Università degli Studi di Padova

Centro Ricerche Fusione (**CRF**)

Università degli studi di Napoli Federico II

Universidade de Lisboa

Instituto Superior Técnico (**IST**)

JOINT RESEARCH DOCTORATE IN FUSION SCIENCE AND ENGINEERING

Cycle XXX

MAGNETIC RECONNECTION IN FUSION PLASMAS

Coordinator: Prof. Paolo Bettini

Supervisors: Dr. Emilio Martines, Dr. Matteo Zuin

Ph.D. student: Luigi Cordaro

Padova

UNIVERSITÀ
DEGLI STUDI
DI PADOVA

JOINT Doctorate and NETWORK in Fusion Science and Engineering

Network Partners:

- Instituto Superior Técnico (IST) Lisboa, Portugal
- Università degli studi di Padova, Italy
- Ludwig Maximilians University Munich, Germany

In collaboration with:

Consorzio RFX
IPP Garching, Germany

Contents

Introduction

Summary

This thesis is devoted to the experimental study of magnetic reconnection and the related phenomena taking place in the plasmas produced in the RFX-mod device, a flexible toroidal facility for the study of magnetic plasma confinement for nuclear fusion.
Magnetic reconnection consists in a rearrangement of the magnetic field topology, which results in a conversion of magnetic energy into heat and kinetic energy of charged particles. It occurs everywhere in the universe, being observed in the evolution of solar flares, in the interaction of solar-wind with the Earth's magnetosphere and in star accretion disks. Magnetic reconnection occurs also in laboratory plasmas, especially in the self-organization processes in current carrying fusion plasmas. In the latter, magnetic reconnection events are particularly evident during sawtooth activities in tokamaks and in the discrete relaxation events (DREs) in Reversed Field Pinchs (RFPs). They are also involved in island formation associated to the stearing instability. During these phenomena, a topology change of the magnetic field lines occurs, leading to new equilibrium configurations of lower magnetic energy.
A complete and detailed understanding of magnetic reconnection is still missing, therefore this phenomenon represents an important topic to be studied for a better understanding of a large variety of astrophysical and laboratory phenomena.
The research activity, here presented, is based on the analysis of the experi-

mental RFX-mod data, coming mainly from the in-vessel system of electrostatic and magnetic probes. The experimental analyzes have been performed alongside theoretical modeling activities.

The overall activity can be divided in two main parts: in the first one, a characterization of reconnection phenomena in fusion plasmas, with special emphasis on the RFP configuration, has been performed; the second one is dedicated to the study of the rotation of magnetic islands in tokamak circular discharges.

The characterization of magnetic reconnection has been carried out by analyzing the DREs in RFP discharges. During these phenomena, a toroidally localized $m = 0$ magnetic perturbation develops, associated with the formation of a poloidal current sheet. The analysis, performed on the high-frequency magnetic perturbation data, has shown that the current sheet is naturally subject to a fragmentation process, determining, in turn, a multi-scale electric field structure, which has been suggested to be able to efficiently accelerate charged particles. Indeed, the acceleration of supra-thermal ions, mainly localized at the position where magnetic reconnection occurs, has been observed during the discrete relaxation events. Such particles have energies high enough to induce enhanced fusion reactivity, as evidenced by the time behavior of the detected neutron fluxes. These evidences show that magnetic reconnection can efficiently contribute to the plasma heating of RFP plasmas.

The second main research activity has been devoted to the analysis of tearing mode dynamics in the RFX-mod plasmas in tokamak configuration. Tearing modes are resistive instabilities, developing both in tokamak and RFP plasmas. In the presence of resistivity, field lines can tear and reconnect, determining a change in the magnetic topology. The resulting magnetic configuration is characterized by the presence of magnetic islands, which, in turn, favor the radial transport of particles and the confinement reduction.

Tearing modes are therefore a concern for magnetic confinement and their characterization is important in order to control them and achieve better confinement performances.

The study of tokamak circular discharges has included both the analysis of

experimental data and a theoretical modeling of mode rotation based on the two-fluid MHD equations.

The comparison of experimental and theoretical results has shown that the rotation of magnetic islands in RFX-mod tokamak plasmas is driven mainly by the diamagnetic drift. The variation of the latter can determine the slowing down of tearing mode rotation, a phenomenon which is sometimes associated with the growth of the instability and the sudden loss of magnetic confinement (disruption). Finally, a characteristic quasi-cyclic oscillation of both amplitude and frequency of tearing mode, known as 'limit cycle', has been observed. This behavior has been found to be coupled to sawtooth activities occurring in the plasma core.

Sommario

Questa tesi è dedicata allo studio sperimentale della riconnessione magnetica e ai fenomeni correlati che si verificano nei plasmi generati da RFX-mod, una macchina sperimentale molto flessibile per lo studio del confinamento magnetico dei plasmi per la fusione termonucleare.
La riconnessione magnetica consiste in un riarrangiamento della topologia del campo magnetico, che determina una conversione di energia magnetica in calore e energia cinetica di particelle cariche. Essa si verifica ovunque nell'universo, essendo osservata nell'evoluzione dei brillamenti solari, nella interazione del vento solare con la magnetosfera della Terra e nei dischi di accrescimento delle stelle. La riconnessione magnetica avviene anche nei plasmi di laboratorio, specialmente nei processi di auto-organizzazione che si verificano nei plasma da fusione. In quest'ultimi, gli eventi di riconnessione magnetica sono particolarmente evidenti durante le attività sawtooth dei tokamak e negli eventi di rilassamento discreti (DRE) nei reversed field pinch (RFP) e sono coinvolti nella formazione di isole magnetiche associate alle instabilità 'tearing'. Durante questi processi si verifica un cambiamento topologico delle linee del campo magnetico, che porta a nuove configurazioni di equilibrio di energia magnetica inferiore.
Una comprensione completa e dettagliata della riconnessione magnetica è ancora mancante. Tale fenomeno rappresenta un importante argomento da studiare per una migliore comprensione di una grande varietà di fenomeni astrofisici e di laboratorio.
Il lavoro di analisi presentato in questa tesi è principalmente basato sull'analisi dei dati sperimentali di RFX-mod, provenienti da sistemi di sonde elettrostatiche e magnetiche, posizionate all'interno della camera da vuoto. Le analisi sperimentali sono state affiancate anche da attività di modellizzazione teorica.
L'attività complessiva può essere divisa in due parti principali: nella prima è stata svolta una caratterizzazione dei fenomeni di riconnessione nei plasmi in configurazione RFP; la seconda è dedicata allo studio della rotazione delle isole magnetiche in scariche tokamak circolari.

La caratterizzazione della riconnessione magnetica è stata effettuata analizzando i DRE in scariche RFP. Durante questi fenomeni, la perturbazione magnetica determina la formazione di modi toroidalmente localizzati $m = 0$, associati alla formazione di strutture di corrente poloidale. L'analisi ha dimostrato che queste strutture sono naturalmente soggette a frammentazione, la quale determina a sua volta una struttura di campo elettrico multi-scala che, come mostrato in letteratura, è in grado di accelerare efficacemente le particelle cariche. In effetti, è stata osservata l'accelerazione di ioni sovratermici, particolarmente evidenti nelle posizioni in cui si verifica la riconnessione magnetica, durante gli eventi discreti di rilassamento. Tali particelle hanno energia abbastanza alta da indurre una reattività da fusione, come dimostrano gli andamenti temporali dei flussi neutronici.
Queste evidenze sperimentali dimostrano che la riconnessione magnetica può contribuire in modo efficace al riscaldamento del plasma nei dispositivi RFP.
La seconda attività di ricerca principale è stata dedicata all'analisi della dinamica dei modi tearing nei plasmi di RFX-mod in configurazione tokamak. Tali modi tearing sono instabilità resistive, che si sviluppano sia nei plasmi tokamak che in quelli RFP. In presenza di resistività, le linee di campo possono rompersi e riconnettere, determinando un cambiamento nella topologia magnetica. La configurazione magnetica risultante è caratterizzata dalla presenza di isole magnetiche che, a loro volta, favoriscono il trasporto radiale di particelle e la riduzione del confinamento magnetico.
I modi tearing costituiscono quindi un problema per il confinamento magnetico e la loro caratterizzazione è importante per poter proporre metodi di controllo al fine di migliorare le prestazioni del confinamento.
Lo studio delle scariche tokamak ha incluso sia l'analisi dei dati sperimentali che una modellazione teorica della rotazione dei modi tearing basata sulle equazioni MHD a due fluidi. Il confronto dei risultati sperimentali con le previsioni del modello teorico ha mostrato che la rotazione delle isole magnetiche nei plasmi tokamak di RFX-mod è guidata principalmente dalla deriva diamagnetica. La variazione di quest'ultima può determinare, associate ad una modifica dei profili di pressione, al rallentamento della rotazione di tali modi, un fenomeno talvolta associato alla crescita delle instabilità e che può portare

alla disruzione.
Infine, è stata osservata una caratteristica oscillazione quasi-ciclica di ampiezza e frequenza dei modi tearing, chiamata 'ciclo limite'. Questo comportamento è dimostrato essere accoppiato alla cosiddetta attività 'sawtooth' che si verifica nella regione centrale del plasma.

Resumo

Esta tese é dedicada ao estudo da reconexão magnética e os fenômenos relacionados que ocorrem em plasmas produzidos pelo RFX-mod, um dispositivo toroidal flexível para o estudo do confinamento de plasma para fusão nuclear. A reconexão magnética consiste em um rearranjo da topologia do campo magnético, que resulta em uma conversão de energia magnética em calor e energia cinética de partículas carregadas. Tal fenômeno ocorre em todo o universo, sendo observado na evolução das chamas solares, na interação do vento solar com a magnetosfera da Terra e nos discos de acréscimo das estrelas. A reconexão magnética também ocorre em plasmas de laboratório, especialmente em processos de auto-organização que ocorrem em plasmas de fusão. Nesses últimos, os eventos de reconexão magnética são particularmente evidentes durante as atividades de dente de serra em tokamaks e nos eventos de relaxamento discreto (discrete relaxation events - DREs) em "reversed field pinch" (RFPs) e está relacionado a formação de ilhas associada à instabilidades do tipo "tearing". Durante esses processos, verifica-se uma mudança topológica das linhas de campo magnético, levando a novas configurações de equilíbrio de energia magnética.

Uma compreensão completa e detalhada da reconexão magnética ainda é necessária, portanto este é um tópico importante para uma melhor compreensão de uma grande variedade de fenômenos astrofísicos e laboratoriais. O trabalho de análise apresentado nesta tese baseia-se principalmente na análise de dados experimentais, provenientes de sondas eletrostáticas e magnéticas, posicionadas dentro da câmara de vácuo do RFX-mod. As análises experimentais também foram apoiadas por atividades de modelagem teórica. A atividade geral pode ser dividida em duas partes principais: na primeira, foi realizada uma caracterização dos fenômenos de reconexão nos plasmas na configuração RFP; a segunda é dedicada ao estudo da rotação das ilhas magnéticas nas descargas tokamak seção circular.

A caracterização da reconexão magnética foi realizada através da análise de DREs em descargas RFP. Durante esses fenômenos, a perturbação magnética determina a formação de modos localizados toroidalmente $m = 0$, associa-

dos à formação de estruturas de corrente poloidais. A análise mostrou que essas estruturas estão naturalmente sujeitas a fragmentação, o que, por sua vez, determina uma estrutura de campo elétrico multi-escala que tem sido sugerido na literatura como sendo capaz de acelerar efetivamente partículas carregadas. De fato, a aceleração dos íons supra térmicos tem sido observada, particularmente evidente nas posições onde ocorre reconexão magnética, durante os eventos discretos de relaxamento. Tais partículas têm energia alta o suficiente para induzir reações de fusão, como evidenciado pela detecção de nêutrons. Essas evidências mostram que a reconexão magnética pode contribuir eficientemente para o aquecimento do plasma em RFP.

A segunda atividade de pesquisa principal foi dedicada à análise da dinâmica dos modos tearing nos plasmas do RFX-mod na configuração tokamak. Tais modos são instabilidades resistivas que se desenvolvem tanto em plasmas em tokamak quanto em RFP. Na presença de resistividade, as linhas de campo podem quebrar e reconectar, resultando em uma mudança na topologia magnética. A configuração magnética resultante é caracterizada pela presença de ilhas magnéticas que, por sua vez, favorecem o transporte radial de partículas e a redução do confinamento magnético.

Os modos tearing são, portanto, uma preocupação para o confinamento magnético e sua caracterização é importante para controlá-los e assim alcançar melhores desempenhos de confinamento.

O estudo das descargas de tokamak incluiu tanto a análise dos dados experimentais como a modelagem teórica da rotação dos modos tearing com base nas equações MHD de dois fluidos. A comparação dos resultados experimentais com as previsões do modelo teórico mostrou que a rotação das ilhas magnéticas nos plasmas do RFX-mod tokamak é impulsionada principalmente pela deriva diamagnética eletrônica. A variação deste último pode determinar, associada a uma modificação dos perfis de pressão, a desaceleração da rotação desses modos, um fenômeno às vezes associado ao crescimento da instabilidade e à perda súbita de confinamento magnético (disruption).

Finalmente, observou-se uma oscilação quase cíclica característica na amplitude e na frequência dos modos tearing. Este comportamento foi demostrado

como sendo acoplado à atividade "dente de serra" que ocorre na região central do plasma.

Content of the thesis

This thesis is organized as follow:

- The first chapter is an introduction to the controlled thermonuclear fusion. The fundamental plasma physics is described and the main types of plasma magnetic confinement are introduced. The plasma equilibrium and the main MHD instabilities are characterized. The tokamak and the Reversed Field Pinch concepts are introduced, by listing the respective advantages and the main operational limits. Finally, a brief overview of the RFX-mod device and of its scientific objectives are given.

- The second chapter deals with the description of diagnostics and experimental methods of investigation. The system of in-vessel probes for magnetic and electrostatic fluctuations and the diagnostics for the kinetic characterization of the RFX-mod plasma behavior are presented. The main analysis techniques are shown, highlighting the advantages and the differences. Among them, the wavelet based method for the identification of intermittent structures in fluctuating signals is described.

- The third chapter is devoted to a description of the phenomenon of magnetic reconnection, in which the conversion of magnetic energy into kinetic and thermal energy of charged particles takes place. First, the magnetohydrodynamic (MHD) theory is introduced, by distinguishing the two-fluid model, the single-fluid resistive model and the ideal one for perfectly conductive plasmas. Then, the most important physical systems that are dominated by the reconnection process are described, referring to recent solar, magnetosphere and laboratory studies. The Sweet-Parker model of magnetic reconnection is illustrated. The theoretical predictions provided by this theory and the comparison with experimental data in literature, are discussed. Finally, some of the most recent theories for magnetic reconnection are presented, illustrating the

differences between collisional and collisionless reconnection phenomena. In the latter framework, the concept of plasmoid instability and its role in determining reconnection dynamics are introduced along with the useful phase diagram.

- The fourth chapter describes the results of experimental analysis of the RFP discharges in RFX-mod, characterized by magnetic reconnection processes occurring during discrete relaxation events. Particular attention is devoted to the study of the evolution of the current layers associated with magnetic reconnection processes, comparing the results with the theoretical predictions. Finally, the effects of these phenomena on the ion distribution function in the velocity space are discussed.

- Finally, the fifth chapter is devoted to the analysis of tearing mode dynamics in tokamak discharges produced by RFX-mod. In particular, the fast rotation of magnetic islands is studied. It is shown, by comparison to the prediction of a dedicated two-fluid MHD model, also presented, that the main driving mechanism of the tearing mode rotation is given by the diamagnetic drift. Evidences that the tearing mode slowing down, a phenomenon that can lead to plasma disruption, is related to a variation of the diamagnetic profiles are given. Furthermore, it is shown that a purely electromagnetic model is not sufficient to explain such a tearing mode dynamics.
  Finally, the characteristic oscillations of amplitude and frequency of the tearing mode under study are shown, highlighting their relationship with the sawtooth activity occurring in the core.

Chapter 1

Nuclear Fusion

1.1 The need of clean energy

The human society needs energy to carry on any kind of activity. The ever increasing quality of life demands ever increasing energy requirements. The energy sources constitute therefore the most important resources for life on Earth. The increasing energy demand has begun to negatively affect the Earth's health and the main evidences of these change are already visible, first among all the global warming. Nowadays, almost the whole energy production is provided by the fossil fuels (petroleum, carbon and natural gas), whose combustion pours greenhouse gases into the atmosphere. These gases, mainly carbon dioxide CO_2 and methane CH_4, regulate the heat radiation rate from the Earth surface back to the space. Greenhouse gases, water included, are transparent to the solar radiation, but opaque to the infrared radiation coming back to the space [1]. In general, most of these gases are essential because they provide the ideal temperature conditions for the life on the Earth. However, their excess, due mainly to the burning of fossil fuels, is generating an excessive temperature increase. It is therefore evident that new energetic strategies, compatible with the increased demand for energy required by social development, are needed in order to protect our planet. These strategies require better awareness of the use of land resources and the use of clean energy sources, alternative to fossil fuels. As shown in Figure

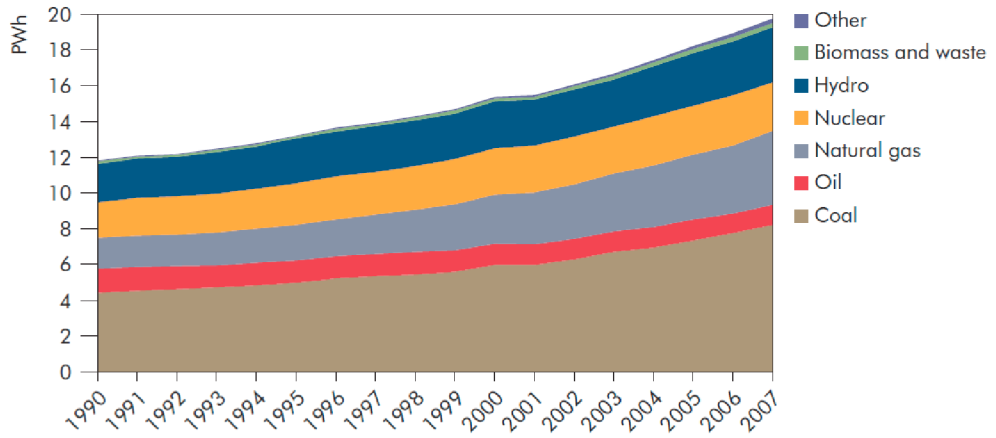

Figure 1.1: Global electricity production from 1990 to 2007. The colored bands represent the different energy source contributions to the total. Taken by [2].

1.1, alternative energies still account for a small part of total energy with respect to the fossil fuels, so major investments in renewable energy research are needed to increase the "green" energy production and reduce as soon as possible the emission of greenhouse gases in the atmosphere.

It must be yet noted that, despite several international policy agreements, the efforts made until now are still inadequate, both because of the high costs of alternative energy compared to fossil fuels and because of public skepticism about the anthropogenic nature of climate change [3, 4], although the human origin of heating has been widely documented by the scientific community [1, 2, 5].

Technological research, in the field of renewable energies, is developing on several fronts such as solar, wind, geothermic, marine just to mention the main ones. However, these sources are still far from being able to meet the demands of world energy. Moreover, renewable energy sources are not constant over time, so their use would require the use of powerful electric energy storage.

The nuclear fission represents an alternative technology, relatively inexpensive, able to deliver a large amount of energy without CO_2 emissions. A nuclear reaction generates an amount of energy about one million times more than an ordinary chemical combustion reaction. With the same energy pro-

duced, the amount of fissile fuel needed is definitely lower than fossil fuels required for classical combustion. However, nuclear fission presents remarkable troubles. First, the fission of heavy elements, such as the ^{235}U uranium isotope, generate further radioactive nuclei, the so-called *radioactive waste*, whose half-life time can be decisively long (up to $\sim 10^6 y$). The radioactive waste causes a serious storage problem, because these exhausted fuels have to be stored in safe places until their radioactivity time reaches the environmental level. Furthermore, public opinion, as a result of nuclear accidents, such as those of Fukushima and Chernobyl, considers the nuclear fission plants extremely dangerous.
A possible solution, especially in the transition phase from fossil fuels to renewable sources, could be provided by nuclear fusion, an extremely efficient, unlimited, safe, clean energy source.

1.2 The nuclear fusion

The nuclear fusion is the physical reaction by which the interaction of two or more light atomic nuclei generates a heavier nucleus and, eventually, other reaction products, like neutrons. In this process energy is released in the form of radiation and kinetic energy of particles. The power of the Sun and other stars comes from nuclear fusion.
Two nuclei fuse together if they approach close enough ($\lesssim 10^{-15} m$) for the strong short-range nuclear forces to exceed repulsive Coulomb forces between particles with the same electrical charge. This is possible only if the colliding particles have high enough kinetic energy.
The mass of a stable nucleus is less than the sum of the *nucleons* masses, that is of protons and neutrons that make up the nucleus. The mass difference Δm, known as *mass defect*, is converted into energy ΔE according to the famous Einstein's relation:

$$\Delta E = \Delta m c^2 \tag{1.1}$$

where c is the speed of light. This means that a very small amount of mass corresponds to a huge amount of energy.
The energy released in a nuclear reaction is equal to the energy needed to break the bonds that keep the nucleons together in the nucleus. This energy, called *binding energy*, is related to the mass defect by equation 1.1.
Fig. 1.2 shows the binding energy per nucleon as a function of the number of nucleons A in the nucleus. The energy is small for the lightest elements, it grows up to a maximum value for iron ^{56}Fe and then slows down slowly for the heaviest elements. Nuclear energy is released when reactions lead to an increase in the binding energy [6], therefore, apart of some exceptions, the fusion of light nuclei (up to ^{56}Fe) releases energy because the mass defect of the products is higher than that of reagents. For heavy nuclei, there is energy release only for the opposite process, that is the nuclear fission.

The most promising reactions, for the thermonuclear fusion, involve the

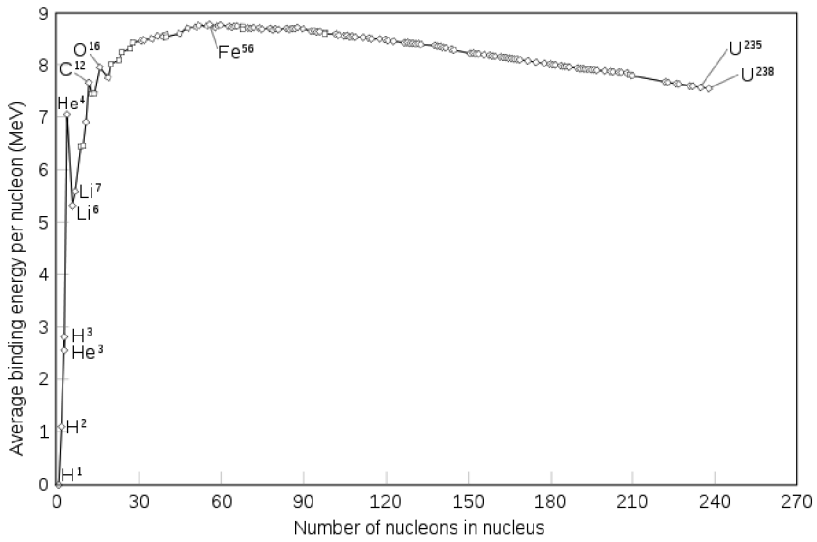

Figure 1.2: Binding energy as a function of the number of nucleons in nucleus

hydrogen H and its isotopes, deuterium D and tritium T [7]:

$$
\begin{aligned}
{}^{2}_{1}D + {}^{2}_{1}D &\xrightarrow{50\%} {}^{3}_{1}T + {}^{1}_{1}H + 4.03MeV && (1.2)\\
{}^{2}_{1}D + {}^{2}_{1}D &\xrightarrow{50\%} {}^{3}_{2}He + {}^{1}_{0}n + 3.27MeV && (1.3)\\
{}^{2}_{1}D + {}^{3}_{1}T &\longrightarrow {}^{4}_{2}He + {}^{1}_{0}n + 17.6MeV && (1.4)\\
{}^{2}_{1}D + {}^{3}_{2}He &\longrightarrow {}^{4}_{2}He + {}^{1}_{1}H + 18.3MeV && (1.5)
\end{aligned}
$$

Of these reactions, the first two have approximately equal probability to take place.

It must be noted that, in fusion physics, the temperature is usually expressed in terms of the thermal energy k_BT, $1eV$ corresponding to $11600k$.

The main aim of a future fusion plant essentially is to produce controlled fusion reactions in a reactor chamber and convert the kinetic energy of the product particles into electric energy.

Fig. 1.3 shows the cross-sections of the above equations as a function of the deuteron[1] energy, obtained by bombarding deuterium, tritium and helium targets with deuteron beams of known energy. The D-T reaction has the higher cross-section at low energies, therefore it is the most favorable reaction, at the moment, for thermonuclear reactors. At this temperature, the energy that particles must have is so high that the fuel material is a full ionized gas, that is a plasma. In particular, the required temperature to reach a convenient D-T reaction condition is of order of 10 keV.

Deuterium accounts for approximately 0.015 % of natural hydrogen and exists in 158 ppm (part per million) in seawater [8]. Its extraction requires a simple chemical process, therefore hydrogen is a virtually inexhaustible source. Tritium instead is a radioactive isotope, with an half-life time of 12.26 years and does not exist in nature, it must be produced in a secondary nuclear reaction [8]. Tritium can be obtained by the following fusion reactions, which use

[1] A deuteron is a nucleus of deuterium.

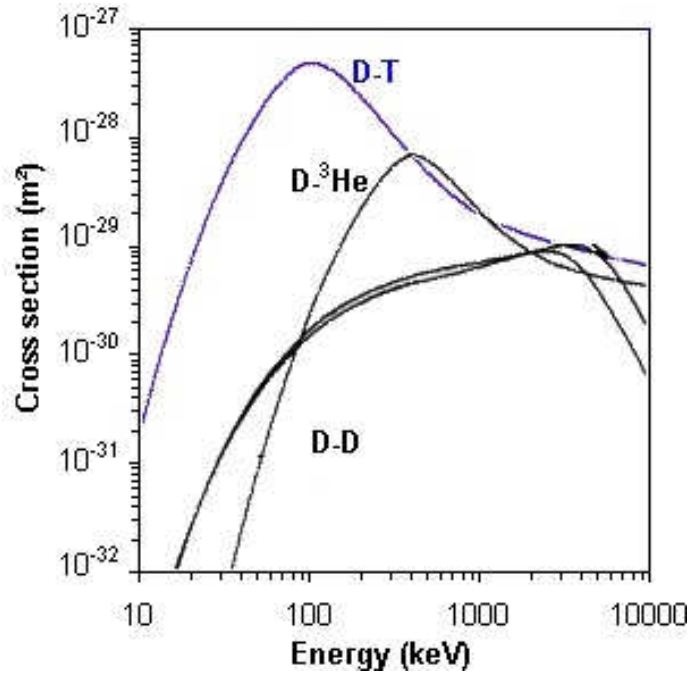

Figure 1.3: Cross-section of fusion reactions as a function of deuteron energy

lithium Li as moderator [6]:

$$ {}^{6}_{3}Li + {}^{1}_{0}n \ (slow) \longrightarrow {}^{3}_{1}T + {}^{4}_{2}He + 4.8MeV \tag{1.6} $$

$$ {}^{7}_{3}Li + {}^{1}_{0}n \ (fast) \longrightarrow {}^{3}_{1}T + {}^{4}_{2}He - 2.5MeV \tag{1.7} $$

A Lithium *blanket*, installed on the same fusion reactor, has been tough as solution for the Tritium supplying, neutrons being provided by the D-T reactions inside the machine itself. According to the present resources estimation, lithium could be a tritium source for an unlimited time, therefore the fusion machines would have an unlimited amount of fuel.
The reactions in a fusion machine would generate, as a product, only Helium that is not a greenhouse gas, hence fusion is a completely "green" energy source.
One method for obtaining the fusion reactions could be shooting an ion beam against an ion target of the other species. However, it must be considered that the elastic collision cross section is generally much greater than that of the D-T reaction; moreover, the particles undergoing elastic collisions are

lost from the beam. Therefore the used approach is to generate a plasma, confining it for longer than the typical collision times, so that the ions may have time to undergo fusion reactions without being lost from the plasma due to the collisions. Plasma ions in thermal equilibrium will have a certain energy distribution, and therefore a percentage of them may have a much higher energy content than average, which means that average energy levels lower than those of ion beams are sufficient.

1.3 Energetic balance

The aim of thermonuclear fusion is to heat a plasma to high temperatures while maintaining a high density for a time long enough that the energy released by the nuclear reactions exceeds that required to sustain the plasma itself.
In a D-T reaction, the energy released E_{fus} is distributed in 3.5 MeV to α-particles (the He nuclei) and 14.1 MeV to neutrons. The α-particles can eventually contribute to maintain the plasma heating, while the neutrons can be stopped at the external walls and the resulting heat serves to generates vapor sustaining the motion of the turbines for the electricity production.
Here a rough power balance in a fusion reactor is presented.
Given a plasma of electron and ions, the average energy per particle is $\frac{3}{2}T$. Therefore the energy per unit volume w is:

$$w = 3\langle nT \rangle \tag{1.8}$$

The power per unit volume, generated by fusion reactions, can be written as

$$p_f = n_D n_T \langle \sigma v \rangle E_f \tag{1.9}$$

where n_D and n_T are the mean densities of deuterium and tritium, respectively; $\langle \sigma v \rangle$ is the D-T reaction rate and $E_f = 17.6$ MeV is the energy released by a single fusion reaction.
The total density is $n = n_D + n_T$, therefore, taking into account an equal

amount of deuterium and tritium, the fusion power density can be written as:

$$p_f = \frac{1}{4} n^2 \langle \sigma v \rangle E_f \tag{1.10}$$

About one fifth of the energy released by a D-T reaction is sold to the α-particles, which, being electrically charged, remain confined by the magnetic field and contribute to the plasma heating by particle collisions. The power density related to the α-particles thus is:

$$p_\alpha = \frac{1}{4} n^2 \langle \sigma v \rangle E_\alpha \tag{1.11}$$

The temporal evolution of the thermal energy can be thus written as

$$\frac{dw}{dt} = p_{ext} + p_\alpha - p_L - p_R \tag{1.12}$$

where p_{ext} is the eventual externally supplied power density, p_R represents the power loss by radiation, p_L the power loss by transport (i.e. by convection and conduction).
By considering a full ionized plasma, the main contribution to the radiative losses is given by the bremsstrahlung radiation[2], which power density p_b can be written as [7]

$$p_b = 5.35 \cdot 10^{-37} \alpha_b n^2 T_e^{\frac{1}{2}} \ W m^{-3} \tag{1.13}$$

where T_e is expressed in kev.
The transport contribution to the losses is difficult to estimate. It is usually quantified by means of the so-called *confinement time* τ_E, representing the average time a particle remains confined in the plasma:

$$\tau_E = \frac{w}{p_L} \tag{1.14}$$

In absence of fusion reactions, an external heating $p_{ext} = p_L + p_R$ must be supplied in order to maintain the plasma in stationary conditions. The time

[2]Bremsstrahlung is the electromagnetic radiation, characterized by a continuous spectrum, produced by charged particles decelerated by collision processes.

confinement can thus be approximated by the relation:

$$\tau_E = \frac{w}{p_{ext} - p_R} \tag{1.15}$$

This suggests that the bremsstrahlung radiation fixes a low temperature limit for the energy balance. This limit is usually identified by the condition $p_\alpha = p_b$, that means that the α-particles match the radiation losses. This limit corresponds to a temperature of 4.4 keV for D-T reactions [9].
The most favorable condition would be that for which the power provided by α-particles is sufficient to balance all the losses, without any external heating:

$$p_\alpha = p_L - p_b \tag{1.16}$$

This condition is known as *ignition*. In this case, the external power would only be used in the initial transient phase, in order to trigger the fusion reactions, which would then be able to sustain the process. The ignition condition occurs if the following condition takes place [7]:

$$n\tau_E > \frac{12T}{\langle\sigma v\rangle E_\alpha - 4\alpha_b T^{1/2}} \tag{1.17}$$

The minimum product $n\tau_E$ required for ignition is drawn as a function of the temperature in Fig. 1.4. The minimum at $T \simeq 30keV$ represents the temperature at which it is easier to obtain the ignition. At this temperature, the ignition condition can be written as:

$$n\tau_E > 1.5 \cdot 10^{20}\ m^{-3}s \tag{1.18}$$

Nevertheless, the operative temperature in a fusion reactor is though to be between 10 and 20 keV, in order to optimize power density while minimizing the bremsstrahlung radiation losses. By taking in mind that the reaction rate $\langle\sigma v\rangle$ depends on the temperature, the ignition condition can be written in terms of the product of density, confinement time and temperature (simply

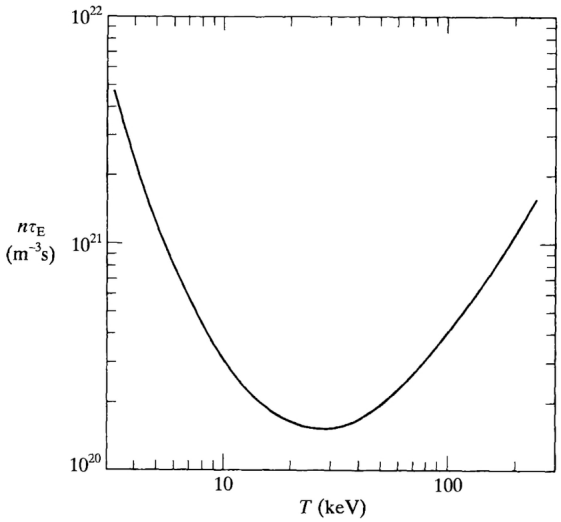

Figure 1.4: Plot of the necessary condition for ignition as stated by equation (1.17). Taken by [7].

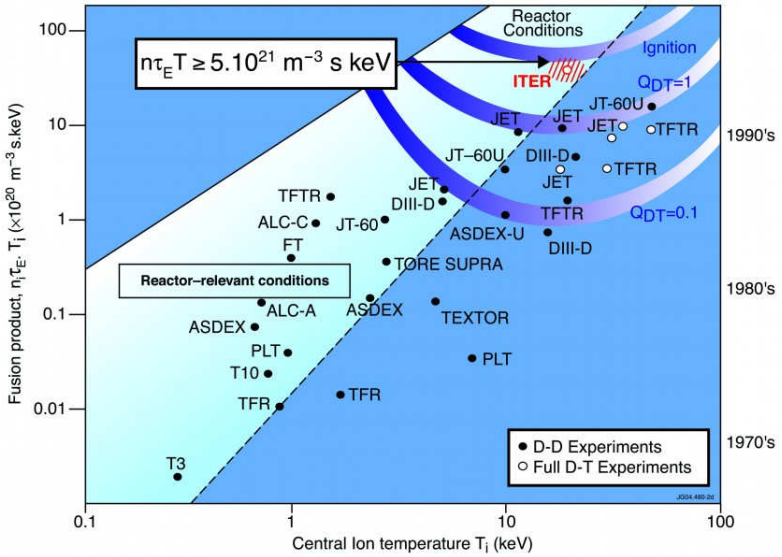

Figure 1.5: Fusion triple product achieved on different fusion facilities. Credit EUROfusion.

known as the *triple product*):

$$n\tau_E T > 5 \cdot 10^{21}\ m^{-3} keV s \tag{1.19}$$

This condition can be achieved, for example, with $n = 10^{20} m^{-3}$, $T = 14keV$ and $\tau_E = 3.5s$.
Fig. 1.5 shows the values of the triple product achieved in fusion devices up to now and that expected for the forthcoming fusion experiment ITER (*International Thermonuclear Experimental Reactor*), the biggest reactor for the thermonuclear experiments under construction in Cadarache, France.
The performances of a fusion reactor can be estimated by means of a figure of merit Q, measuring the ratio of the produced fusion power P_{fus} to the external power P_{fus} needed to compensate the energy losses:

$$Q = \frac{P_{fus}}{P_{ext}} \sim \frac{(nT)^2}{P_{loss} - P_\alpha} \tag{1.20}$$

where the scaling of P_{fus} with n and T is an approximation.
The condition $Q = 1$, said *breakeven*, is that in which fusion reactions generate an amount of energy equal to that provided by the external systems. For a net power gain, the total output thermal power must exceed the external heating power required to maintain the plasma [9]. At ignition, the external heating is reduced to zero and $Q \to \infty$. In order to have a positive energy balance, sufficient for a net production of energy, a value $Q > 10$ is required. Actually, the main aim of ITER is to show the feasibility of nuclear fusion by achieving a figure of merit $Q > 10$ for a sufficient long time.

1.4 Plasma confinement

The study of the plasma confinement for achieving the nuclear fusion conditions is performed in laboratory on two main fronts: inertial and magnetic confinement.

Inertial confinement

A D-T pellet is uniformly heated by several powerful laser beams, which cause the ablation of the external layer. This has, as a consequence, the implosion of the internal part of the target, creating the conditions for fusion reactions [10]. The process persists till the material expands and dilutes. This kind of process is nothing else than a mini thermonuclear explosion. The confinement time is very short ($\sim 10^{-10}s$), hence, in order to obtain the conditions for nuclear reactions, the fuel material must be compressed to very high density values ($\sim 10^{31}m^{-3}$), that is about 10^3 times the density of the deuterium and tritium at liquid state.

Magnetic confinement

Fuel particles, in the state of plasma, are confined by intense magnetic fields. It is in fact known that a charged particle in a magnetic field moves in a spiral motion along a magnetic field line, whose Larmor radius is $r_L = \frac{m_p v_\perp}{q_p B}$, where $v_\perp$ is the velocity component perpendicular to the field line. If the magnetic field is strong enough, in absence of collisions, the particle is thus confined in a direction perpendicular to the magnetic field. This confinement method, on which this thesis is focused, is described on a more detail in the next section.

1.5 Magnetic confinement

The magnetic field can confine the charged particles in a orthogonal direction, by means of the Lorentz force, but not in the longitudinal direction. Several magnetic field geometries have been adopted from the beginning of the fusion studies [11], concluding that the best solution in order to reduce the longitudinal losses is that in which magnetic field lines are closed, forming a toroidal configuration.
Fig. 1.6 shows the coordinate system, used in the rest of this thesis, describing this toroidal geometry. The torus is described by the following quantities: the *major radius* R_0, that is the distance from the rotation axis (*major axis*)

to the plasma center (*minor axis*), and the *minor radius* a, that is the distance from the minor axis to the external edge. The ratio R_0/a is called *aspect ratio*.

The coordinate system is given by the radial coordinate r, the toroidal an-

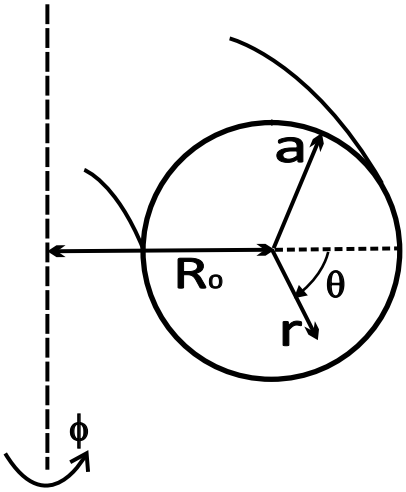

Figure 1.6: Schematic of the toroidal coordinate system.

gle ϕ, measuring rotations around the major axis; and the poloidal angle θ, measuring rotations around the minor axis (Figure 1.6).

Sometimes, in order to simplify the plasma modeling, a cylindrical coordinate system (r, θ, z) is used, in which the torus is stretched into a cylinder. In this reference system, z is the direction along the cylinder, instead of the toroidal coordinate ϕ. This approximation can be consider valid for large aspect ratios.

The closed magnetic configuration, with a purely toroidal magnetic field B_ϕ, avoids particle losses along the field lines. However, it leads, for the Ampere's law, to a non-uniformity of the magnetic field magnitude, which have higher values at the inner side (called *high field side* HFS) while it decreases towards the outer side (*low field side* LFS).

In such a configuration, the particle drifts become important. In particular, the line curvature determines a *curvature drift*

$$\mathbf{v_c} = -\frac{m_p v_\parallel^2}{q_p}\frac{\nabla \mathbf{B} \times \mathbf{B}}{B^3} \tag{1.21}$$

while the non-uniformity generates a *grad-B drift*

$$\mathbf{v}_{\nabla \mathbf{B}} = -\frac{m_p v_\perp^2}{2q_p} \frac{\nabla \mathbf{B} \times \mathbf{B}}{B^3} \tag{1.22}$$

where B indicates the magnetic field, v the particle velocity, m_p the particle mass, q_p the particle charge.
Both drifts generate a radial charge-independent drift

$$\mathbf{v}_{\mathbf{E} \times \mathbf{B}} = -\frac{\mathbf{E} \times \mathbf{B}}{B^2} \tag{1.23}$$

which carries particles outwards, determining particle losses and confinement destruction.
The problem is fixed by adding a poloidal field component to the total magnetic field, resulting on the $E \times B$ drift cancellation in a toroidal turn. The resulting magnetic field lines describe helical paths around nested toroidal surfaces, known as *magnetic surfaces*. The helical winding is described by an important topological quantity, called *safety factor* q, which represent the number of toroidal turns traveled during one poloidal turn:

$$q = \frac{\Delta \phi}{2\pi} \tag{1.24}$$

The variation of the helical winding along the radial direction, that is moving along neighboring magnetic surfaces, is expressed by the *magnetic shear*:

$$s = \frac{r}{q} \frac{dq}{dr} \tag{1.25}$$

Three main toroidal configurations make use of helical magnetic fields to confine plasma: tokamak, reversed field pinch and stellarator.
The difference among these devices consists in the way the magnetic field components are produced. In the first two, the magnetic field components are generated by both the plasma current and the outer coils, while in the latter, which does not carry any plasma current, the helical twist of the magnetic field lines is entirely generated by currents flowing into external

coils.
In this chapter, only the two current-carrying configurations are described, both being topics of this thesis.

1.6 Plasma equilibrium and instabilities

The modeling of a plasma can be done by using different approaches, which depend on the level of accuracy required in the description. The more detailed model should take into account the motions of each individual particle and the interaction with each other. It is clear that this approach is not feasible and some simplifications must be done in order to make the equations more manageable.
The simplest approach consists into consider the plasma as an electrically conducting fluid, under the effect of pressure and electromagnetic fields. This theory, described in a more detail in chapter 3, is called *Magnetohydrodynamics* (MHD).

1.6.1 Plasma equilibrium

The steady-state status of plasma is described by assuming stationary ($\partial/\partial t = 0$) and static ($\mathbf{v} = 0$) conditions. The MHD equations give the *force-balance equation*:

$$\mathbf{j} \times \mathbf{B} = \nabla p \tag{1.26}$$

which describes the balance between magnetic and pressure gradient forces. This equation means that the current flowing perpendicular to the magnetic field exercises a force on the fluid element that is balanced by the plasma kinetic pressure. Taking the dot-product of equation (1.26) with $\mathbf{B}$, the following equation is obtained:

$$\mathbf{B} \cdot \nabla p = 0 \tag{1.27}$$

This means that the pressure gradient is null along the magnetic field or, in other terms, the magnetic field lines must lie in constant pressure surfaces.

Analogously, the following formula is obtained by taking the dot-product of equation (1.26) with $\mathbf{j}$:

$$\mathbf{j} \cdot \nabla p = 0 \tag{1.28}$$

This means, in the same way, that the current lines lie on constant pressure surfaces.

Therefore, equation (1.26) describes nested magnetic, current and pressure isosurfaces that characterize the toroidal thermonuclear plasmas. Furthermore, each surface can be described by a value of the safety factor q (1.24), which can be written, in cylindrical approximation, as [12]:

$$q \simeq \frac{r}{R_0} \frac{B_\phi(r)}{B_\theta(r)} \tag{1.29}$$

The force-free balance equation (1.26) can be written in an alternative way, by using the vector identity and the Ampere's law $\nabla \times \mathbf{B} = \mu_0 \mathbf{j}$, in order to obtain the *pressure balance equation*:

$$\nabla(\frac{B^2}{2\mu_0} + p) = \frac{1}{\mu_0}(\mathbf{B} \cdot \nabla)\mathbf{B} \tag{1.30}$$

where μ_0 is the magnetic permeability. The gradient of the sum of magnetic pressure $B^2/2\mu_0$ and kinetic pressure p balances a force due to the bending and parallel tension of the magnetic field.

An important parameter used in fusion physics is the β parameter, defined as the ratio of the kinetic pressure p, averaged over the plasma volume, and the magnetic pressure:

$$\beta = \frac{\langle p \rangle}{\frac{B^2}{2\mu_0}} \tag{1.31}$$

The β parameter can be though as a measurement of the ability of the magnetic field pressure to confine the plasma.

1.6.2 MHD instabilities

The MHD theory predicts that, under certain conditions, small perturbations of the fluid quantities, such as the density or the magnetic field, can grow

up in time, giving rise to the so-called *MHD instabilities*. A perturbation is unstable if it reduces the potential energy of the system.
The main basic classifications of MHD instabilities are here exposed.
MHD instabilities are basically classified according to the source of free-energy which drives the perturbation to grow, hence there are mainly *current-driven* instabilities, driven by the non-uniform current density parallel to the magnetic field; *pressure-driven* instabilities, driven by the pressure gradients and the magnetic field curvature; and *particle-driven* instabilities, associated to plasma particles.
The MHD instabilities can be basically characterized by [13]:

- mode numbers (m,n);
- growth rate of the mode (γ);
- frequency in the laboratory frame ($f = 2\pi\omega$);
- radial displacement of the mode $\tilde{A}_k(r)$

A perturbation $\tilde{A}$ of a physical quantity A can be decomposed as a sum of Fourier components as follow:

$$\tilde{A}(r,\theta,\phi,t) = \sum_k \tilde{A}_k(r)\, e^{i(\mathbf{k}\cdot\mathbf{r}-w\,t)}\, e^{\gamma t} = \sum_k \tilde{A}_k(r)\, e^{i(m\,\theta - n\,\phi - \omega\,t)}\, e^{\gamma t} \qquad (1.32)$$

where $\mathbf{k} = (k_r, k_\theta, k_\phi) = (k_r, m/r, n/R_0)$ is the wave-vector in toroidal coordinates, m and n being called *poloidal wave-number* and *toroidal wave-number*, respectively. A helicoidal perturbation is called *mode* and it can be represented by the pair of numbers (m,n). In this decomposition, the exponential growth of the mode amplitude ($\tilde{A}(t) \propto e^{\gamma t}$), characterized by the growth rate γ, is assumed .
It can be shown that modes can grow unstable if the wave vector $\mathbf{k}$ satisfies the *resonance condition*

$$\mathbf{k} \cdot \mathbf{B_0} = 0 \qquad (1.33)$$

where $\mathbf{B_0}$ is the equilibrium magnetic field.
A system on equilibrium is in a state of minimal energy, therefore, if a perturbation deformed the field, that is if $\mathbf{k} \cdot \mathbf{B_0} \neq 0$, then there would be an increase in energy. This is an energetically unfavorable condition, and the

system would return to its state of equilibrium. Therefore, only perturbation that satisfy equation (1.33) can grow up unstable in time.
The resonance condition (1.33) can be also written as a function of the mode numbers as follow:

$$\mathbf{k} \cdot \mathbf{B} = \frac{m}{r} B_\theta - \frac{n}{R_0} B_\phi = 0 \tag{1.34}$$

The safety factor q can then be expressed as:

$$q = \frac{r}{R_0} \frac{B_\phi(r)}{B_\theta(r)} = \frac{m}{n} \tag{1.35}$$

This means that the helical MHD modes can grow at the magnetic surfaces, known as *rational* or *resonant surfaces*, where the safety factor assumes rational values.
A mode with numbers (m,n) has the same helicity as the resonant surface where it develops, in which the magnetic field lines close after m toroidal and n poloidal turns. In the non-resonant surfaces, instead, the magnetic field lines never closes, covering uniformly the magnetic surface [13]. The tension of the magnetic field lines, so densely covering the non-resonant surfaces, prevent the perturbation growth.
MHD instabilities can be also classified as *ideal* and *resistive*. In the ideal case, which can be described in the context of the ideal MHD (section 3.2), the plasma has no resistivity and the instabilities change only the shape of the magnetic surfaces, any topological change being forbidden. The instabilities grow in a short time, of the order of the Alfvén time[3], so they cannot be stabilized by using external feedback actuators. These instabilities are usually known as ideal *kink* instabilities because they generate displacements that tilt and kink the plasma [13]. The presence of conductive structures close to the plasma may slow down the kink growth time to the inverse of the resistive time scale of the wall, the ideal kink resulting thus converted in the so-called *Resistive Wall Mode* (RWM) [14].

[3]The Alfvén time $\tau_A = \frac{L}{v_A} = \sqrt{\frac{\mu_0 m_i n L^2}{B^2}}$, where n is the plasma density, L is the typical length of the instability and v_A is the Alfvén velocity, represents the time spent by an electromagnetic wave to cross the length L in the plasma.

The resistive instabilities can instead develop when some resistivity appears in the plasma, leading magnetic reconnection to take place, changing the topology of the magnetic field and accessing to lower energy states. A resistive instability is characterized by a growth time greater than the ideal one and less than the resistive diffusion time.
Tearing modes are the most important example of resistive instabilities, developing both in tokamak and RFP plasmas. They are current-driven instabilities, but can be converted in pressure-driven instabilities, called *Neoclassical Tearing Modes* (NTMs), in high beta plasmas. The name tearing mode

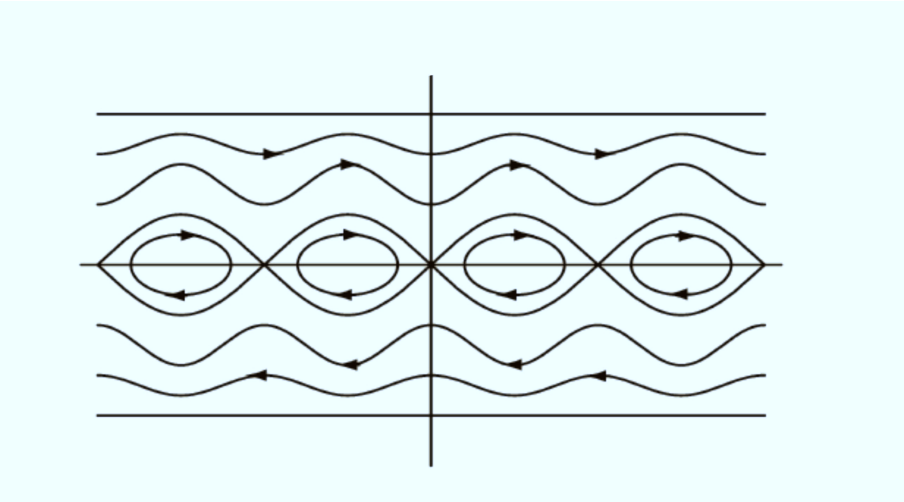

Figure 1.7: Schematic of magnetic islands generated by tearing mode instability. Taken by [15]

originates from the fact that, in the presence of resistivity, the field lines can tear and reconnect, determining a change in the magnetic topology. The resulting magnetic configuration is characterized by the presence of magnetic islands, as schematized in Figure 1.7.
Tearing modes are a trouble for magnetic confinement because magnetic islands favor the energy and particle radial transport. Moreover, the eventual overlap of magnetic islands generates stochasticization of the magnetic field lines, which are no longer obliged to stay on one magnetic surface, consequently reducing plasma confinement.
Finally, in order to complete a general characterization of the modes, it is nec-

essary to specify where instability occurs. Hence, they are distinguished from *internal modes*, which develop mainly internally to the plasma ($\tilde{A}_k(a) = 0$) and *external modes*, which affect the plasma edge ($\tilde{A}_k(a) \neq 0$). However, it is important to remember that this classification is basic. A large number of modes, with different names, exist. Other effects, such as geometric effects or the interaction among multiple modes, can generate further instabilities whose evolution can generate complex physical phenomena that need to be carefully studied [13].

1.7 Tokamak

The word "Tokamak" is a Russian acronym for *toroidal chamber with magnetic coils*. The tokamak configuration has been the most studied worldwide and the most performing, since present-day devices have achieved the temperature conditions for D-T fusion reactions [13].
The tokamak concept is characterized by high toroidal magnetic field B_ϕ, produced by a set of field coils encircling the plasma, called *toroidal field coils* and by a lower poloidal magnetic field B_θ, produced by a toroidal plasma current. The latter is, in turn, induced by the transformer action of a set of primary *poloidal field coils*, the plasma itself representing the secondary [12]. The flux variation is obtained simply by changing the voltage applied at the primary winding coils. Additional outer poloidal coils are used to control the position and the shape of plasma. In the most performing tokamak devices, superconductive coils are used in order to produce very strong magnetic fields. Figure 1.8 shows a schematic of a tokamak machine, showing the main coil distribution.
Due to the temporal limitation of the magnetic flux variation in the central coils, the plasma current cannot be sustained for long-pulse operations without additional non-inductive drives. Plasma current can be thus supported by external antennas, like in the *electron cyclotron current drive* (ECCD) and *lower hybrid current drive* (LHCD); by the *Neutral Particle Injectors* (NBIs) and by the so-called *bootstrap current* [13]. The latter is caused by the radial non-uniformity of the magnetic field ($B_\phi \propto 1/R$), which generates

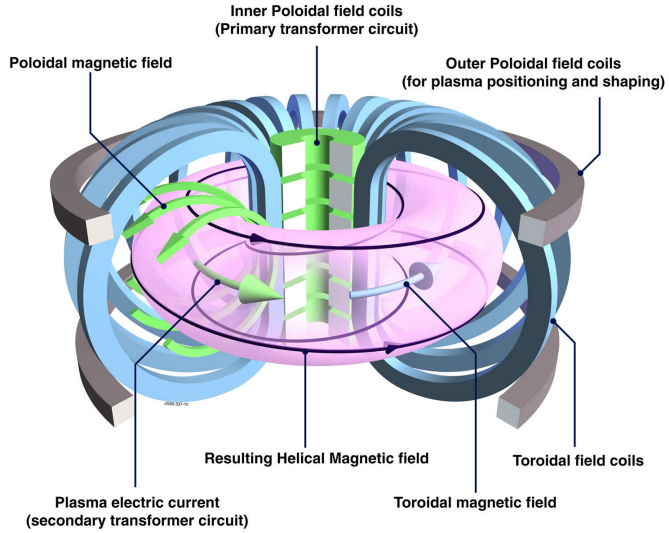

Figure 1.8: Schematic of magnetic coil arrangement in a tokamak device. Credit EUROfusion.

two populations of particles (*trapped* and *passing* particles). The interaction of these two populations generates the bootstrap current. Future tokamak devices are expected to have a large fraction of bootstrap current, which could sustain the plasma confinement for long-time or, ideally, steady-state operations.

1.7.1 Operational limits

As said before, the main aim of a fusion machine is to confine a plasma in such a way the triple product $n_e T_e \tau_E$ is as close as possible to the ignition threshold. However plasma parameters, such as density n, temperature T and confinement time τ_E can not be easily increased because of several limitations related to the appearance of instabilities which reduce or completely destroy the plasma confinement.
The operating electron temperature is fixed at about 20 keV in order to maximize the cross-section of the D-T reaction and, at the same time, minimize radiative losses. Therefore the remaining parameters to be increased are n and τ_E.

Density limit

The maximum density achievable in a tokamak is limited by the so-called *density limit*, which is empirically expressed by the *Greenwald relation*:

$$n_G = \frac{I_p}{\pi a^2} \tag{1.36}$$

where n_G is the line averaged density limit expressed in $10^{20} m^{-3}$, a is the minor radius in m and I_p is the plasma current, expressed in MA. When the line average density exceeds this value, a rapid loss of confinement (*disruption*) occurs.

The physical origin of the density limit is not full understood, but it is now clear that it is related to the plasma edge physics [16, 17, 18]. The density limit involves the cooling of the plasma edge, followed by a steepening of the current profile [14]. For example, the presence of impurities at the plasma edge may increase the line radiation, leading to a local temperature and current density decrease. The resulting steep current profile triggers current-driven instabilities, such as tearing and kink modes, which lead to disruption.

The density limit can be extended by reducing the impurities at the edge, for example by means of wall conditioning, or by fueling the plasma core with particle pellets. The latter allows higher densities at the plasma core, while maintaining low radiative losses at the plasma edge [13].

Current limit

The confinement time τ_E cannot be easily increased as well. A direct measurement of τ_E cannot be done, however, it can be deduced from particle and energy transport. Empirical scaling laws have shown that τ_E scales almost linearly with the plasma current I_p, therefore high current operations are necessary to increase the confinement performances of fusion devices.

However, once again, also the maximum achievable plasma current in a tokamak is limited by the growth of disruptive external ideal kink modes. To be precise, the current limit is a limit on the minimum value of the safety factor

at the edge q_a, in fact the latter can be written, in cylindrical approximation, in terms of the plasma current as:

$$q_a \simeq \frac{2\pi a^2}{\mu_0 R}\frac{B_z}{I_p} \tag{1.37}$$

By means of energy principles, it is possible to show that, in order to have stable operation, the condition $q_a > 1$ must be fulfilled. This condition is known as *Kruskal-Shafranov limit*.
Actually, external kink modes already occur in circular, high aspect ratio plasma at $q_a = 2$, further limiting the maximum plasma current.
This limit can be partially overcome by generating triangular and elongated plasmas, with a typical D-shape, with which higher plasma currents can be obtained.
Moreover, recent experiments on RFX-mod device, operated as tokamak, have shown that $q < 2$ plasmas can be obtained by means of an adequate feedback control system by additional coils [19], opening a new stable operational regime with higher plasma currents [20, 21].

β limit

Furthermore, an additional limit exists, involving the maximum attainable kinetic pressure $p = nT$. This limit is expressed in terms of a limit of the $\beta = \frac{p}{B^2/2\mu_0}$ and it is known as *beta limit*. Sometimes, this limit is alternatively described in terms of the so-called *normalized* β, $\beta_N = \beta\frac{aB_\phi}{I_p}$.
The maximum achievable β is of order of few percentage, beyond which the development of an external kink mode leads to a disruption event. Actually, the maximum beta value changes assuming a plasma without an external wall or in presence of an ideal wall. In the first case, an external ideal kink mode grows if β crosses a threshold called *no wall limit* ($\beta_{no-wall}$). In the presence of an ideal external wall, the instability threshold is higher, and the β can be further increased up to the so-called *ideal wall limit* ($\beta_{ideal-wall}$). If these limits are crossed, the external kink modes grow at a rate that can not be controlled by the feedback system.

In the presence of a resistive external structure, the pressure limit is in the middle of the two above mentioned beta limits [13]. The external ideal kink mode is converted into a RWM in the presence of a resistive wall, and the β limit depends on the wall properties. Two main branches can be recognized: a fast branch, in which the kink mode is characterized by a fast rotation with respect to the wall. At these frequencies, the wall acts as an ideal conductor, stabilizing the mode. In the low branch, the perturbation rotates at a slow frequency with respect to the wall. In this case, the perturbation can penetrate through the wall and become unstable and grows at a fast rate, making the control system useless. The boundary between the two branches depends on the magnetic diffusion properties of the resistive wall.

Hugill diagram

The operational regime of a tokamak can be represented as a limited area in the $(I_p,\langle n_e\rangle)$ plane, where $\langle n_e\rangle$ is the averaged electron density. This is summarized by the so-called *Hugill diagram*, schematized in Fig. 1.9. This diagram shows three main stability limits, beyond which an abrupt plasma termination occurs (disruption) or the confinement is lost in a longer time (soft limit). It shows also how the boundary of the stable operational region can be enlarged through appropriate operations on the plasma and on the external walls.
In this diagram, apart the current and Greenwald limits, a low density limit, labeled as *runaway limit* is shown. If density is low, electrons have few collisions, gaining a big amount of energy from the electric field. These electrons can easily be lost by plasma, causing confinement losses and severe damages to the wall.
Actually this low density limit is not too much important for a fusion reactor, because high density levels must be achieved.

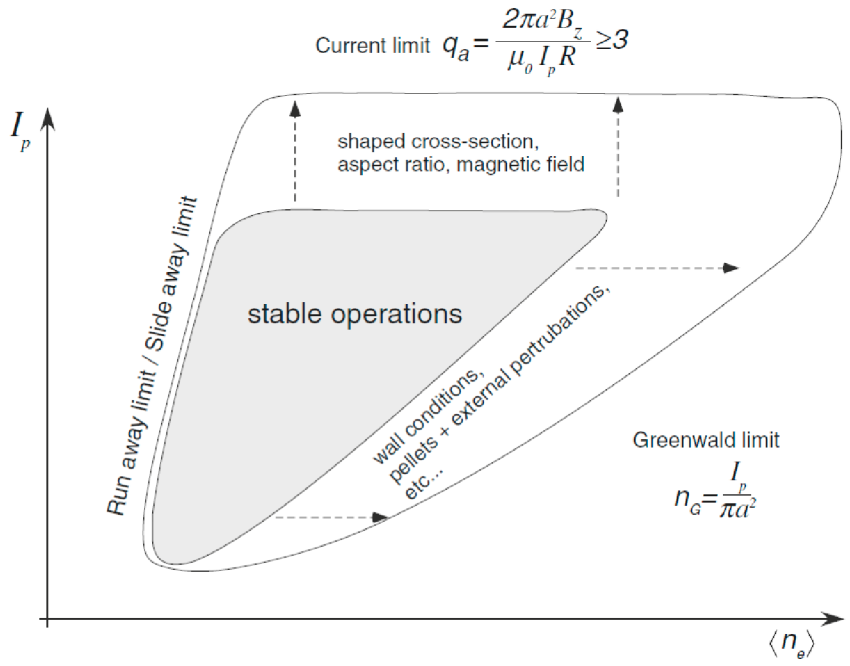

Figure 1.9: Hugill diagram and the main limits for tokamak operations. Taken by [13]

1.8 Reversed Field Pinch

The reversed field pinch is a toroidal axisymmetric configuration for plasma confinement. The poloidal magnetic field is produced by the toroidal component of the plasma current, as in tokamaks, while the toroidal field is produced by both currents flowing in the external toroidal field coils and the toroidal component of the plasma current itself [22]. Differently from tokamak, in which the toroidal field is largely dominant on the poloidal one, in RFP, the magnitudes of toroidal and poloidal magnetic fields are comparable, as shown in Fig. 1.10, which exhibits the radial profiles of the field components for RFP and tokamak. As can be seen, in the RFP configuration, the toroidal magnetic field direction reverses at the edge with respect to that on axis. The safety factor profile is much less than 1 over all the minor radius. The RFP does not thus satisfies the Kruskal-Shafranov criterion (i.e. $q_a > 1$), therefore the plasma current can, in principle, be very high, giving the pos-

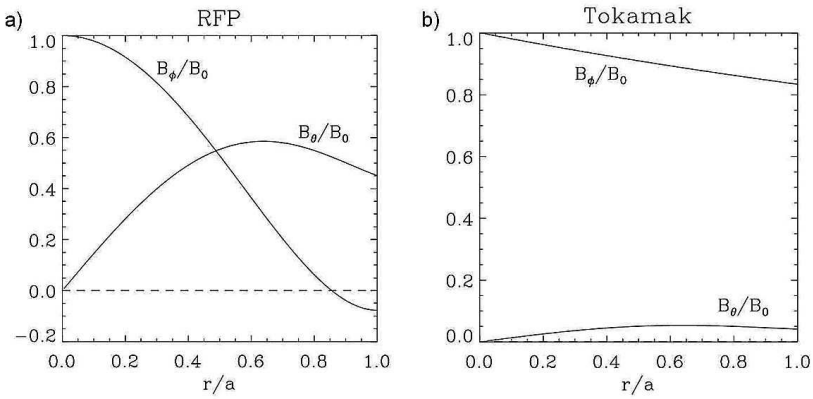

Figure 1.10: Radial profiles of toroidal and poloidal magnetic field components in RFP (a) and tokamak (b). All the quantities are divided by the total equilibrium magnetic field.

sibility to achieve the ignition by Ohmic heating only, without any external additional heating supply.

The q profile in a RFP leads to the growth of several resonant instabilities (tearing modes), generating magnetic islands at multiple radii. RFP plasmas typically exhibit a large population of tearing modes of poloidal mode number $m = 1$ resonant in the plasma core and $m = 0$ resonant at the reversal surface, that is where the toroidal magnetic field reverses. This condition is generally known as *Multiple Helicity* (MH) state. The position where some of these instabilities grow is schematized in Fig. 1.11, the most internal of which being the $m = 1$, $n = 7$ tearing mode. Tearing modes in a RFP are non disruptive, but they usually grow up to a saturation level.

In the standard vision, as will be discussed later, the overlap of the magnetic islands can produce a chaotic region inside the plasma where the magnetic surfaces are destroyed [13]. Because of the chaotic trajectories of the magnetic field lines, the radial transport of particle and energy is high, making the confinement time small. This condition is different from tokamak, where, as said before, the magnetic lines lie on nested surfaces and the radial transport is small.

Two dimensionless parameters are typically used to characterize the RFP magnetic field: the *pinch parameter* Θ and the *reversal parameter* F, respec-

tively defined as follow:

$$\Theta = \frac{B_\theta(a)}{\langle B_\phi \rangle} \tag{1.38}$$

$$F = \frac{B_\phi(a)}{\langle B_\phi \rangle} \tag{1.39}$$

where $\langle B_\phi \rangle$ indicates the toroidal field averaged over the poloidal cross-section. The Θ-parameter measures how much the plasma and the magnetic field are squeezed in the torus, the F-parameter provides an estimation of the toroidal field reversal at the edge. In this context, the tokamak is a low Θ configuration with $F > 1$, while the RFP is a high Θ configuration, with negative values of the F parameters.

1.8.1 Dynamo

If the RFP equilibrium was dominated only by resistivity, then the discharge would be limited over time, in particular the toroidal component of the magnetic field should decay with a time constant given by the plasma resistivity itself [23]. Instead, it is experimentally observed that the RFP configuration is maintained for a much longer time, limited only by the capacity of the external transformers to provide the *loop voltage*. This suggests the idea that there is a mechanism that continually regenerates the toroidal field lost due to resistive diffusion. The toroidal field profile of the RFP configuration

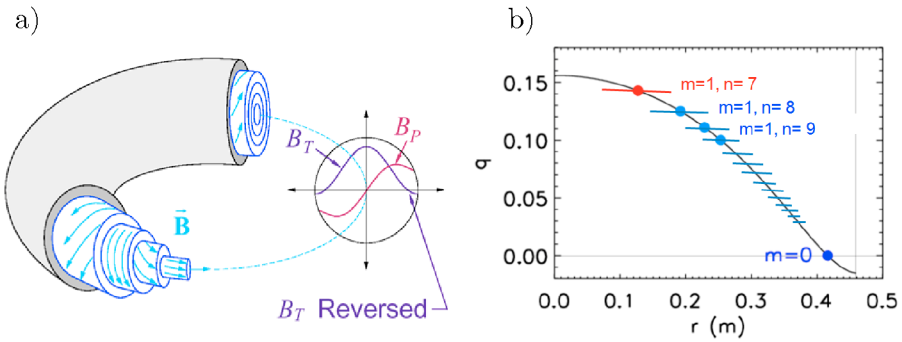

Figure 1.11: a) Schematic of magnetic field line winding at different radii in a RFP plasma. b) Safety factor profile for a typical RFP plasma. The locations of the resistive $m = 1$ and $m = 0$ tearing modes are schematized.

requires a poloidal current density. However, in a RFP, no poloidal electric field is supplied from external systems in stationary conditions. This condition is particularly evident at the reversal surface, where the magnetic field is purely poloidal. In that position, there isn't any possibility to push electrons in the poloidal direction to generate a current if no poloidal electric field is provided. Therefore, some effective electromotive force must exist, keeping the poloidal current density over time. The origin of this force, not yet full understood, is called *dynamo*, as remembering similar processes, taking place in Earth and stars, that generate magnetic field. This process causes the plasma continually relaxing towards a preferred, lower energy state and maintains the RFP configuration as long as the plasma current is sustained. The most used model for describing the dynamo mechanism is that of *MHD dynamo* [22]. According to this model, the so-called *dynamo electric field* $\mathbf{E}_D$ is generated from the nonlinear interaction of MHD instabilities in the plasma [23, 24]. Such instabilities produce velocity fluctuations $\tilde{\mathbf{v}}$ and magnetic fluctuations $\tilde{\mathbf{B}}$ which generate the non-inductive electric field:

$$\mathbf{E}_D = < \tilde{\mathbf{v}} \times \tilde{\mathbf{B}} > \tag{1.40}$$

where $< \cdot >$ denotes an average over the equilibrium flux surface [25].
Hence, although the instabilities represent a big deal for the plasma confinement, they constitute a fundamental factor for the RFP, as their activity sustains the magnetic configuration itself.
Actually, it has been shown that the RFP configuration can be sustained by a single MHD mode. This situation is called *Single Helicity* (SH) and the transition to this state is governed by the Hartmann number [26]:

$$H = (\eta\nu)^{-\frac{1}{2}} \tag{1.41}$$

where η and ν are resistivity and viscosity terms, respectively.

The SH state has never been seen in experiments, however transitions to a intermediate regime in which a single mode ($m = 1, n = n_0$) is dominant over the others, have been observed. The other modes, said *secondary modes*,

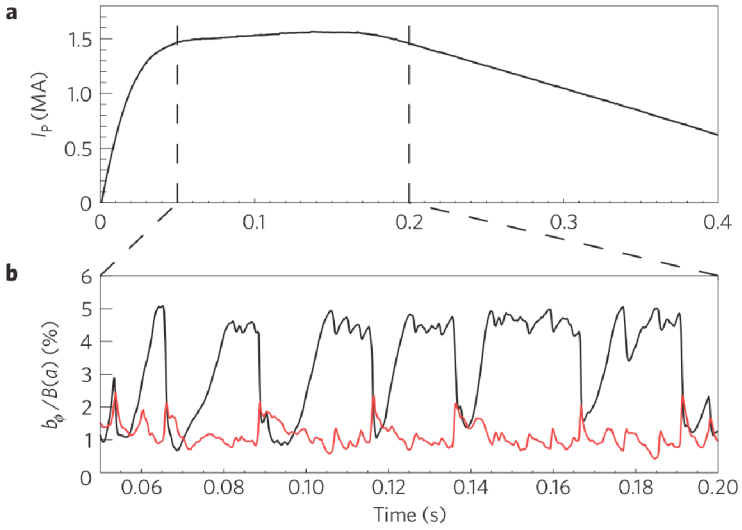

Figure 1.12: (a) Time trace of plasma current for a RFX-mod RFP discharge. The vertical dashed lines delimit the so-called flat-top phase of the discharge. (b) Amplitude time trace of the m=1/n=7 dominant mode (black curve) during the flat-top phase of the discharge, and amplitude of the secondary modes (red curve), the latter being defined as the square root of the sum of each amplitude. The amplitudes are normalized to the average poloidal magnetic field. The system oscillates between two states, one where all of the modes have similar amplitudes (multiple helicity) and another one where there are a dominant mode and secondary ones (QSH). Taken by [27].

don't completely cancel, therefore, this state is known as *Quasi Single Helicity* (QSH) state, to distinguish it from the true SH one.

During a QSH state, the plasma topology evolves creating a helical equi-

Figure 1.13: Schematic of the plasma helical equilibrium formed during a QSH state.

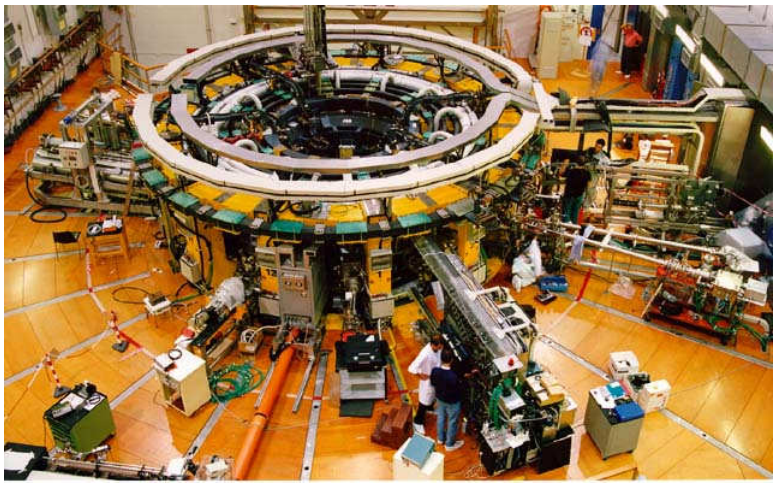

Figure 1.14: Photograph of the RFX-mod facility.

librium in the core, schematized in Figure 1.13, characterized by a higher confinement with internal transport barrier [27].
This new state is sustained for a finite time, therefore quasi-cyclic transitions between QSH and MH states are observed. These transitions are related to magnetic reconnection of field lines, the plasma relaxing to a new, lower energy state. The analysis of the crashes as well as the study of the evolution of the $m = 0$ modes constitutes one of the main topics of this thesis and are presented in chapter 4.

1.9 The RFX-mod machine

The *Reversed Field eXperiment modified* (RFX-mod) is the largest RFP device presently operating in the world, located in Padova, Italy. RFX-mod is a purely Ohmic device, being designed to operate without any additional system for the plasma heating. Its major and minor radii are $R_0 = 2m$ and $a = 0.459m$, respectively.
RFX-mod is the upgraded version of the former RFX device [28] and it is designed to achieve the highest plasma current (2MA) ever produced by RFPs. The RFX-mod plasma is produced inside a small-time constant inconel vacuum vessel ($\tau_v \simeq 1.2ms$, $r_v = 0.5125m$) [29], whose internal wall is entirely

covered by graphite tiles. This *first-wall*, being directly exposed to plasma, has to withstand high thermal loads during the plasma-wall interactions, which locally can reach values of order of tens of MW/m^2 [30]. The plasma is passively stabilized by an external 3mm thick copper shell ($\tau_W = 100ms$, $r_W = 0.5125m$).

RFX-mod has the most advanced system for the feedback control of MHD instabilities [31], made of an array of 4 poloidal $\times$ 48 toroidal independently driven active saddle coils, placed on the outermost support structure ($\tau_s \simeq 24ms$, $r_s = 0.5815m$). The MHD feedback control system makes use of magnetic sensors placed close to the shell inner surface at $r_s = 0.507m$. These sensors are unable to detect high frequency perturbations, because of the screening effect of the vacuum vessel. The detection of high frequency phenomena is done by means of the ISIS diagnostic, a system of probes placed on the vacuum-vessel inner surface. This diagnostic is presented in a detail in chapter 2.

Thanks to the advanced MHD control and to the flexibility of the magnetic coil system, RFX-mod is a unique device able to operate in a wide range of configurations. Reversed field pinch, tokamak and the magnetic configurations between the two, the so-called *ultra-low q* (Ulq) one, have been produced in RFX-mod [31].

The study of plasma in such a wide range of parameters has considerable advantages, such as the understanding of basic physics phenomena, like, for example, that of the density limit.

In RFX-mod, a full set of diagnostics is installed for the measurement, both in time and space, of several physical quantities. The main diagnostic systems that have been used for the experimental analysis, here presented, are described in chapter 2.

In the RFX-mod experiments, in RFP configurations, it has been shown that, when the plasma current is increased, plasma spontaneously transits to ordered helical states. The quasi-cyclic transitions between the QSH and MH states, characterized by fast changes in magnetic topology, make RFX-mod an important laboratory for the study of magnetic reconnection and particle acceleration processes in plasmas.

As a tokamak, RFX-mod has shown the possibility to operate stable discharges at $q_a < 2$, thanks to the suppression of the non-resonant $m = 2, n = 1$ resistive wall modes, by means of a sophisticate magnetic feedback system [19].
RFX-mod is presently shut down since 2015, in order to allow it to be updated. Several enhancements have been proposed in order to increase the number of diagnostics and enhance the machine performances.
All the analysis presented in this thesis refer to experimental data inferred from RFX-mod discharges, in both tokamak and RFP configurations. In particular, the analysis of magnetic reconnection events in RFP plasmas is presented in chapter 4, while the study of tearing mode dynamics in tokamak plasmas in exposed in chapter 5.

Chapter 2

Diagnostics and data analysis

2.1 Diagnostics

The results of the experimental analyzes, presented in this thesis, have been obtained by elaborating the data provided by several diagnostics, of which RFX-mod is equipped.
Most of the activity has been addressed to the study of high-frequency magnetic and electrostatic fluctuations, detected at the plasma edge by means of the probes of the *Integrated System of Internal Sensors* (ISIS). Signals from other diagnostics, briefly described in this chapter, have been analyzed to determine some global plasma parameters and to extrapolate their plasma profiles.
Finally, in paragraph 2.2, the main methods adopted for the experimental data elaboration are presented.

2.1.1 ISIS

The Integrated System of Internal Sensors (ISIS) represents a large set of in-vessel probes designed mainly to detect high-frequency plasma fluctuations [32]. They constitute a diagnostic system able to provide local measurements of several plasma parameters, resolved both in time and space.
ISIS is dedicated to perform calorimetric, electrostatic and magnetic measurements by means of the following sensor arrays:

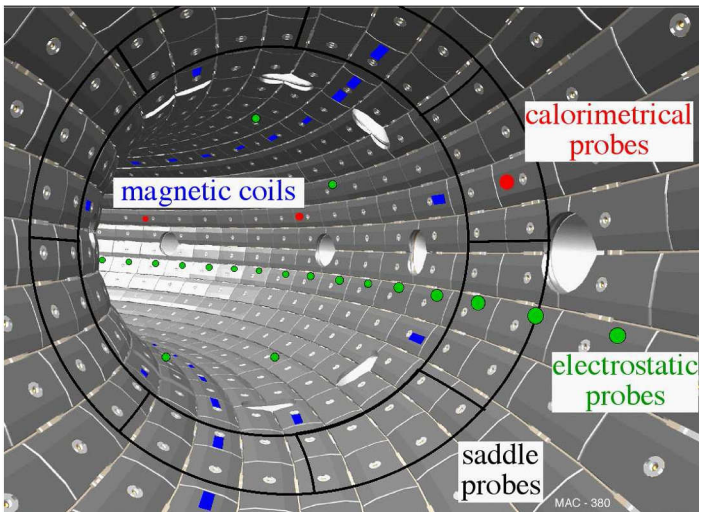

Figure 2.1: Schematic picture of the ISIS sensors

1. **Calorimetric sensors**. They are thermocouples, embedded in the graphite tiles, devoted to measure tiles temperature and study the thermal loads at the first-wall. This ISIS sub-system consists of 8 calorimetric sensors, distributed in a toroidal array (Fig. 2.1). Thermocouples are placed just close to the pumping ports, in order to be easily removed in case of failure [32].
2. **Electrostatic sensors**. This sub-system is made of tungsten electrodes exposed to plasma, measuring the *floating potential* V_f, defined as the bias voltage at which the probe draws no net current [33]. V_f is also the potential of an insulated object immersed into the plasma [34]. Floating potential is strictly related, according to the Langmuir probe theory [33], to the plasma potential V_p through the electron temperature T_e and the plasma ion mass m_i. Electrostatic probes can be also arranged in a triple array, dubbed as 'triple probe', to easily estimate the electron temperature with good time resolution.

   The electrostatic probe system of ISIS consists of 73 single probes and 8 triple probes, organized as follow: a toroidal array of 72 equally spaced single probes, located at $\theta = 19.3°$; a poloidal array of triple probes at the toroidal angle $\phi = 248.6°$, and one single and one triple probe close to a spectroscopic diagnostic for calibration purposes [35]. Elec-

trostatic data are acquired with a sampling frequency up to 20 MHz, with a bandwidth up to 2 MHz.

3. **Magnetic sensors**. This subset is composed by pick-up and saddle coils [36], measuring the time derivative of the magnetic field $\dot{\mathbf{B}}$, through the Faraday-Neumann's law:

$$V = -\frac{d\Phi_B}{dt} = -\frac{d(\mathbf{B}\cdot\mathbf{A})}{dt} = -\dot{\mathbf{B}}\cdot\mathbf{A} \tag{2.1}$$

where V is the voltage induced at the coil endings, Φ_B is the magnetic flux, B the magnetic field, $A = nA_0$ is the total area of the coil, being n the number of wire turns and A_0 the area of a single winding. The magnetic field fluctuations, B, can be obtained by means of a numerical integration of $\dot{B}$ over time.

The in-vessel magnetic probes are located behind the graphite tiles and represent the only magnetic diagnostic system able to detect high-frequency magnetic fluctuations, due to the screening effect of the vacuum vessel and the copper shell (basically a low-pass filter) on the external magnetic sensors.

ISIS magnetic sensors are distributed in several arrays, as follow:

- two toroidal arrays of 48 $\dot{B}_\varphi$ pick-up probes each, uniformly distributed along the toroidal direction and located at diametrically opposite poloidal angles ($\theta_1 = 289.3°$ and $\theta_2 = 109.3°$)
- one poloidal array of 8 $\dot{B}_r$ saddle probes, located at $\varphi = 215°$;
- one poloidal array of 8 $\dot{B}_\theta$ pick-up coils, located at $\varphi = 216.2°$;
- one poloidal array of 8 $\dot{B}_\varphi$ pick-up coils, located at $\varphi = 208.7°$;
- one partial poloidal array of 6 $\dot{B}_\varphi$ pick-up coils, at $\varphi = 28.9°$;
- a cluster of 8 $\dot{B}_\varphi$ pick-up coils for turbulent structure study;
- a cluster of 8 $\dot{B}_\theta$ pick-up coils for turbulent structure study.

The cable that constitutes the pick-up coils, made in Chromel, is wrapped in two layers for a total of eight turns around an elliptical ceramic material (MACOR). The sampling frequency for the magnetic measurements from the ISIS system is 2 MHz, with an estimated bandwidth up to 400kHz [32].

For the analysis presented in this thesis, the two toroidal $\dot{B}_\varphi$ arrays and the poloidal $\dot{B}_\theta$ and $\dot{B}_r$ ones have been used. Note that the study of modes with m poloidal mode number is limited to $m \leq 4$, according to the Nyquist-Shannon theorem, discussed in next paragraph 2.2.1, because ISIS has only 8 probes along the poloidal direction; instead it is possible to study modes with toroidal mode number n up to 24. This probe distribution was chosen, in the ISIS design phase, because, in RFP configuration, the RFX-mod plasmas are characterized by several tearing modes with high toroidal mode numbers (mainly $m = 1$ and $n = 7 - 15$ for RFX-mod aspect ratio) [32]. At that time, tokamak operations were not yet foreseen.

2.1.2 U-probe

An insertable probe, called *U-probe*, is used in RFX-mod to perform measurements of magnetic and electrostatic fluctuations at the plasma edge. This diagnostic is made of two cases, separated 88mm. It is installed on the equatorial plane on the low field side of the machine. Because of the high heat loads during the plasma discharge, this diagnostic cannot be inserted for more than 10% of the plasma radius.
Each case include a 2D array of Langmuir probes, separated 6mm each other, for the electrostatic measurements, and a radial array of tri-axial magnetic coils, measuring the time derivative of magnetic fluctuation along the three directions. These probes are analogous to those installed on the ISIS system, therefore no further explanation of these devices is given. The maximum sampling frequency is 10MHz, with a bandwidth up to 3MHz.
A schematic of this diagnostic is presented in Fig. 2.2.

2.1.3 Neutron and gamma detector

The magnetic reconnection processes, as already said, are often associated with acceleration and heating of charged particles in plasma. The rate of D-D fusion reactions increases with the temperature, therefore, plasma heating

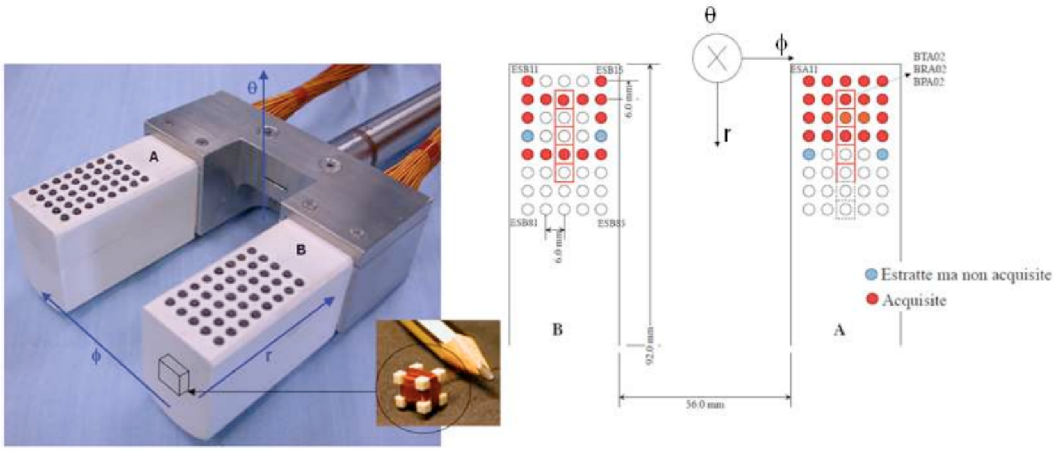

Figure 2.2: Schematic view of the U-probe and distribution of electrostatic and magnetic probes.

in a localized region could lead to a local increase of the number of reactions and therefore also to an increase in the neutron production.

In order to study the flow of neutrons emitted by the RFX-mod plasma, a compact spectrometer has been used. This instrument is placed on the top of the vacuum chamber above the toroidal axis, in a position $R = R_0 = 2m$, as shown in Figure 2.3. This diagnostic uses a liquid scintillator EJ-301 [37] (diameter 51 mm, thickness 51 mm) coupled to a H8500 photo-multiplier [38]. The neutron and gamma radiation sensitive scintillator is placed 260 mm above a window and protected by a polyethylene screen, which acts as collimator.

Discrimination between photons and neutrons is determined on the basis of a standard method, dubbed as *Pulse Shape Discrimination*, distinguishing different types of particles on the basis of the signal shape produced by delayed fluorescence [39]. The detector has been energy calibrated by using small radioactive sources (^{137}Cs and ^{60}Co) emitting gamma rays of known energy.

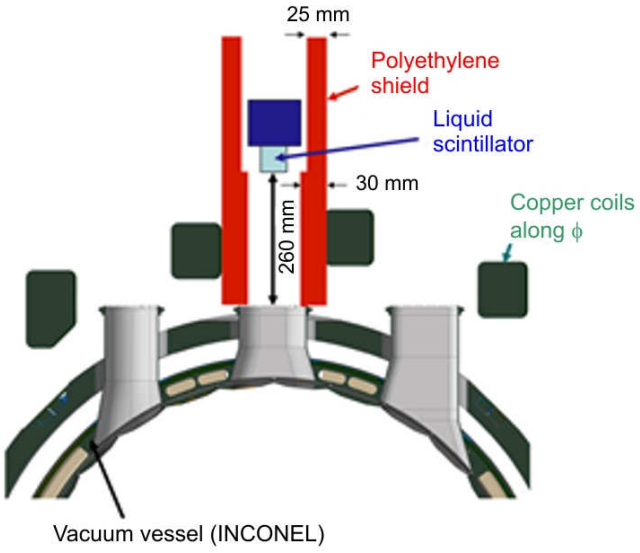

Figure 2.3: Schematic of the neutron and gamma detector in RFX-mod

2.1.4 Neutral Particle Analyzer

Fast neutral particles can be generated in the plasma due to charge-exchange processes between fast ions and cold neutrals. In this process, a fast ion A and a cold neutral atom B collide, exchanging in the reaction their electric charge state:

$$A^+ + B \rightarrow A + B^+ + \Delta E \tag{2.2}$$

in which the symbol $^+$ denotes the ionized particle and ΔE is the difference between the ionization potentials of A and B [40].
The resulting fast neutral particles are not confined by the magnetic field, so they can get out of the reactor. They can be detected and their energy distribution function, which reflects the energy distribution of the ion component, can be measured by a Neutral Particle Analyzer (NPA) [41]. The fast atoms escaping the reactor vessel enter at first into a gas target, where they are ionized by stripping collisions. The resulting ions, with the same energy as the primary neutrals, are deviated by a magnetic and electrical

field and spatially distributed according to their mass and velocity. Finally, they are collected by an array of detectors (photocatodes coupled to photomultipliers). Each detector measures ions in a narrow range of energies. From the resulting energy distribution function, the ion temperature can be extrapolated (assuming a Maxwellian distribution).

2.1.5 Pressure profile measurements

The analysis performed on the RFX-mod tokamak plasmas has required the knowledge of the radial electron pressure profile $p_e(r) = n_e(r) \cdot T_e(r)$, being the pressure p the product of density n and temperature T. The pressure profile estimations, presented in this thesis, have been deduced by means of two different devices: a *Thomson scattering* diagnostic, for the electron temperature measurements, and an *Interferometer*, for the density profile estimation. Both diagnostics are here briefly described.

Thomson scattering diagnostic

Thomson scattering (TS) is the elastic scattering of an electromagnetic radiation by means of a charged particle [7]. When an electromagnetic wave impinges on a charged particle, the electric and magnetic components of the wave exert a Lorentz force on that particle. Thus, the particle is accelerated and, consequently, emits radiation in all directions. This emitted radiation is the scattered wave [41]. Because of the particle velocity, the scattered radiation is also subject to a Doppler shift. Therefore, given a monochromatic electromagnetic radiation, the scattered light energy distribution reflects that of the particles. For a thermalized population of charged particles, it is possible to estimate the temperature by measuring the energy distribution width. Because the ions are much heavier than the electrons, their acceleration and hence radiation is usually small enough to be negligible. This is why TS diagnostic mainly measures radiation scattered by electrons.
The RFX-mod Thomson scattering diagnostic makes use of a Nd:YLF laser to produce the coherent monochromatic radiation ($\lambda = 1053nm$). The scattered wave is detected, after being collected by a optic fiber system, by means

of an array of avalanche photo-diodes [42]. The RFX-mod TS diagnostic provides data on 81 spatial points disposed radially on the chamber equatorial plane. The spatial resolution is about 10 mm and profiles are sampled every 10 ms [43].

Interferometer

An interferometer is a device in which two or more waves can interfere, generating a resulting wave whose amplitude depends on the phases of the incident waves [41]. This device is usually used in plasma physics to determine the plasma density. It uses a laser beam that is divided into two beams by means of a beam splitter. The first one, called *scene beam*, passes through the plasma, while the other one, called *reference beam*, travels on the same optical path outside the plasma. Then the two beams recombine together

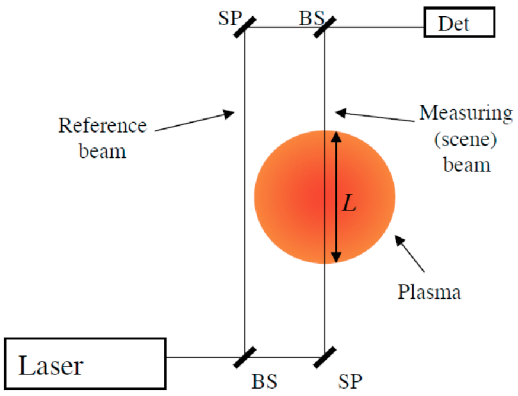

Figure 2.4: Schematic of the interferometer diagnostic. A laser beam is splitted in two beams, one of which passes through the plasma, the other traveling the same path outside the plasma. The two beams recombine together and detected for phase measurements. In RFX-mod a two-color laser system is used [44].

and the merging beam is detected in order to be analyzed. The plasma density can be inferred from the output of the interferometer, knowing that the change in the phase of the scene beam is proportional to the electron density integrated on the path along the plasma.
There are different types of interferometer, which basically differ according

to the path of the beams and the number of beams and beamsplitters. RFX-mod interferometric device makes use of a Mid-Infra Red (MIR) multi-chord CO_2 interferometer [44], using two main chords modules. In the present configuration, the module A measures the central zone of the plasma with 8 horizontal or nearly horizontal chords, whereas module B, made of 6 chords, is mainly dedicated to the outer plasma region on the low field side.
The density profile is computed by the inversion of the interferometer data, by means of a numerical code on the magnetic flux coordinate [45].

2.1.6 Soft X-rays

In a thermonuclear plasma, the temperature of about $1keV$ leads to a radiation emissivity with a maximum in the energy range of the *soft X-rays* (sxr). In a fully ionized plasma, this radiation comes only from the continuous bremsstrahlung, but, in the presence of non-totally stripped impurities, plasma emits also characteristic line radiations.
The sxr radiation is a strong function of the electron density n_e and electron temperature T_e. In the absence of line radiation, the plasma sxr emissivity is proportional to $n_e^2\sqrt{T_e}$.
In the RFX-mod device, such a radiation is detected by a large system of PIN photo-diodes, acting as radiation-current converters. The photon impinging on the diode produces a number of electron-hole pairs, giving rise to a current proportional to the photon energy. These detectors look at the plasma through a pin-hole, along a narrow cone of observation, called *line-of-sight*. The photon hitting the detector comes from plasma in this volume. A large number of photo diodes, looking at different line-of-sights, are used to maximize the observed plasma volume [46]. Tomographic algorithms are used to reconstruct the plasma emissivity distribution of plasma, from which useful information of various properties can be derived, for example about plasma equilibrium, the impurity content or the presence of turbulence in the plasma core [46].
In the present thesis, only in-axis sxr measurements are taken into account, in order to identify any presence of unstable modes, particularly in the plasma

core, such as the sawtooth instability, discussed in paragraph 3.3.2.

2.2 Data analysis techniques

In this section, the main techniques adopted for the data analysis presented in this thesis are briefly described.
Since the main interest concerns the analysis of the rapid changes and fluctuations of physical quantities, such as the magnetic fluctuations at the plasma edge, it is necessary to adopt a proper representations of signals, collected by the different diagnostics as a function of time, and analysis methods.
The representation of these signals in the time-amplitude plane is not always the best representation of a signal, being most of information hidden in the frequency content of the signal. Therefore, the amplitude-frequency and the time-frequency representations, here discussed, can provide detailed information about the behavior of many physical quantities. In the following, short notions about the well-known Fourier transform, widely used for almost all the analysis carried out, are given. Next, a description of the wavelet transform, which represents an important tool for the study of intermittent signals, is also provided.

2.2.1 Fourier transform

The continuous Fourier Transform (CFT) is a mathematical technique that decomposes a signal x(y), defined in $(-\infty, +\infty)$, in terms of trigonometric functions (sin and cos), or, equivalently, in terms of plane waves ($e^{i2\pi\zeta y}$) [47]. The CFT is defined as follow:

$$\hat{x}(\zeta) = \int_{-\infty}^{+\infty} x(y) e^{-i2\pi\zeta y} dy \tag{2.3}$$

As the independent variable y represents time (in seconds), the transform variable ζ represents frequency (in hertz); similarly, when y represents the space (m), ζ represents the wave number k (m^{-1}).
From here on, use is done, for simplicity, of the temporal variable t as an

independent variable, hence the previous formula becomes:

$$\hat{x}(f) = \int_{-\infty}^{+\infty} x(t) e^{-i2\pi ft} dt \tag{2.4}$$

With a similar expression, $x(t)$ can be determined back by $\hat{x}(t)$, trough the *inverse Fourier transform*:

$$x(t) = \int_{-\infty}^{+\infty} \hat{x}(f) e^{i2\pi ft} dt \tag{2.5}$$

Since the basis $e^{-i2\pi ft}$ is characterized by a definite frequency, then $\hat{x}(f)$ possesses the frequency content of the original signal $x(t)$, that is its *frequency spectrum*. However, in $\hat{x}(f)$, all the time information are lost, so the Fourier transform of a $x(t)$ signal varying over time isn't able to say when some frequency component appears in the original signal. Therefore, the CFT is a good analysis tool for stationary signals, whose spectral frequency distribution does not vary over time.
The energy content E of a signal can be calculated, in terms of $x(t)$ or, equally, in terms of $\hat{x}(f)$, according to the equivalence of time and frequency representation (Parseval's theorem), as:

$$E = \int_{-\infty}^{+\infty} |x(t)|^2 dt = \int_{-\infty}^{+\infty} |\hat{x}(f)|^2 df \tag{2.6}$$

hence $|\hat{x}(f)|^2$ can be interpreted as a energy density, that is the energy per unit frequency contained in the signal at the frequency f.

Discrete Fourier Transform

The CFT can be applied to a signal that is continuous in time. Nevertheless, this is not the case for experimental signals, which are measured discreetly, both in time and space. For this reason, the CFT cannot be applied to such signals. Experimental signals are nothing but a sequence of N discrete values of a continuous function, measured every time interval Δt, which is the *sampling period*, for a total time T.

The *Discrete Fourier Transform* (DTE) applies to such sampled signals, returning a same length sequence of samples $f_n = n\Delta f$ in the frequency domain, where $\Delta f = 1/T$. In this framework, if $x_j = x(j\Delta t)$, with $j = 0, 1, ..., N$, is the sampled signal, then equations (2.4),(2.5) must be replaced by the following equations, representing respectively the DTE and its inverse, in which the integral is approximated to a discrete summation [34]:

$$\hat{x}_n = \sum_{j=0}^{N-1} x_j e^{-i2\pi jn/N} \tag{2.7}$$

$$x_j = \sum_{n=N/2}^{N/2} \hat{x}_n e^{i2\pi jn/N} \tag{2.8}$$

The DFT represents the most important tool for the analysis of experimental data in the frequency domain. Since calculation of equations (2.7),(2.8) is performed by computers, several algorithms are used, among which the most known is the *Fast Fourier Transform* (FFT) [48]. Nowadays, DFT and FFT terms are used almost interchangeably.

Nyquist-Shannon theorem

In order to reconstruct the original signal from sampled measurements without losing information, attention must be paid to the sampling frequency, according to Nyquist-Shannon's theorem. According to this theorem, if Δt is the sampling period of a signal, then $f_N = \frac{1}{2\Delta t}$ is the maximum frequency that can be reconstructed in a signal. Equivalently, the minimum sampling rate necessary to prevent loss of information, in the reconstruction of the original analog signal, is equal to twice its maximum frequency. This means that, if frequencies larger than f_N are presented in the analog signal, there is the production of frequencies that do not belong to the original signal, namely artifacts (i.e. spurious frequencies) appear in the reconstructed digital signal. This phenomenon is known as *aliasing*. Figure 2.5 shows an example of aliasing due to insufficient frequency sampling. The original signal is shown as a blue curve, while the red one represents the signal reconstructed on the

basis of the sampled values (black points).

Aliasing occurring in signals sampled over time is referred to temporal

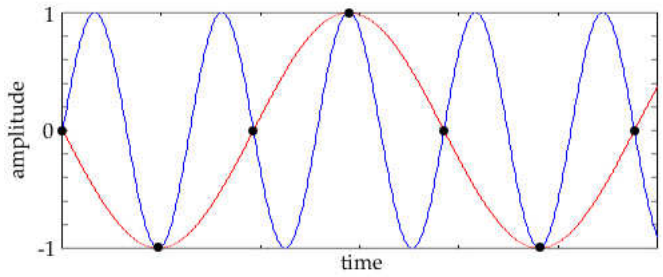

Figure 2.5: Incorrect reconstruction (red curve) of a signal (red) by means of insufficient frequency sampling. The black points are the sampled values.

aliasing, while that occurring in spatially sampled signals is known as spatial aliasing. It can be shown that any spectral component with frequency f in the range $[mf_N, (m+1)f_N]$, with m an integer number, appears in the spectrum at the frequency $f_N - f$. So, it is important to sample the signal at the Nyquist frequency f_N or to properly filter the signal in order to prevent the appearance in the spectrum of artifacts, with no physical meaning.

Short Time Fourier transform

As mentioned before, the Fourier transform doesn't provide any temporal information for each spectral component. Many signals have a energy distribution that varies both in time and frequency. Therefore, when both the time localization and the frequency content of a signal must be known, it is useful to perform a transformation that gives the so-dubbed *time-frequency representation* [49], such as the *Short Time Fourier Transform* (STFT). The procedure requires to divide a signal into N segments of equal length T and calculate the Fourier transform separately on each interval, considered as a independent realization of the considered process. The signal is firstly multiplied by a window function w, which is different from zero only for a period T, and the resulting slice of the original signal is Fourier transformed. These slices usually overlap each other, in order to reduce artifacts at the boundary. Here again, one can distinguish between the continuous and the discrete case.

In the former, the transform can be mathematically expressed as:

$$\hat{x}(\tau, f) = \int_{-\infty}^{+\infty} x(t)w(t-\tau)e^{-i2\pi ft}dt \tag{2.9}$$

where the Fourier transform $\hat{x}(\tau, f)$ is a complex function representing the amplitude and phase of the signal as a function of time and frequency. In the discrete case, the integral is replaced by a summation, hence the STFT can be expressed as:

$$\hat{x}(m, f) = \sum_{j=-\infty}^{+\infty} x_n w_{n-m} e^{-i2\pi jn/N} \tag{2.10}$$

The best way to represent the result of STFT is given by the *spectrogram*. The most common format is a color-coded contour plot, showing time along the horizontal axis and frequencies along the vertical. The third dimension refers to the squared magnitude of the STFT of the signal, being defined as:

$$S(\tau, f) = |\hat{x}(\tau, f)|^2 \tag{2.11}$$

The STFT and its spectrogram are however limited in resolution due to the principle of indetermination. This is because, by choosing narrow window functions, a good time resolution (window time position) can obtained but low resolution in frequency; larger windows, on the contrary, are associated with good frequency resolution, but the time-resolution is low. So the STFT analysis of the experimental data requires a careful selection of the win-

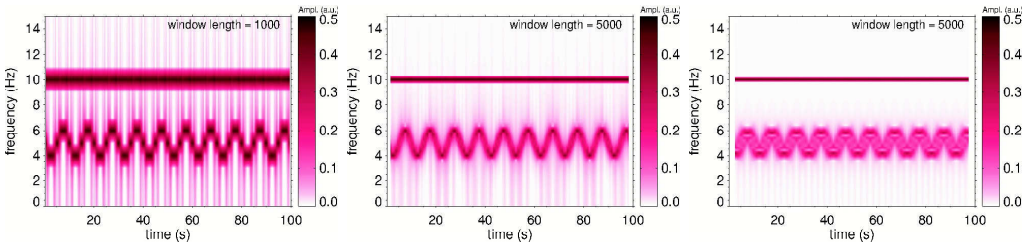

Figure 2.6: Three examples of spectrogram, with different window length. The STFT is applied on the function $y = sin(2\pi f_1 t + 10cos(2\pi f_2 t)) + cos(2\pi f_3 t)$, with $f_1 = 5Hz$, $f_2 = 0.1Hz$, $f_3 = 10Hz$.

dow function width, in order to get the right compromise between time and frequency resolution. This can be shown in Figure 2.6, showing the Fourier spectrogram of the function $y = sin(2\pi f_1 t + 10cos(2\pi f_2 t)) + cos(2\pi f_3 t)$, with $f_1 = 5Hz$, $f_2 = 0.1Hz$, $f_3 = 10Hz$ and t representing the temporal independent variable. It is evident, as the window length changes, the temporal and frequency resolutions change as well.

Wavenumber-frequency representation

Another useful signal representation can be made if a certain physical quantity is sampled over time in different spatial locations. This representation, which provides the frequency content as a function of the wave number k, is called *wavenumber-frequency representation*. Such a representation can be useful in estimating the dispersion relation $k(f)$ of fluctuating quantities in the system or identifying the frequency of a particular fluctuation with wave number k.

This tool is used to analyze the signals coming from the circular arrays of

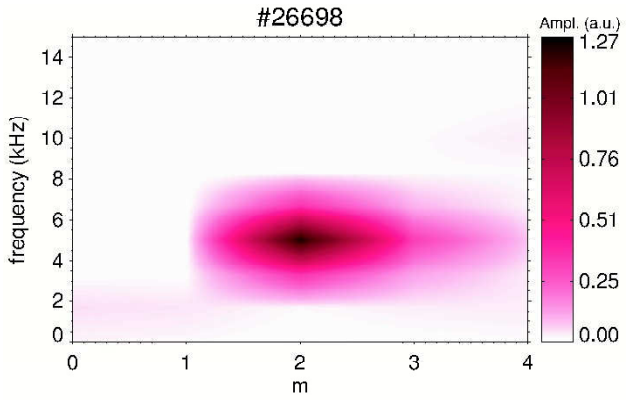

Figure 2.7: Example of wavenumber-frequency representation of the radial magnetic fluctuations measured by ISIS for the tokamak discharge #26698 at a certain time interval.

the equally-spaced ISIS coils. In practice, amplitude $A_p(t)$ and phase $\Phi_p(t)$ of the magnetic fluctuations of RFX-mod plasmas are determined by applying the STFT to the N signals of an array at each time sample. These quantities

are related to the signal $x(\alpha, t)$ measured at angle α by the relationship:

$$x(\alpha, t) = \sum_{p=0}^{N-1} A_p(t) cos[p\alpha + \Phi_p(t)] \tag{2.12}$$

Figure 2.7 shows an example of wavenumber-frequency representation of the poloidal magnetic fluctuations measured by the 8 poloidal coils of the ISIS system for a RFX-mod discharge in tokamak configuration. As can be seen, at this time interval, the plasma is characterized by a main magnetic fluctuation with poloidal mode number $m = 2$ with a frequency $f \sim 5kHz$.

2.2.2 Wavelet Transform

A tool for the time-frequency analysis of signals, alternative to the STFT, is represented by the *Wavelet transform*. This method decomposes a signal in terms of time limited functions (from which the term wavelet, coming from the French *ondelette*, meaning small wave).
The main feature of the Wavelet transform is the use of variable width window functions, which make it different from the STFT that uses fixed window functions. Therefore, the above mentioned resolution problem of the STFT can be partially solved with wavelet analysis, which uses adaptive windows, although, it must be noted, the indeterminacy principle can not be completely eliminated. However, the wavelet analysis, presented in this thesis, has been performed only for the study of intermittent fluctuations in RFP discharges, while the signal frequency studies have been performed with standard STFT.

Wavelet definition

In the wavelet transform, the signal is expressed by combinations of *daughters wavelet*, obtained by shifting and scaling operations on the same *mother wavelet*. A wavelet is a function $\Psi(t)$, satisfying the *admissibility* condition, which is basically equivalent to assume that $\Psi(t)$ is an integrable function with a mean null value, and the *similarity* condition, meaning that a wavelet

function can be obtained by translation and dilation of only one mother wavelet [50].
There are several functions that can be used as mother wavelet and their use depends on the type of analysis one intends to do. In this thesis, use has been made of the *Maar* wavelet or *Mexican hat* function (Figure 2.8). This

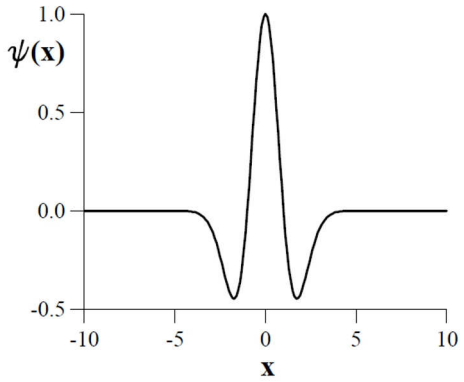

Figure 2.8: Wavelet *Mexican Hat* ($\sigma = 1$)

real function, that is the second derivative of the Gaussian function, can be written as:

$$\Psi(t) = \frac{2}{\pi^{\frac{1}{4}}\sqrt{3\sigma}} \left(\frac{t^2}{\sigma^2} - 1 \right) exp(-\frac{t^2}{2\sigma^2}) \tag{2.13}$$

where σ is the characteristic width of the Gaussian.
The wavelet transform is defined as the integral of the signal $f(t)$ multiplied by the scaled and shifted daughter wavelet [51]:

$$C(\tau, s) = \frac{1}{\sqrt{s}} \int f(t) W \left(\frac{t - \tau}{s} \right) dt \tag{2.14}$$

where s is the scale factor, τ is the shifting factor, t is the time. The continuous wavelet transform is then a convolution of the input data signal with a set of functions generated by the mother wavelet.
The coefficients $C(\tau, s)$ represent the temporal behavior of the characteristic fluctuations at each scale s, or, in other terms, fixed the scaling and shifting factors, the coefficients give the "similarity" between a portion of the signal and the wavelet. Each coefficient thus allows a decomposition of the signal

to the scale s as a function of the time parameter τ.

Intermittency detection

Wavelet transform can be used as a basis of an analysis tool for detection of intermittent structures in a turbulent signal. This recognition method consists in selecting those structures in the signal associated with those $C(\tau, s)$ coefficients that deviate from the gaussianity condition. It is in fact proven that the probability distribution function (PDF) of the fluctuations in a signal has the same scaling of the PDF of wavelet coefficients [52].
It is possible to define a *Local Intermittence Measurement* (LIM) characterizing the activity in the signal at each scale s and at time τ [50]:

$$l(\tau, s) = \frac{C(\tau, s)^2}{\langle C(\tau, s)^2 \rangle} \tag{2.15}$$

where the $\langle\rangle$ symbol refers to the temporal average.
A non-intermittent signal has $l(\tau, s) = 1$ for each τ and s, instead, $l(\tau, s) > 1$ means that the signal has fluctuations greater than the average value at the s scale.
The recognition method assumes to take as intermittent events those that exceed a certain threshold value of the LIM for each scale, that is those values for which the *flatness* parameter

$$F(s) = \frac{\langle C(\tau, s)^4 \rangle}{\langle C(\tau, s)^2 \rangle^2} \tag{2.16}$$

is greater than 3 [52].
Figure 2.9 shows the time trace of the reversal parameter F for a typical RFP discharge in RFX-mod. The vertical lines identify the intermittent structures in the signal, detected at the scale factor $s = 1.25ms$. Further details will be provided in chapter 4, which describes the analysis of experimental data based on this method.

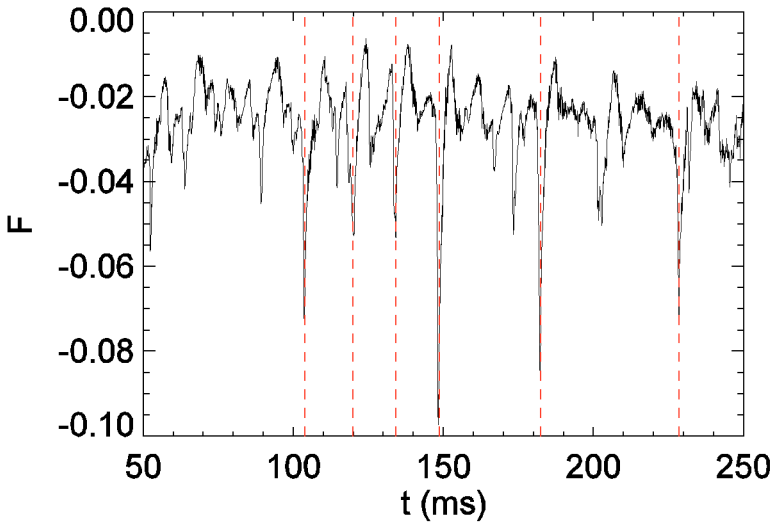

Figure 2.9: Time trace of the reversal parameter F for a RFP discharge. The identified intermittent structure, at the scale $s = 1.25ms$ are highlighted by vertical lines.

Signature wavelet

A new wavelet-based method, recently proposed, has been implemented for the analysis of non-regular signals. This tool, which exclusively uses the sign of the complex wavelet coefficients C, is called *signature* [53] and it is defined as:

$$\sigma f(\tau) \equiv \lim_{s\to 0} sgn\langle f, C_{s,\tau}\rangle \equiv \lim_{s\to 0} \frac{\langle f, C_{s,\tau}\rangle}{|\langle f, C_{s,\tau}\rangle|} \tag{2.17}$$

The complex-valued quantity $\sigma f(\tau)$ is the signature of the function f at location τ. This quantity can be interpreted as an indicator of the local regularity of a signal. More precisely, the signature equals to zero at sufficiently regular points, whereas it is non-zero at salient points, such as jump and cusp, where it assumes purely real and purely imaginary values, respectively.
When a sampled signal has to be analyzed, only a finite number of scales $[s_j]_{j=1}^N$ can be used. Hence, for pratical applications, the following quantity

$$\bar{w}_\tau \equiv \frac{1}{N}\sum_{j=1}^{N} sgn\langle f, C_{s,\tau}\rangle \tag{2.18}$$

is taken into account, where $sgn(\bar{w}_\tau)$ gives an estimate of $\sigma f(\tau)$. In particular, $|\bar{w}_\tau|$ is non-zero if it exceeds an empirical threshold parameter ε $(0 < \varepsilon < 1)$. Therefore, the estimate of the discrete signature takes the form:

$$\sigma f(\tau) \equiv \begin{cases} sgn(\bar{w}_\tau) & |\bar{w}_\tau| \geq \varepsilon \\ 0 & elsewhere \end{cases} \tag{2.19}$$

An example of application is presented in Fig. 2.10, showing a triangular waveform and the $|\bar{w}_\tau|$ parameter, estimated with only 20 wavelet scales. It is possible to observe that $|\bar{w}_\tau|$ is large at the discontinuities, whereas it is small in regular points.

In the analysis reporter in this thesis, the discrete signature tool has been used to localize the step-like points in experimental signals, such as those found during sawtooth instabilities in tokamaks.

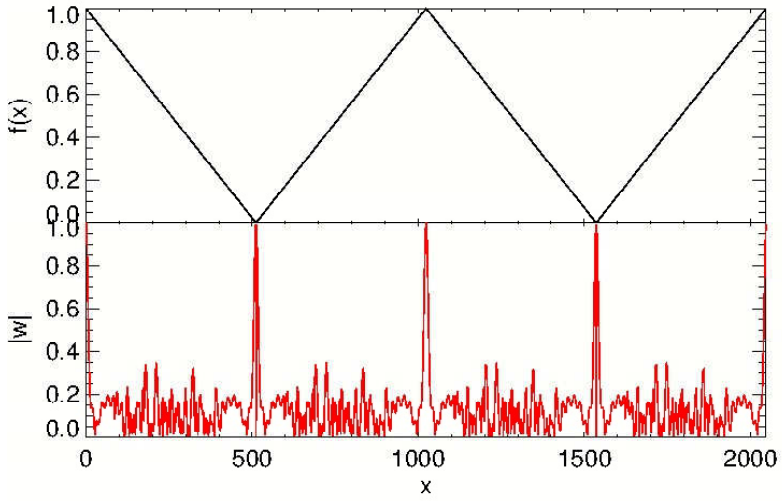

Figure 2.10: The discrete signature of a triangular waveform. It is possible to observe that $|\bar{w}_\tau|$ is large at the discontinuities, whereas it is small at regular points.

Chapter 3

Magnetic Reconnection

3.1 Introduction

Magnetic reconnection is a topological rearrangement of the magnetic field lines in a plasma [54, 55, 56]. When this fundamental process takes place, magnetic energy is converted into kinetic energy through heating and acceleration of charged particles [57]. Magnetic reconnection is as ubiquitous as plasma itself, playing a key role in a wide range of phenomena, such as solar flares[1], the *Coronal Mass Ejections*[2] (CMEs), the interaction between the solar wind and the Earth's magnetosphere[3] [57]. It occurs also in laboratory plasmas, such as in sawtooth activity in tokamak and in the relaxation processes in RFP plasmas. Furthermore, because this process changes the magnetic topology, the generation and dynamics of magnetic fields in stars, accretion disks and galaxies require magnetic reconnection [59].

The concept of magnetic reconnection has its origin in the attempts to understand the huge amount of energy (up to 10^{25} J) released in solar flares. These phenomena occur in a very short time, of order of minutes or hours

[1] A solar flares is a violent explosion on the Sun's surface. It manifests as a sudden flash of brightness, persisting for a few seconds to a few hours. In this event, a large amount of energy stored in the magnetic field is released [58].

[2] A Coronal Mass Ejection is a large expulsion of plasma and magnetic field outwards the Sun, generating the so-called *solar wind*.

[3] A magnetosphere is the region around a planet dominated by the planet's magnetic field.

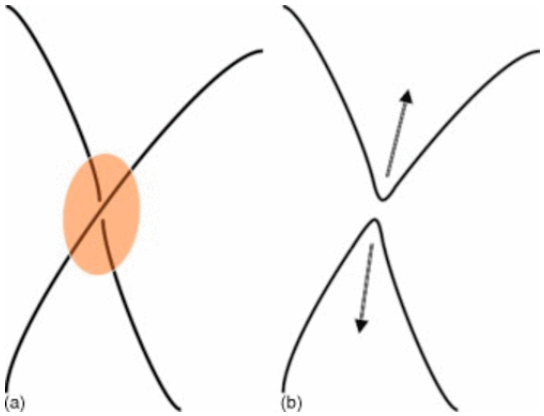

Figure 3.1: Schematic view of breaking and reconnection of field lines. Taken by [57].

[58]. A simple estimate of the resistive decay time of the magnetic field indicates that a direct conversion of magnetic energy by ohmic dissipation would take several years [57]. This has suggested that a mechanism for fast conversion of magnetic energy into kinetic energy and heat must exist.
Giovanelli [60] and Hoyle [61] suggested that magnetic X-type null points (that are the regions of space where magnetic field is zero and the field lines draw a X) may be locations for acceleration and heating of charged particles in solar flares. Dungey [62] showed that a current sheet can be formed in a X-type null point by the collapse of the magnetic field. He was the first to suggest that 'lines of force can be broken and rejoined' in the current sheet (Fig. 3.1). After this topological variation, the two freshly connected lines accelerate the plasma outside this sheet, which is called *neutral sheet* or *diffusion region* [63].
From those early work on solar flares, the collaboration between laboratories and astrophysical research communities has made impressive progresses on the knowledge of magnetic reconnection, nevertheless a complete and detailed understanding of this phenomenon as a whole is still missing.
The study of magnetic reconnection must still solve four main key problems [56]:

- *Rate problem*: most of the theories often predict reconnection rates much slower than those deduced from experimental observations. The

understanding of the mechanisms that drive a fast magnetic reconnection is needed;

- *Trigger problem*: up to now, the processes that determine the amount of energy that is stored in the magnetic field and the trigger mechanisms that enable its sudden release is not yet clear;
- *Energetic problem*: a theory that can explain how the converted magnetic energy is distributed among ion heating, electron heating and acceleration of supra-thermal particles is still missing;
- *Scales problem*: magnetic reconnection is inherently a local, microscopic process while the magnetic energy accumulation and plasma evolve on macroscopic scales. Understanding how microscopic and macroscopic scales are related is therefore necessary.

This chapter is aimed to highlight the recent progresses in understanding the magnetic reconnection phenomenon, by presenting the most significant experimental observations and the numerical simulations and by discussing the main meaningful theoretical models, in order to know the key mechanisms and the physical effects.
This chapter is organized as follow: in section 3.2 the equations of magnetohydrodynamics are presented, showing the main differences between the single- and two-fluid approximations. The concepts of ideal plasma and frozen field lines are also introduced. In section 3.3 the main experimental observations of the magnetic reconnection processes are pointed out, including both astrophysical and laboratory experiments. Section 3.4 is devoted to present the main theories and the most recent understanding on magnetic reconnection phenomena. Finally, section 3.5 presents the evolution of tearing mode instability in thermonuclear devices.
A table showing the main physical quantities that are reported throughout this chapter is shown in table 3.1.

3.2 Magnetohydrodynamics

Fusion plasma as well as magnetic reconnection have historically been treated in the framework of the *Magnetohydrodynamics* (MHD).

Quantity	Symbol	Formula
Ion plasma frequency	ω_{pi}	$\left(\frac{4\pi n_i e^2}{m_i}\right)^{\frac{1}{2}}$
Electron plasma frequency	ω_{pe}	$\left(\frac{4\pi n_e e^2}{m_e}\right)^{\frac{1}{2}}$
Ion gyro-frequency	ω_{ci}	$\frac{eB}{m_i c}$
Electron gyro-frequency	ω_{ce}	$\frac{eB}{m_e c}$
Ion skin depth	δ_i	$\frac{eB}{m_i c}$
Electron skin depth	δ_e	$\frac{eB}{m_e c}$
Alfvén speed	v_A	$\frac{B}{\sqrt{\mu m_i n_i}}$
magnetic Reynolds number	Rm	$\frac{\mu L v}{\eta}$
Lundquist number	S	$\frac{\mu L v_A}{\eta}$

Table 3.1: Table of the main used quantities. Formulas are expressed in the MKS system of units.

The MHD model describes the plasma as a one- or two-fluid object under the effect of pressure and electromagnetic forces. The equations of MHD are determined by combining the motion and thermodynamics laws of fluid elements to the Maxwell equations [23]. Several simplifications can be made, under some approximation, in order to obtain a more manageable system of equations.

In the two-fluid MHD model, plasma is consider as composed by an electron fluid and an ion fluid. If we take into account that no particle or momentum sources exists in the system, the mass and momentum equations can be respectively written as [64]:

$$\frac{\partial \rho_\alpha}{\partial t} + \nabla \cdot (\rho_\alpha \mathbf{v}_\alpha) = 0 \tag{3.1}$$

$$\rho_\alpha \left(\frac{\partial \mathbf{v}_\alpha}{\partial t} + \mathbf{v}_\alpha \cdot \nabla \mathbf{v}_\alpha \right) = \sigma_\alpha \mathbf{E} + \mathbf{j} \times \mathbf{B} - \nabla \cdot \mathbf{p}_\alpha + \mathbf{R}_{\alpha\beta} \tag{3.2}$$

where α and β represent the particle species (ions i and electrons e), $\rho_\alpha = m_\alpha n_\alpha$ is the mass density, $\mathbf{v}_\alpha$ is the fluid velocity, $\sigma_\alpha = \pm e n_e$ is the charge density, $\nabla \cdot \mathbf{p}_\alpha$ is the pressure tensor and $\mathbf{R}_{\alpha\beta}$ is the rate at which the species α gain or lose momentum due to collisions with species β. $\mathbf{E}$, $\mathbf{B}$ and $\mathbf{j}$ are

the usual symbols for the electric field, magnetic field and current density, respectively.
This model can be further simplified to a single fluid approach, if the collisionality is high enough to minimize the relative drift velocity distributions of both ions and electrons. This model, simply inferred as MHD model, can be obtained by introducing the following quantities: the mass density $\rho = \rho_i + \rho_e$, the fluid velocity $\mathbf{v} = (\rho_i \mathbf{v_i} + \rho_e \mathbf{v_e})/\rho$ and the charge density $\sigma = e(n_i - ne)$.
The pressure term is often considered as a scalar p, by providing an equation of state for the scalar pressure. Usually an equation $p \sim n^\gamma$ is used, where γ is the ratio of the constant pressure to the constant volume specific heat.
By combining (3.1) and (3.2) and introducing the above mentioned approximations, the following fluid equations can be obtained:

$$\frac{\partial \rho}{\partial t} + \nabla \cdot (\rho \mathbf{v}) = 0 \tag{3.3}$$

$$\rho \left(\frac{\partial \mathbf{v}}{\partial t} + \mathbf{v} \cdot \nabla \mathbf{v} \right) = \sigma \, \mathbf{E} + \mathbf{j} \times \mathbf{B} - \nabla p \tag{3.4}$$

$$\mathbf{E} + \mathbf{v} \times \mathbf{B} = \eta \, \mathbf{j} + \frac{\mathbf{j} \times \mathbf{B}}{n \, e} - \frac{\nabla p_e}{n \, e} \tag{3.5}$$

where η is the scalar plasma resistivity.
Equation (3.5) represents the generalized Ohm's law, whose last two terms take into account the Hall and the diamagnetic effects [64]. Actually, this equation doesn't strictly represents a single-fluid equation due to the presence of the ∇p_e term.
It should be noted also that the term $\mathbf{R}_{\alpha\beta}$ has disappeared in the MHD equations, being the collisionality implicitly included in the resistivity and current density terms.
In some cases, few terms of the MHD equations can be neglected in order to further simplify the expressions. Whether a term can be eliminated is often determined by rough estimates by replacing the differentials with characteristic time and spatial scales [54].

The so-called *resistive MHD* framework is obtained by introducing the following further approximations:

- quasi-neutrality $n_i = n_e$;
- small ion Larmor radius compared to the scale size of the fluid motion.

These conditions allow us neglecting respectively the $\sigma \mathbf{E}$ term in eq. (3.4) and the Hall terms in eq. (3.5).
The whole set of resistive MHD equations can be then written, taking into account also the Maxwell equations, as:

$$\nabla \times \mathbf{E} = -\frac{\partial \mathbf{B}}{\partial t} \qquad (\textit{Faraday's law}) \tag{3.6}$$

$$\nabla \cdot \mathbf{B} = 0 \qquad (\textit{Gauss' law}) \tag{3.7}$$

$$\nabla \times \mathbf{B} = \mu \mathbf{j} \qquad (\textit{Ampere's law}) \tag{3.8}$$

$$\frac{\partial \rho}{\partial t} + \nabla \cdot (\rho \mathbf{v}) = 0 \qquad (\textit{Mass conservation}) \tag{3.9}$$

$$\rho \left(\frac{\partial \mathbf{v}}{\partial t} + \mathbf{v} \cdot \nabla \mathbf{v} \right) = \mathbf{j} \times \mathbf{B} - \nabla p \qquad (\textit{Momentum conservation}) \tag{3.10}$$

$$\mathbf{E} + \mathbf{v} \times \mathbf{B} = \eta \, \mathbf{j} \qquad (\textit{Ohm's law}) \tag{3.11}$$

$$p = k n^{\gamma} \qquad (\textit{equation of state}) \tag{3.12}$$

where μ is the magnetic permeability and k is a proportionality factor. In the Ampere's law the displacement term $\epsilon_0 \frac{\partial \mathbf{E}}{\partial t}$ has been neglected.
By combining Faraday's law (3.6) and Ohm's law (3.11), the equation of magnetic induction is obtained, describing the dynamics of magnetic and

fluid velocity fields:

$$\frac{\partial \mathbf{B}}{\partial t} = \nabla \times (\mathbf{v} \times \mathbf{B}) + \frac{\eta}{\mu}\nabla^2 \mathbf{B} \qquad (\textit{magnetic induction}) \tag{3.13}$$

The two terms on the right-side of eq. (3.13) vary on different temporal scales, respectively given by

$$\tau_C = \frac{L}{v} \qquad (\textit{convective or fluid time scale}) \tag{3.14}$$

$$\tau_D = \frac{\mu L^2}{\eta} \qquad (\textit{diffusive or resistive time scale}) \tag{3.15}$$

where v and L are typical velocity and length scales [15].
The ratio of these temporal scales is dubbed as the *magnetic Reynolds number*:

$$R_m \equiv \frac{\tau_D}{\tau_C} = \frac{v\mu L}{\eta} \tag{3.16}$$

R_m provides an estimation of the dominant temporal scale in the magnetic field evolution [54].
If $\eta = 0$ (or $R_m >> 1$), the plasma is well described by the so-called *ideal MHD*. In this framework, eq. (3.11) and eq. (3.13) become, respectively:

$$\mathbf{E} + \mathbf{v} \times \mathbf{B} = 0 \tag{3.17}$$

$$\frac{\partial \mathbf{B}}{\partial t} = \nabla \times (\mathbf{v} \times \mathbf{B}) \tag{3.18}$$

Thus the dynamics of the magnetic field is determined by the plasma motion. The magnetic field lines are said *frozen-into* the plasma and any topological variation of magnetic field is forbidden. This means also that any plasma on a given field line is bound on that line and cannot move to another line [63].
If $v = v_A$, namely the Alfvén velocity $v_A = B/\sqrt{\mu\rho_i}$, and if L represents the spatial dimension of the system, then the Reynolds number becomes

equivalent to the *Lundquist number* S

$$S = \frac{v_A \mu L}{\eta} \tag{3.19}$$

The Lundquist number is the ratio of the global Ohmic diffusion time τ_D to the global Alfvén time $\tau_A = L/v_A$.
To an excellent approximation, space and laboratory plasmas can be described by ideal MHD. In this context, reconnection concerns to the breakdown of the frozen magnetic flux condition on time scales much shorter than plasma classical diffusion time based on ion-electron collisions [59].
In MHD theory, the processes that are able to convert magnetic energy into other forms are distinguished as ideal and non-ideal, the former being derived on the framework of ideal MHD. Ideal processes, such as the kink instability, can convert magnetic energy into kinetic energy without any magnetic dissipation. Therefore, ideal processes cannot generate heat [54]. However, they can generate waves which can be dissipated by secondary non-ideal processes. On the contrary, non-ideal MHD processes, such as magnetic reconnection, can convert magnetic energy into heat and kinetic energy. Although ideal MHD process can release energy very fast, they don't release significant amount of energy due to the topological constraints that exist without the dissipation term. Magnetic reconnection, in contrast, has not any constraint, hence it can release a much larger amount of energy [54].

3.3 Magnetic Reconnection Observations

The research on magnetic reconnection has been conducted on three main fronts: theory and numerical simulations; solar and space observations, by means of dedicated telescopes and spacecrafts; laboratory experiments.
In this section, the main observations in space and laboratory plasmas are briefly presented, in order to give the reader an idea of the physical phenomena in which magnetic reconnection is involved and the typical times that characterize its dynamics.

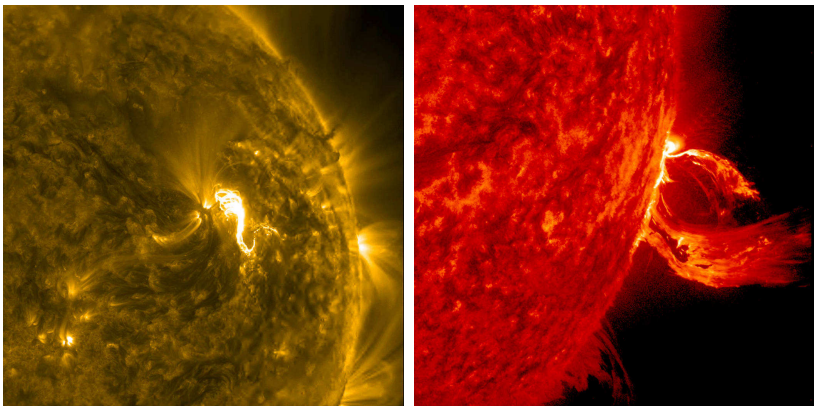

Figure 3.2: Image of solar flares (left) and CME (right) in extreme ultraviolet wavelengths. Taken by [65]. Credit NASA/SDO

3.3.1 Space observations

Many important discoveries on magnetic reconnection have been made thanks to the spatial observations, which make use of telescopes, which provide detailed images of the solar atmosphere, and space satellites, which make *in-situ* measurements of the electromagnetic and particle velocity fields.
In the next paragraphs, the main evidences of magnetic reconnection events in solar and space plasmas are presented.

Solar flares

In the Sun atmosphere, the *Corona*, magnetic field lines form bow-shape structures, named *coronal loops*, whose base points (*footpoints*) lie on the visible surface of the Sun, the so-called *photosphere*. These loops stretch out in the solar corona and are denser in the most active magnetic regions, such as in the sunspots [58]. Magnetic field lines are continuously moved by convective motions that occur under the photosphere. When they get close each other, a current sheet can be formed and, by means of magnetic reconnection, a solar flare can have origin.
Solar flares manifest themselves with a localized, sudden increase of radiative emissions in the whole electromagnetic spectrum. They are also associated with acceleration of a huge amount of particles and, sometimes, with a large scale ejection of mass and magnetic flux (CME) into the interplanetary space

(Fig. 3.2) [54].
The space observatories, from Skylab [66] to the more recent ones, such as SDO [67], RHESSI [68] and SOHO [69], have shown that electrons are accelerated up to tens of keV and ions are accelerated up to tens of MeV, at relativistic energies. Their energy spectra are typically non-thermal with a broken power-law distribution [70, 59]. These results suggest that mechanisms able to efficiently accelerate charged particles to non-thermal energies during magnetic reconnection events must exist. Solar flares can emit up to $10^{25} J$ of energy in less than a hour, even if the observations at the X-ray wavelengths show that most of this energy is released in the initial phase of the flare, in few minutes [57]. The number of accelerated particles, up to 10^{37} electrons per second above 20 keV in less than a second and up to 10^{35} ions per second with energies above 1 MeV [71], is much larger than could be accelerated in a single reconnection region [72].
One of the most accredited theory, able to explain the particle number and also the power-law energy distribution, suggests that a current sheet can be subject, possibly by means of turbulence, to a fragmentation determining, in this way, a multiple system of sites for the particle acceleration [72, 73].

Solar Corona

Magnetic reconnection is also recognized as the most likely candidate as heating mechanism of the solar corona (Fig. 3.3) to more than one million degrees. If this was the case, magnetic reconnection could solve the so-called *coronal heating problem*, that is why the corona's temperature is, rather surprising, three orders of magnitude higher than the photosphere's temperature [74].
The large amount of energy released in large flares has led scientists to believe flares as the main source of coronal heating. However, several calculations, based on the averaged released energy and on flare repetition frequency, have rejected this hypothesis.
An alternative theory suggests that the corona is heated by smaller flares ($10^{16} - 10^{19}$ Joule flares, called *nanoflares*) [75, 76]. According to this model, the coronal heating originates by small-scale current sheets in the coronal

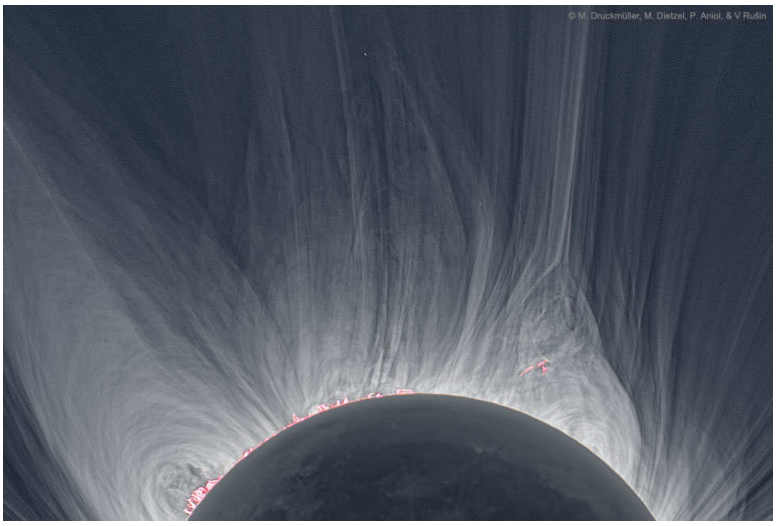

Figure 3.3: Photograph of solar corona during a total solar eclipse [65]. Credit: Druckmüller, Dietzel, Aniol, Rušin

plasma. Unfortunately, the observation of these events is obscured in the noise of the Sun's turbulent atmosphere [77].
Although other alternative solutions to the coronal heating problem, like the so-called *wave heating*, have been proposed [78, 79], reconnection remains the main candidate mechanism, since the magnetic field represents the prevailing energy source in the solar corona [57, 80].

Magnetosphere

The magnetosphere is the space around the Earth in which the geo-magnetic field is dominant over other contributions, such as the interplanetary field and the solar-wind. Because the latter can be consider an ideal plasma, the field lines are deflected around the *magnetopause*, the boundary that separates the geo-magnetic field and terrestrial plasma from the solar wind plasma. In this way, energetic particles cannot enter into the Earth's atmosphere [57].
However, resistive non-ideal regions may exist where current sheets can develop. In these resistive layers, the magnetic reconnection process can join some solar-wind field lines with the terrestrial ones, allowing energetic particles, coming from the Sun, to move into the Earth's atmosphere. This phenomenon leads, especially in periods of intense solar magnetic activity, to

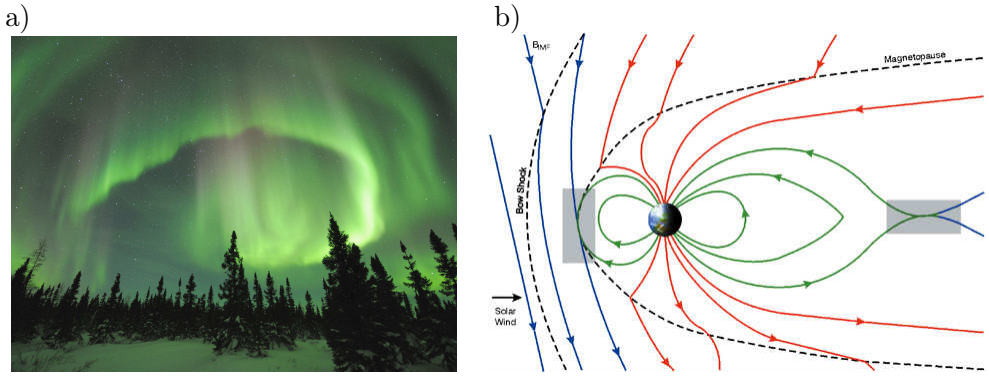

Figure 3.4: a) Photograph of solar aurora borealis. Taken by [81]. b) Schematic view of the interaction between the solar wind and the magnetosphere. The main reconnection sites are represented as gray rectangles. Taken by [82].

Earth's electromagnetic storms or to the fascinating polar aurorae (Fig. 3.4a). The lightning of the aurora is generated by energetic charged particles meeting the neutral ones in the atmosphere; it is visible to the poles where the magnetic field lines are denser.

Over the past decades, several spacecrafts, such as Wind, Cluster and THEMIS, have made detailed *in-situ* measurements, showing that current sheets are formed on both the day-side (*magnetopause*) and night-side (*magnetotail*) of the Earth's magnetosphere, as schematized in Fig. 3.4b.

Experimental measurements as well as numerical simulations have shown fast electron acceleration to several times their thermal energy, by means of magnetic reconnection [83]. Several experimental evidences have convinced the researchers to believe that, in these environments, the reconnection dynamics cannot be described by a conventional steady-state resistive MHD theory. There, magnetic reconnection involves terms in the generalized Ohm's law, such as the Hall term, whose causes decoupling of ions and electrons from the magnetic field at the ion and electron skin depth respectively [84], producing an electron diffusion region inside an ion diffusion region [85]. Evidences for a quadrupolar magnetic field and a bipolar electric field, both signatures of collisionless two-fluid reconnection have been discovered [56, 86]. These results are in agreement with recent experimental data from laboratory experiments.

3.3.2 Laboratory observations

Most of the research activity on magnetic reconnection is performed on laboratory experiments. Fusion devises, including tokamaks and RFPs, have provided, since 60s, excellent examples of processes, such as sawteeth and relaxation events, in which magnetic reconnection represents the key physical mechanism. Furthermore, in the last decades, several dedicated experiments have been built, in order to study the dynamics of the reconnection layer where the conversion of magnetic energy occurs. Compared to the former, the latter allow the examination of the electric and magnetic field pattern in the reconnection process, by means of internal probes.

Sawtooth relaxation

Sawteeth, one of the most peculiar instabilities in tokamak plasmas, represent the typical example of global magnetic reconnection in plasma.
The sawtooth oscillations are observed as periodic events that flatten the electron temperature profile in the minor cross section [57]. The characteristic sawtooth shaping, exhibiting by the time traces of electron temperature and X-ray flux signal for a RFX-mod tokamak discharge, is shown in Fig. 3.5i.
Large sawteeth are harmful in fusion devices because they break down the confinement, even if small sawteeth are useful to remove impurities from the plasma core.
Kadomtsev [87] proposed a model involving the $m = 1, n = 1$ tearing mode to describe the sawtooth crashes. His model follows several steps, here summarized [88]: an electric field is imposed externally to drive the toroidal current in the plasma, which, in turn, heats the plasma by Ohmic dissipation. As long as the electron temperature T_e raises, the plasma resistivity η decreases because of the Spitzer's law ($\eta \propto T_e^{-3/2}$) [7]. This resistivity drop must be accompanied by a plasma current rise, in order to maintain the external electric field, through the Ohm's law $E = \eta j$. As the current increases, the core safety factor $q(0)$ decreases. If $q(0)$ becomes less than one, the plasma results unstable to a helical MHD kink mode. The resulting helical deformed

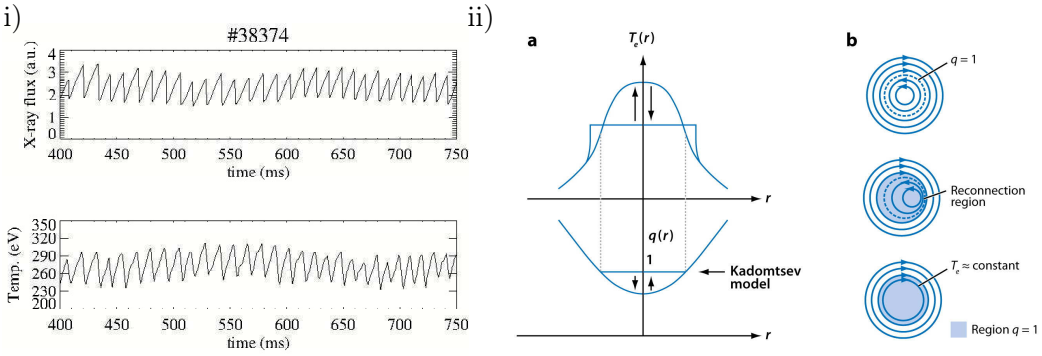

Figure 3.5: i) Time traces of X-ray flux signal and electron temperature showing sawtooth activity in a tokamak RFX-mod discharge. ii) Schematic view of Kadomtsev model of reconnection: a) evolution of temperature and safety factor profiles, b) m=1,n=1 MHD instability developing and triggering reconnection near the $q = 1$ surface. Taken by [59]

plasma drives reconnection near the $q = 1$ surface, as schematically shown in Fig. 3.5ii. The hot plasma in the core mixes with the colder plasma found outer the $q = 1$ surface, resulting in a lower temperature. In this process, both the safety factor and the electron temperature result in a flat profile in the core. The cycle repeats till the external electric field is imposed. According to the Kadomtsev theory, the sawtooth reconnection can be described by the Sweet-Parker model.

Although the Kadomtsev model is very elegant, it is now evident that it doesn't give a complete explanation of the sawtooth instability, even if it is clear that reconnection represents the main involved process.

The experimentally measured q profiles show in fact that the axis safety factor doesn't relax to unity. Beidler and Cassak [89] have suggested a model for incomplete reconnection in sawtooth crashes, where reconnection is switched off when the diamagnetic drift at the reconnection site exceeds a threshold. Moreover, the reconnection rate in sawtooth oscillations is much faster than that predicted by the Sweet-Parker theory. Recent results by numerical simulations have shown that a two-fluid reconnection model can simulate well the observed fast sawtooth reconnection times [90].

RFP relaxation events

In a RFP, the sheared magnetic field changes its pitch from a purely toroidal direction in axis to an almost poloidal direction at the edge, where the toroidal field component is negative. This field line shearing allows magnetic reconnection occurring at multiple radii, at the radial locations where the safety factor q is rational, that is $q = m/n$.

Along with the continuous dynamo action, already described in paragraph 1.8.1, often multiple reconnection events take place simultaneously, leading to a sudden rearrangement of the global magnetic field. These impulsive relaxation events are dubbed as *Discrete Relaxation Events* (DREs). During these events, the generation of magnetic flux from poloidal to toroidal occurs. DREs can be seen as large, rapid variations of the reversal parameter

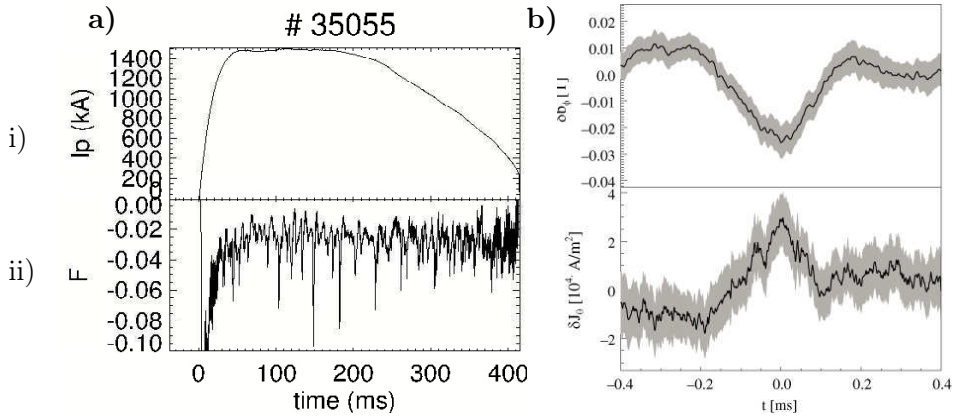

Figure 3.6: a) Time trace of plasma current (i) and F parameter (ii) for a typical RFP discharge in RFX-mod. b) Perturbation of magnetic field (i) and poloidal current component (ii) measured by means of the insertable probe at $r = 0.9a$ [91]

$F = \frac{B_\phi(a)}{<B_\phi>}$, shown in Fig. 3.6a, along with the temporal evolution of the plasma current for a typical high current RFP discharge in RFX-mod.

Zuin et al. [91] have shown that these relaxation crashes are associated with a large energy transfer from the $m = 1$ modes to an $m = 0$ perturbation. These topological changes are also associated with the rapid formation of a strongly localized poloidal current sheet (Fig.3.6b). These results are shown in a more detail in chapter 4.

Controlled reconnection experiments

Although tokamak and RFP devices show several magnetic reconnection processes, the insertion of probes for the measurement of electric and magnetic field profile is impossible in such machines, or, at most, limited to the plasma edge.

In the last decades, several dedicated devices have been built in order to

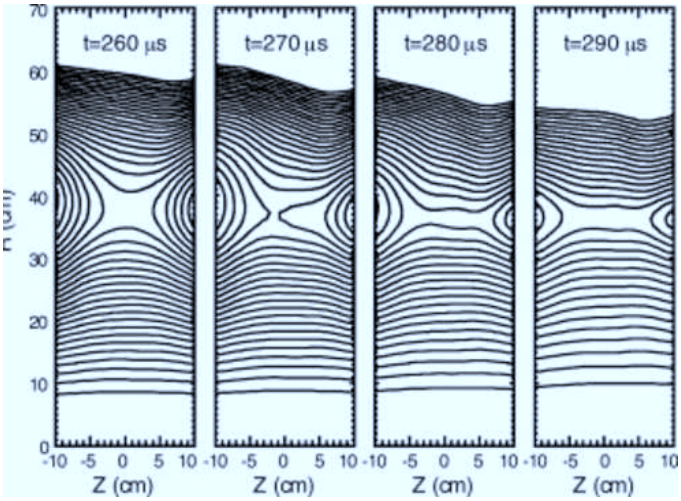

Figure 3.7: Time sequence showing the evolution of magnetic field lines during a magnetic reconnection event in a MRX discharge. Taken by [57]

study the magnetic reconnection phenomenon in controlled reconnection experiments, such as the *Magnetic Reconnection Experiment* (MRX) [92] and the *Versatile Toroidal Facility* (VTF) [93]. In these experiments, two neighbors annular, toroidally symmetric plasmas are created with oppositely directed field lines. A reconnection layer can be then created where both plasma meet. Both collisional and collisionless plasma can be created, by varying the plasma parameters, in a fairly large parameter space range. Magnetic field is measured by means of a large number of magnetic and electric probes [92]. Fig. 3.7 shows the magnetic field lines of the MRX plasma reconstructed from the magnetic measurements, in four times around the magnetic reconnection event.

In these laboratories, evidences of both collisional and collisionless reconnection regimes have been obtained. In particular, researchers at MRX have

confirmed the validity of the Sweet-Parker model at low Lundquist number and a transition to the collisionless regime at slightly higher values. In the latter conditions, a different pattern of ion and electron velocity flow along with a quadrupolar out-of-plane magnetic field, both evidence of two-fluid MHD effects, have been measured (Fig. 3.8) [56].

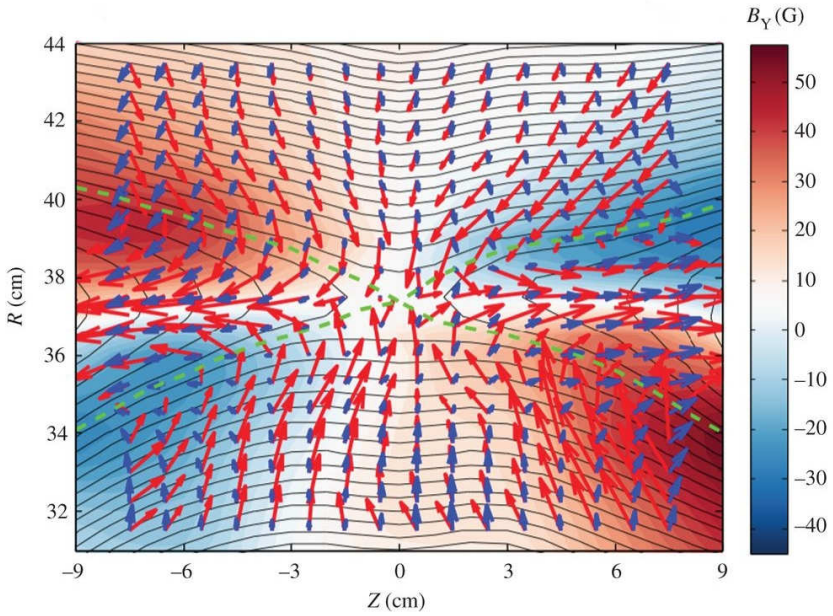

Figure 3.8: Flow vector patterns of ions (blue arrow) and electrons (red arrows) measured during a MRX discharge. The arrow length is proportional to the velocity. The on-plane component of the magnetic field is represented by black lines. The color-coded contour represents the out-of-plane magnetic field magnitude, clearly showing a quadrupolar pattern. Taken by [56]

3.4 Magnetic reconnection models

In this section, the most significant models of the magnetic reconnection are presented, with a particular emphasis on the Sweet-Parker (SP) theory. Although this model cannot explain the 'fast' magnetic energy conversion rate that is observed in many natural physical environments, it still represents the basic pattern for most of the theories that are been presented till now. The SP model is deduced on the basis of simple assumptions, describing its

advantages and limits. Then the most recent progresses in understanding the physics of magnetic reconnection are briefly summarized.

3.4.1 Sweet-Parker theory

Sweet [94] and Parker [95] were the first to formulate a description of the magnetic reconnection phenomenon. Their model is derived, using simple dimensional arguments, in the framework of the resistive MHD. The SP model is an example of *driven reconnection*, because reconnection is guided by an opportune flow of plasma, carrying the magnetic field into the dissipative region [15].

In the SP model, the analytic expressions of magnetic and plasma velocity

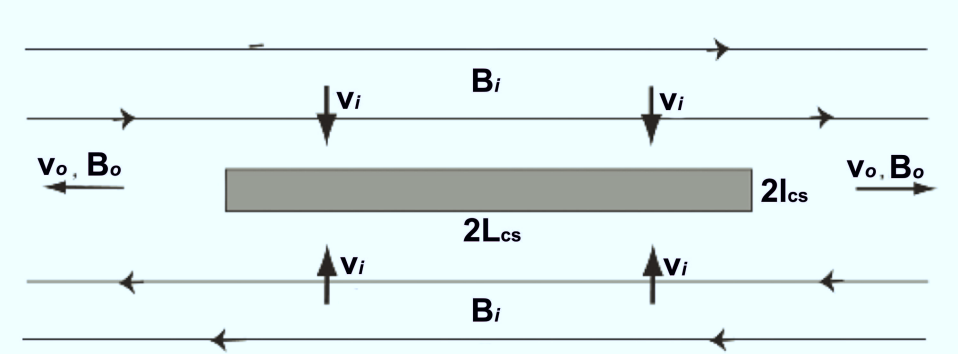

Figure 3.9: Scheme of the Sweet-Parker model. Taken by [15].

fields are not provided. It is supposed a constant electric field **E** to be directed in the z (*out-of-plane*) direction and that the reconnection occurs on a resistive current sheet of length $2L_{cs}$ and thickness $2l_{cs}$, where a current density $\mathbf{J_{cs}}$ flows along [15]. Two oppositely directed magnetic fields $\pm\mathbf{B}$ form a null point at the center of this configuration [56]. The magnetic field has no component in the out-of-plane direction (there is no *guide field*). The system is assumed to be steady-state [15].

The plasma, with mass density $\rho = \rho_i + \rho_e$, is ideal outside the resistive layer, hence the magnetic field lines are frozen-into the plasma. They are carried towards the neutral sheet at speed v_i, as schematized in Fig. 3.9. Just outside the reconnection layer the current density is zero, therefore the

electric field, according to the Ohm's law (3.11), is:

$$E = v_i B_i \tag{3.20}$$

Instead, in the center, where $\mathbf{B} \sim 0$, the electric field can be written as:

$$E = \eta J_{cs} \tag{3.21}$$

where the subscript cs refers to the current sheet, while the subscripts i and o refer to the incoming and outcoming fluxes, respectively.
The current density, according to the Ampere's law (3.8), is

$$J_{cs} \approx \frac{1}{\mu}\frac{B_i}{l_{cs}} \tag{3.22}$$

which, combined with (3.21) and (3.20), yields:

$$v_i = \frac{\eta}{\mu l_{cs}} \tag{3.23}$$

For the mass conservation, the incoming flux $4L_{cs}\rho v_i$ must be equal to the outcoming one $4l_{cs}\rho v_o$, then:

$$Lv_i = lv_o \tag{3.24}$$

where v_o is the velocity of plasma jet going out of the diffusive layer.
For the magnetic flux conservation, there must be $v_i B_i = v_o B_o$, then the outgoing magnetic field is:

$$B_o = \frac{v_i}{v_o}B_i = \frac{l_{cs}}{L_{cs}}B_i \tag{3.25}$$

Assuming the pressure constant everywhere ($\nabla p = 0$), the magnetic Lorentz force, pushing the plasma towards the current sheet, is:

$$J_{cs}B_o \simeq \frac{1}{\mu}\frac{B_i Bo}{l_{cs}} \tag{3.26}$$

From equation (3.10), taking into account that $\partial/\partial t = 0$, due to the steady state condition, one obtains

$$\rho(\mathbf{v} \cdot \nabla \mathbf{v}) = \mathbf{J} \times \mathbf{B} \tag{3.27}$$

from which the following relationship is deduced:

$$\rho \frac{v_o^2}{L_{cs}} \simeq \frac{B_i Bo}{\mu l_{cs}} \tag{3.28}$$

This equation, combined with (3.25), provides the plasma velocity outgoing from the resistive layer:

$$v_o \simeq \frac{B_i}{\sqrt{\mu\rho}} \equiv v_A \tag{3.29}$$

where v_A is the Alfvén velocity relatively to the incoming flux.
This means that, according to the SP model, the plasma enters into the sheet with velocity v_i and goes out at the Alfvén speed.
The dimensionless reconnection rate is defined as:

$$R_i \equiv \frac{v_i}{v_A} \simeq \left(\frac{\eta}{\mu l_{cs} v_A} \right) \tag{3.30}$$

By using equation (3.24), this rate R_i can be written in terms of the Lundquist number S as:

$$R_i \simeq \sqrt{\frac{\eta}{\mu L_{cs} v_A}} = S^{-\frac{1}{2}} \tag{3.31}$$

The reconnection rate provided by the Sweet-Parker theory is then inversely proportional to the square root of the Lundquist number S.
Although the SP model predicts a conversion rate much faster than that expected from resistive decay in absence of current sheets, it is non 'fast' enough to explain the observed reconnection rates. For instance, in a typical coronal plasma, characterized by high S values, the SP model predicts that a solar flare should persist about two months, a much larger value with respect the observed duration typically less than one hour [88].
It should be noted, however, that the SP model remains valid for low Lundquist numbers S ($< 10^4$), collisional plasmas, being confirmed by several numerical

simulations and laboratory measurements [96].
It must be noted that, despite the lack of success to explain the observed reconnection rates in most plasmas, the SP reconnection cannot be referred as 'slow reconnection' as it was done in the past. For $S < 10^4$, the Sweet-Parker rate $R_i \simeq S^{-1/2}$ exceeds 0.01, that is a fast reconnection rate [97].
For larger S values, the resistive sheet should be too thin in order to make the current density dissipating the incoming magnetic flux. Nevertheless, the current sheet width is also the width of the outflow. Therefore, if the mass flux out of the layer is very small, then, for the mass flow conservation, also v_i must be small, hence limiting the reconnection rate.

3.4.2 Petschek model

An alternative 2D, steady-state, reconnection model was proposed in 1964 by Petschek [98]. He realized that the SP reconnection is slow because all the plasma fluid carried out into the reconnection region must flow out trough a thin resistive layer. Petschek therefore suggested that reconnection would be faster if the resistive layer were short and most of the incoming plasma fluid passed in a open outflow region outside the tiny dissipation sheet [97].
In order to deflect the incoming fluid in this wider channel, forces provided

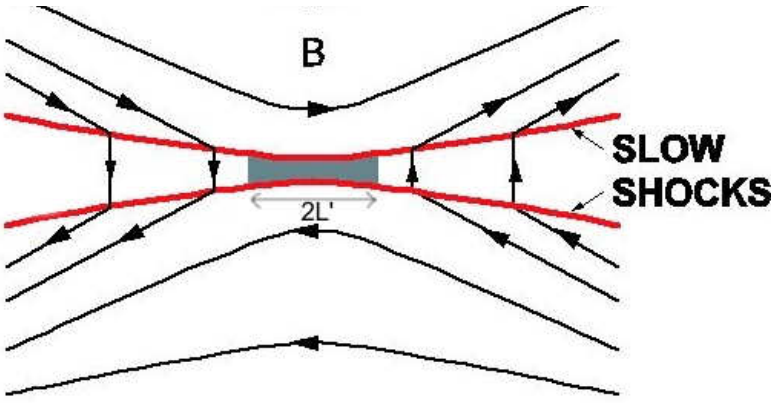

Figure 3.10: Scheme of the Petschek model

by two pairs of steady-state shock waves must exist.
If the current sheet length L_{cs} is replaced by a shorter length L'_{cs}, the reconnection rate enhances by $\sqrt{L_{cs}/L'_{cs}}$.

The Petschek diffusion region is schematized in Fig. 3.10. According to this model, a reconnection rate $R \sim 1/\log S$ can be achieved, a value much faster than the SP one [57].
However, although the Petschek reconnection time agrees with that found in astrophysical and fusion plasmas, this shock wave, steady-state, constant-resistivity configuration has never been found neither in laboratory neither in simulations [56]. According to some simulations, the Petschek model would work only if there were a localized enhancement of the resistivity but this effect has not yet been verified experimentally. Furthermore, the origin of the shock waves is not clear.

3.4.3 Plasmoid instability

In the recent years, researchers have shown that turbulent environments and plasma instabilities can lead to fast reconnection rates. In particular, a theory for fast reconnection suggests that a Sweet-Parker current sheet is tearing unstable if the local Lundquist number S exceeds a threshold $S_c \simeq 10^4$ [59, 97, 99]. In particular, the SP layer can break up into multiple X-lines, separated by magnetic islands. The resulting non-linear structures are called *plasmoids* and the instability is now known as *plasmoid instability* [88].
Furthermore, secondary current sheets are expected to be plasmoid unstable as long as the local Lundquist number exceeds S_c. This gives thus origin to a hierarchical fractal-like structure, which ends down to the scales where the local Lundquist number is less than S_c. At these scales, the resistive diffusion is enough to prevent further dissipation [88, 99]. Each shorter length current sheet, coming out from the original one due to the plasmoid instability, can process a smaller amount of magnetic field lines with respect to a SP larger current sheet, but this can be compensated for by having many of these short resistive layers [57].
The evolution of plasmoids in a reconnection region is far to be linear. Its dynamics follows three main processes: the formation and non-linear evolution of plasmoids by tearing mode, up to a saturation limit; a coalescence phase,

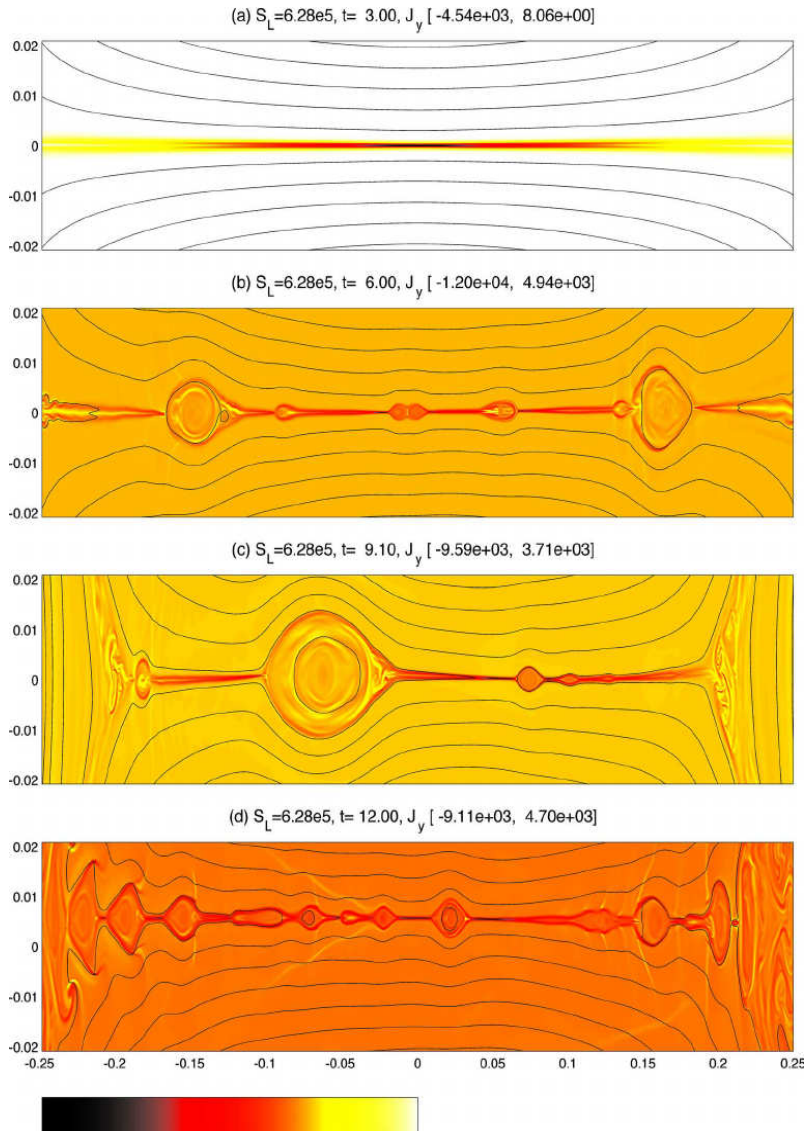

Figure 3.11: Simulation showing the evolution time sequence of a current sheet by plasmoid instability with $S \sim 6 \cdot 10^5$ at times 3,6,9,12 in Alfvén units. Taken by [100]

due to the mutual attraction between neighboring current structures; and the expulsion of the plasmoids along the current sheet by Alfvénic jets [99]. Fig. 3.11 presents a simulation showing the formation and expulsion of plasmoids in a current sheet in a high Lundquist plasma [100].

It has been shown that this non-steady plasmoid mediated reconnection is

fast, the magnetic conversion rate greatly exceeding the Sweet-Parker one for large Lundquist numbers [97]. The formation of plasmoids and the current sheet fragmentation have been observed both in simulations and experimental observations of solar corona [101, 102, 103, 104]. A numerical simulation has shown also the formation of plasmoids in tokamak plasmas during sawtooth crashes [105].

Particle acceleration in fragmented current sheets

It has been observed that electrons and ions in coronal plasmas as well as in magnetotail are accelerated to non-thermal energies during magnetic reconnection events, electrons being able, for instance, to gain up to 50% of magnetic energy in solar flare events [83]. While the plasmoid instability can justify a fast reconnection rate for large Lundquist numbers, through multiple X-lines formation, it says nothing about particle acceleration. However, numerical simulations have confirmed that the particle acceleration by interaction with a multiple current sheet distribution can be faster and more efficient than that with a single 'monolithic' current sheet [106]. A schematic of this multi-step acceleration mechanism is shown in Fig. 3.12a.

In particular, the results of a 3D simulation of a coronal-like plasma performed by Onofri, Isliker and Vlahos are briefly shown [107]. They have studied the evolution of a current sheet with a Harris-like magnetic field [4]. Fig. 3.12b shows the electric field isosurfaces in three different instants ($t = 50\tau_a$, $t = 200\tau_a$, $t = 400\tau_a$). The red surface represents higher values of the electric field, the blue one represents lower values. The sheet evolves by forming small scale structures (current filaments) already at $t = 50\tau_A$. At $t = 200\tau_a$, the sheet is highly fragmented and the electric field is characterized by regions of space where the field is stronger, surrounded by a large volume with a lower electric field. At $t = 400\tau_a$ the sheet is completely destroyed and the electric field becomes highly fragmented. The red regions represent hence a system of multiple acceleration sites for the charged particles.

[4] The Harris sheet is a useful one-dimensional equilibrium model, whose magnetic field profile has the form $B_z(x) = B_0 \tanh(\frac{x}{L})$ [108].

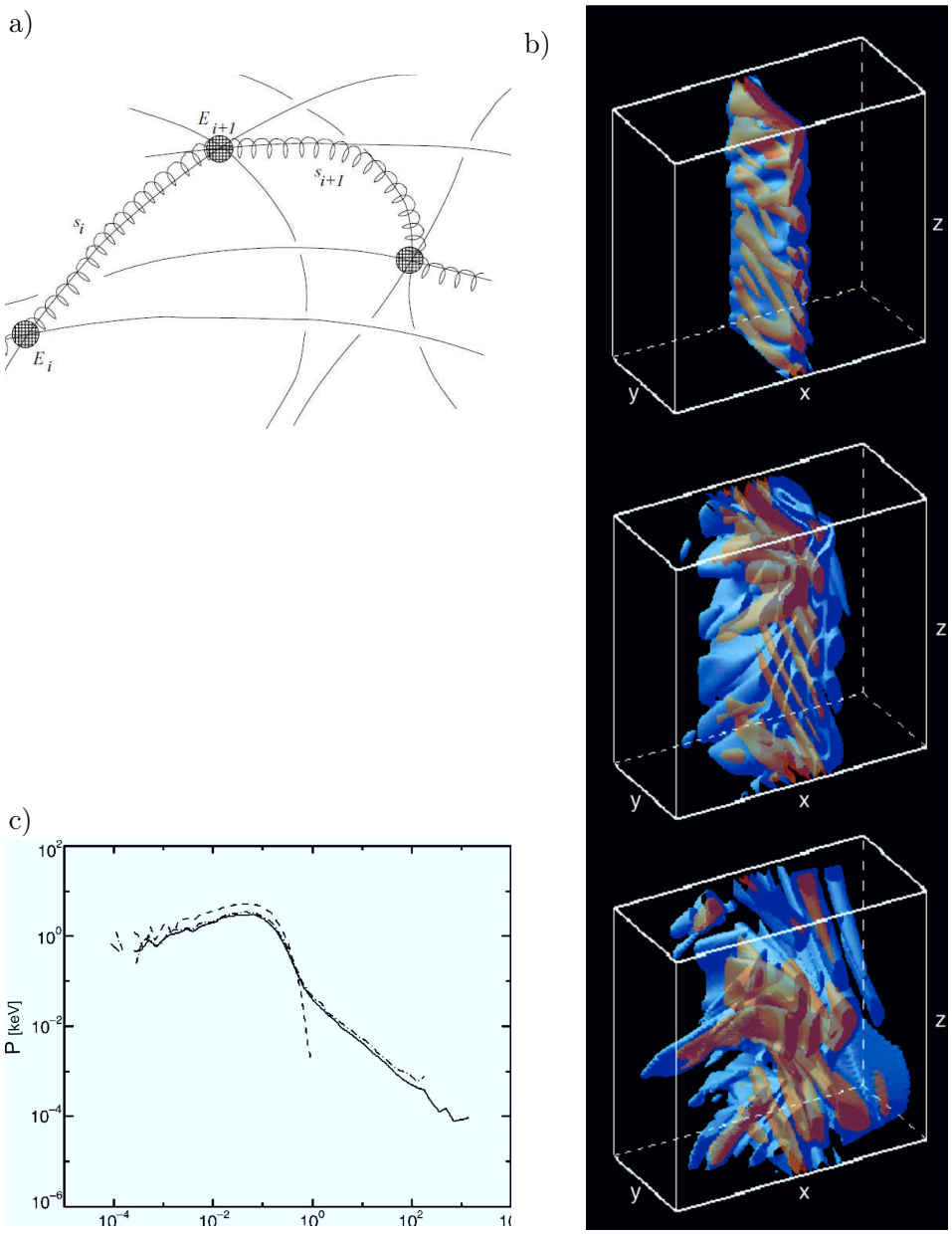

Figure 3.12: a) Schematic of particle acceleration process by multiple current sheet interaction. A particle moves freely along the magnetic field line until it enters a current sheet (filled circles) where it is accelerated by an effective electric field **E**. Taken by [72]; Simulation of coronal plasma dynamics performed by Onofri et al. [107]: b) time sequence of the electric field isosurface at $t = 50\tau_a$, $t = 200\tau_a$, $t = 400\tau_a$, showing the fragmentation process of the current sheet; c) electronic energy distribution at $t = 8 \cdot 10^{-5}s$ (solid line), $t = 3 \cdot 10^{-5}s$ (dot-dashed line) and the initial distribution (dashed line). The last two figures are taken by [107].

Fig. 3.12c shows the energy distribution of a population of electrons, with an initial Maxwellian velocity distribution, injected into the simulation domain. There is a very fast acceleration of electrons, which form a supra-thermal tail up to relativistic energies. The injection of ions, although less efficient, gives an acceleration up to 1Mev.
The result of the simulation shows that a fragmented current sheet can be a very efficient accelerator. Particles can adsorb, in a short time, a large amount of energy from the magnetic field.
In chapter 4, the experimental results suggesting the current sheet fragmentation and particle acceleration during DREs in the RFX-mod plasma are presented.

3.4.4 Collisionless reconnection

The reconnection models here presented can be described in the framework of a single-fluid MHD description. In this context, the collisionality is high, getting the relative drift of ions and electrons small enough to consider both populations as a single fluid. This regime is dubbed as *collisional reconnection*. However, when ions and electrons move differently, the generalized Ohm's law (3.5) should be used, assuming different velocity distributions. In this framework, the two-fluid MHD formulation becomes more appropriate [59].
In thin reconnection layers, such as those observed in magnetosphere plasmas, ions become demagnetized and the relative drift velocity between ions and electrons can be large [57]. In these cases, only electrons are magnetized and two-fluid effects, especially the Hall effect, become important. This regime is dubbed as *collisionless reconnection* because it can be expressed in terms of the collisional mean free path [59]. In particular, the transition between collisional and collisionless reconnection occurs when the current sheet thickness $l_{cs} = L_{cs}/\sqrt{S}$, predicted by the SP model, is equal to

$$l_{cs} = \rho_s \equiv \frac{\sqrt{(T_i + T_e)m_i}}{Q_i B_t} \tag{3.32}$$

where ρ_s is the ion sound gyroradius, T_e and T_i are the electron ad ion temperatures, B_t is the total magnetic field, m_i is the ion mass and Q_i is the ion charge [96].
In the cases in which reconnection takes place without a guide field (this condition is known also as *antiparallel reconnection*), with upstream small plasma beta ($\beta \ll 1$), then ρ_s is equal to the *ion skin depth*:

$$\delta_i = \frac{c}{\omega_{pi}} \tag{3.33}$$

where ω_{pi} is the ion plasma frequency.
In the l_{cs} scale length, ions are demagnetized while electrons are still magnetized. The region where ions are demagnetized is known as *ion diffusion region*. The relation $\mathbf{E} + \mathbf{v_i} \times \mathbf{B} = 0$ is not anymore satisfied for ions, while the motion of electrons can be still described by $\mathbf{E} + \mathbf{v_e} \times \mathbf{B} = 0$, until they reach the region close to the X-point, where they become demagnetized as well. This central region is called *electron diffusion region*.
Fig. 3.13 presents a schematic of the two-fluid reconnection, showing the ion and electron diffusion regions, the magnetic field and particle flow patterns. It can be useful to imagine that, in the ion diffusion region, the magnetic field lines are frozen-in to the electronic fluid, by which they are carried into the X-line to be reconnected.

The evidences of two-fluid effects have been found both in magnetosphere and laboratory plasmas, as already discussed in paragraph 3.3. In particular, the different pattern of ion and electron flows and the quadrupolar out-of-plane magnetic field, the main signatures of two-fluid reconnection, has been found.

3.4.5 Phase diagram

The magnetic reconnection regimes can be represented in a *phase diagram*, which shows the dominant reconnection processes as a function of two dimensionless parameters: the Lundquist number S and a macroscopic length

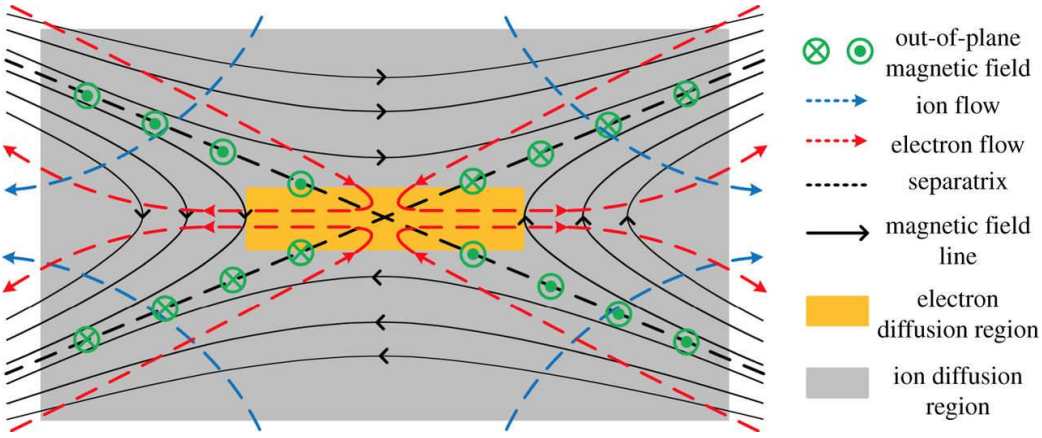

Figure 3.13: Schematic of two-fluid reconnection. The ion and electron diffusion regions are represented, along with the flow patterns. Taken by [56]

λ in units of the ion sound gyroradius [96]

$$\lambda = \frac{L}{\rho_s} \tag{3.34}$$

where L is the plasma size.

The phase diagram has been presented by Ji and Daughton in 2011 [96] and reviewed by Cassak and Drake in 2013 [97]. Fig 3.14 shows the phase diagram, taken by [97]. It presents four main (color coded) regions that are here briefly described, without going deeply into the details.

The white region, labeled as 'no reconnection', suggests that, for $S \lesssim 100$, reconnection doesn't take place. This phase has been added in [97] with respect to the previous version. The authors suggest that, in these conditions, collisionality is high and magnetic diffusion dissipates energy at a fast rate, inhibiting any magnetic reconnection mechanism. The diagram portion labeled as 'Sweet-Parker reconnection' clearly indicates the parameter range at which a single X-point SP layer gives rise to reconnection. The green horizontal line highlights the threshold $S \sim 10^4$ at which a current sheet could be unstable to the plasmoid formation. This SP plasmoid unstable regime is indicated in Fig. 3.14 as a light-salmon portion, labeled as 'Sweet-Parker reconnection with plasmoids'. Finally, the portion of plane above the blue line represents the phase where the two-fluid Hall effects are dominant. The

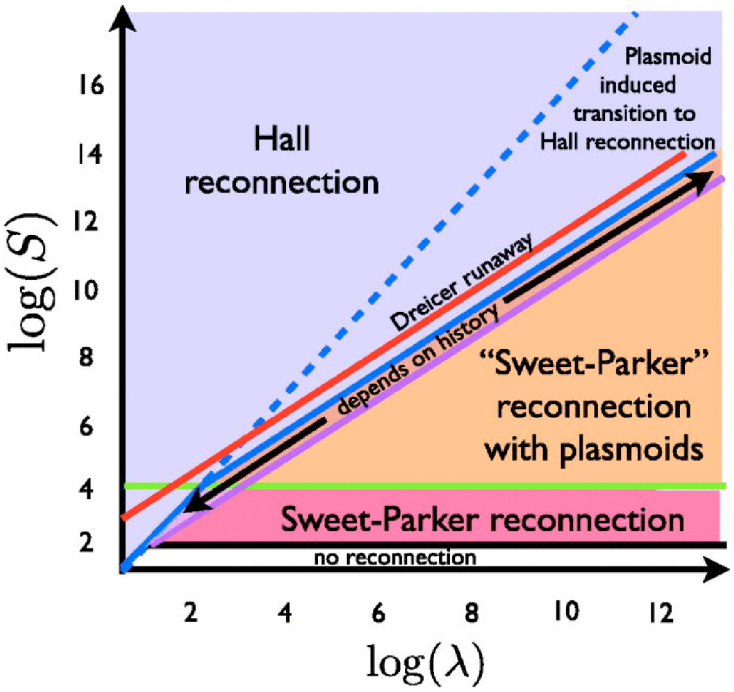

Figure 3.14: Phase diagram of magnetic reconnection. Taken by [97]

solar corona and the magnetosphere plasmas, where strong Hall effects have been detected are located at this stage.

It must be noted that the diagram shows an intermediate region, labeled as 'Plasmoid induced transition to Hall reconnection'. The motivation of this intermediary regime is here explained. As already seen in paragraph 3.4.4, the boundary between collisional and collisionless can be in general addressed by equation (3.32), represented in the graph as a dashed blue line. This may be not true if the current sheet is plasmoid unstable. In fact, secondary current structures can themselves be further subject to the plasmoid instability if $S > S_c$, leading to yet thinner current sheets. If the thickness of the resulting layers approaches the ion sound gyroradius, then collisionless reconnection may be triggered. This means that the plasmoid instability may trigger a transition to fast collisionless reconnection by driving the current sheet thickness below a critical value[56]. Ji and Daughton [96] than suggested that this intermediate region represents a transition phase, in which both collisional and collisionless physics can coexist. Cassak and Drake [97]

suggested instead that, when Hall reconnection takes place, the system remains in this regime for the remainder of the evolution.
The current experiments dedicated to the study of magnetic reconnection, such as MXR and VTF, are placed in a parameter space close to the origin of the phase diagram (that is $\log(\lambda) < 3, log(S) < 4$). It would be interesting to perform high-S experiments, in which non-collisional effects and/or plasmoid instabilities are dominant. In this context, RFP plasmas, characterized by high values of the Lundquist number (up to $S \sim 10^7$) [109], could provide the appropriate conditions for the study of the reconnection processes in such conditions.

3.5 Tearing mode

In the context of magnetic reconnection, an emphasis should be put on tearing mode instability, which is an important subject of this thesis.
The tearing mode (TM) is a resistive instability observed both in tokamaks and RFPs, driven by the radial gradient of the current density [7]. It is accompanied by magnetic reconnection, taking place when the local resistivity is high enough to let the system accessing to a lower energy state, characterized by a change of magnetic line topology.
The resistivity can be destabilizing because it frees the plasma from the constraint that it remains *frozen* to the magnetic field, allowing the growth of plasma perturbations [64].
The name tearing mode derives from the tearing and rejoining of magnetic field lines which occur during the magnetic reconnection process.
In this section, a brief overview of the TM evolution is given, by summarizing the theoretical methods that are commonly used to describe the evolution and stability of the magnetic islands.

3.5.1 Tearing mode analysis

The simplest configuration in which the tearing instability occurs is the so-called *plasma current slab*, already presented in paragraph 3.4.1 to describe

the Sweet-Parker model. In this configuration, magnetic reconnection takes place in a narrow resistive region and the equilibrium field is entirely sustained by a thin current sheet. However, the situation is different in a tokamak plasma, where neither the toroidal nor the poloidal fields change sign along the radius. In this case, the formation of strong magnetic field gradients and current sheets is due to the shear of the magnetic field lines, which generates a situation similar to that described above. At a resonant surface, with $q_s = m/n$, a field line closes into itself after m toroidal and n poloidal turns. Assuming a positive magnetic shear, the neighboring line at $r < r_s$, after m toroidal turns, ends at a lower poloidal angle, while a line at $r > r_s$ ends at a higher poloidal angle. Therefore, an effective helical magnetic field B^* changes sign across the $q = q_s$ surface. Hence, a helical current, with the same helicity of the resonant surface in which it lies, can develop [110].
Plasma resistivity allows the negative field B^* on one side of the $q = q_s$ surface to diffuse into the region of opposite magnetic field on the other side, annihilating it by magnetic reconnection [64]. This annihilation of magnetic field, which is more effective in the vicinity of the resonant surface, is energetically favored, because the magnetic energy $\int \frac{B^{*2}}{2} dV$ results reduced. The resulting lower energy state is characterized by a chain of magnetic islands, centered at the resonant surface.
A magnetic island has helical structure, closing into itself after n poloidal and m toroidal turns. For this reason, the TM instability can be uniquely identified by the couple (m, n). A magnetic island is bounded by the *separatrix*, the two parts of which meet at the *X-points*. The separatrix divides two regions with different magnetic topology. The magnetic field lines within the magnetic island lie on a set of nested helical surfaces, whose magnetic axis is identified by the *O-point*. The maximum radial width, measured through the O-point, is called *island width* W. A schematic representation of a magnetic island is shown in Figure 3.15, in which the axis refers to a helical coordinate system $(r, \xi = \theta - \frac{m}{n}\phi, \phi)$. In this reference system, the O-points, corresponding to the radial position where the perturbed field is minimum, are located at $(r = r_s, \xi = (j + 1/2)\pi)$, while the X-points are placed at $(r = r_s, \xi = j\pi)$, j being an integer.

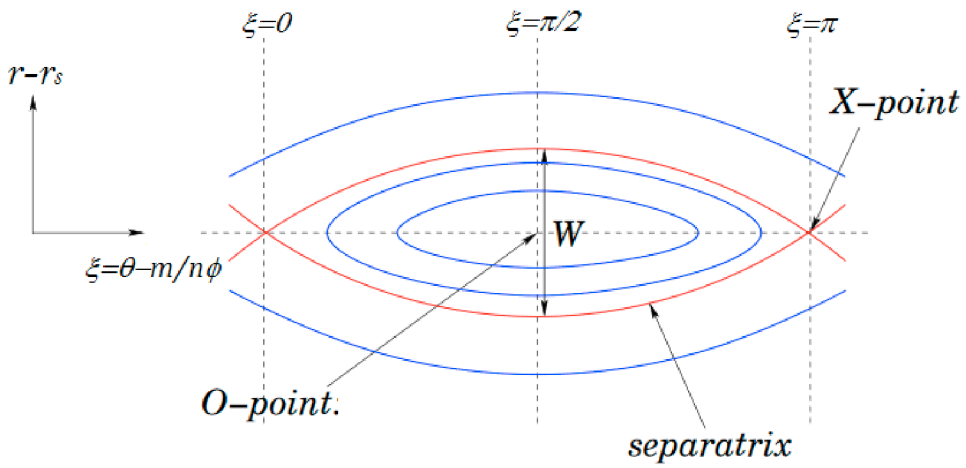

Figure 3.15: Schematic of a magnetic island induced by a TM instability at the resonant surface r_s.

3.5.2 Tearing mode equation

The analysis of TM is typically performed by solving the ideal MHD equations over the most of the plasma, where resistivity is negligible (the so-called *outer region*), and solving non-ideal MHD equations at the resonant surfaces (the *inner* or *resistive region*), where the $\mathbf{v} \times \mathbf{B}$ contribution to Ohm's law (3.11) goes to zero and the $\eta\mathbf{j}$ term becomes important [111, 7]. Thus the theory of TM requires a matching of the two solutions at the edge of the resistive layer and applying the appropriate boundary conditions.
The magnetic field perturbation $\mathbf{b}$ of the magnetic island can be expressed in terms of a magnetic flux function ψ, defined as[7]:

$$b_r = -\frac{1}{r}\frac{\partial \psi}{\partial \theta} \tag{3.35}$$

$$b_\theta = \frac{\partial \psi}{\partial r} \tag{3.36}$$

In the outer ideal region, the plasma inertia is negligible, since the growth of the mode is much slower than an ideal instability (as shown later on), then the equation of momentum conservation (3.10) results in the force balance

equation:

$$\mathbf{j} \times \mathbf{B} = \nabla p \tag{3.37}$$

In the large aspect ratio approximation $R_0/a \gg 1$ (i.e. cylindrical geometry can be taken into account) and taking the perturbations to have the form $e^{i(m\theta - n\phi)}$, equation (3.37), combined with (3.7) and (3.8), can be expressed as:

$$\frac{1}{r}\frac{d}{dr}r\frac{d\psi}{dr} - \frac{m^2}{r^2}\psi - \frac{\frac{dj_\phi(r)}{dr}}{\frac{B_\theta(r)}{\mu_0}\left(1 - \frac{q(r)}{q_s}\right)} = 0 \tag{3.38}$$

This equation is known as the *tearing mode equation* or, under the above described approximations, as the *Newcomb's equation*. The helical perturbation flux ψ is connected to the equilibrium via the poloidal magnetic field $B_\theta(r)$, the safety factor $q(r) = \frac{r}{R_0}\frac{B_\phi}{B_\theta}$ and the toroidal current density profile $dj_\phi(r)/dr$ [112].
Equation (3.38) can be solved piecewise for $r < r_s - \delta$ and for $r > r_s + \delta$ (where r_s is the radial position of the resonant surface and δ is the thickness of the resistive layer) using appropriate boundary conditions. However, the equation cannot be solved at the resonant surface, where $q = q_s$, because of a singularity. In the $[r_s - \delta, r_s + \delta]$ region, the tearing mode stability is treated differently in the linear and non-linear cases [112].

Linear regime

In the linear case, valid for a thin resistive layer ($\delta \to 0$), the perturbation flux ψ doesn't change over the layer and the two solutions can be matched with the condition:

$$\lim_{\delta \to 0} \psi(r_s - \delta) = \lim_{\delta \to 0} \psi(r_s + \delta) \tag{3.39}$$

The growth of the island, in the linear regime, is governed by the so-called *tearing stability index*:

$$\Delta'_0 = \lim_{\delta \to 0} \left[\frac{1}{\psi}\frac{d\psi}{dr}\right]_{r_s - \delta}^{r_s + \delta} \tag{3.40}$$

This parameter is a property of the plasma equilibrium, representing the jump in the logarithmic derivative of ψ to the left and to the right of the layer [64]. If $\Delta'_0 > 0$, determined by the yet unperturbed equilibrium, the current flowing at the resonant surface reinforces the initial perturbation and a tearing mode can grow. On the contrary, if $\Delta'_0 < 0$, the plasma resists tearing [110].
Two different examples, representing a stable and an unstable cases, are presented in Fig. 3.16.

The linear growth rate of the island $\gamma = dW/dt$ is found to be dependent

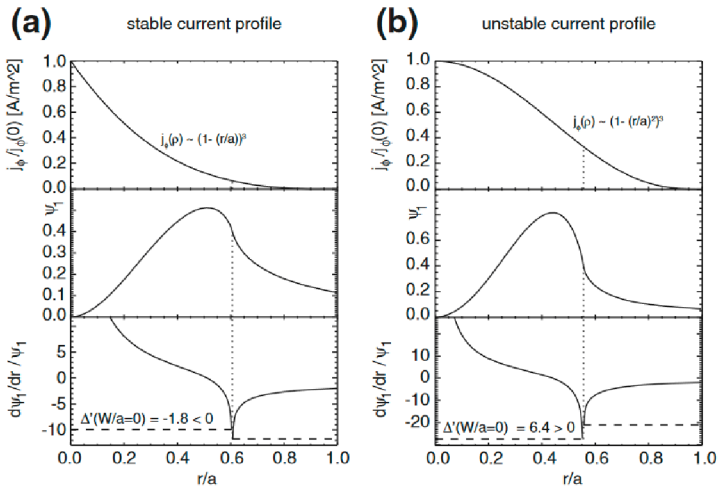

Figure 3.16: Radial profile of several quantities for a stable profile, with $\Delta' < 0$ (a), and an unstable profile, with $\Delta' < 0$ (b), representing, from top to bottom: current density profile, perturbed magnetic flux ψ and logarithm derivative $\frac{\psi'}{\psi}$. These quantities are determined by using the tearing mode equation based on the current profile $j \propto \left(1 - (\frac{r}{a})^2\right)^3$. Taken by [112]

on Δ'_0 parameter and on the characteristic times τ_R and τ_A (resistive and Alfveń time scales, respectively) as [7]:

$$\gamma = \frac{0.55}{\tau_R^{\frac{3}{5}} \tau_A^{\frac{2}{5}}} \left(\frac{a^2}{R_0} \frac{n}{q} \frac{dq}{dr} \right)^{\frac{2}{5}} (a\Delta'_0)^{\frac{4}{5}} \tag{3.41}$$

The TM evolves, in the linear regime, on a time slower than an ideal instability, hence justifying the removal of plasma resistivity in the momentum

conservation equation.

Non-linear regime

The evolution of larger magnetic islands is analyzed in the non-linear regime. The effects of resistivity must be taken into account in a finite region of width W. The solutions in the outer regions are matched, once again, with the solution in the region $[r_s - W/2, r_s + W/2]$, whose size cannot be anymore neglected. In this region, the so-called *constant-ψ approximation* is usually taken into account, that is ψ is assumed to vary weakly within the island. The Δ'_0 stability parameter is replaced by a new term $\Delta'(W)$, depending on the island width of the island:

$$\Delta'(W) = \left[\frac{1}{\psi}\frac{d\psi}{dr}\right]_{r_s-W/2}^{r_s+W/2} \tag{3.42}$$

$\Delta'(W)$ is the jump in the logarithmic derivative of ψ taken across the island. In the constant-ψ approximation, the island width W can be estimated by the mode amplitude at the resonant surface ψ divided by a coefficient related to the equilibrium [113]:

$$W = 4\sqrt{\left|\frac{m\psi}{F_0'(r_s)}\right|}\ , \qquad F_0(r) \equiv mB_\theta - nB_\phi\frac{r}{R_0}\ , \qquad ' \equiv \frac{d}{dr} \tag{3.43}$$

This expression, taking into account (3.35), can be written in the form [7]:

$$W = 4\left(\frac{rb_r q}{mq'B_\theta}\right)^{\frac{1}{2}}\Bigg|_{r_s} \tag{3.44}$$

The evolution of the island is related to the Δ' parameter by the Rutherford equation:

$$\frac{dW}{dt} = \frac{r_s^2\Delta'}{\bar{\tau}_R} \tag{3.45}$$

where $\bar{\tau}_R = 0.82\mu_0 r_s^2/\eta$ is the resistive time scale at the resonant surface, including a numerical factor related to the island geometry.
According to this equation, similarly to the linear case, if $\Delta'(0) > 0$, a tear-

ing mode is unstable and grows, otherwise, if $\Delta'(0) < 0$, the plasma is stable against tearing modes. It is clear that a TM first evolves in the linear regime, then, as soon as the island grows, enters the non-linear regime and the growth rate slows down, until the mode eventually ends up growing on the slow resistive time scale τ_R [111]. The growth of the TM stops when the island width reaches a saturation value W^* which satisfies the condition $\Delta'(W^*) = 0$.
It is important to observe that the saturated island width could be comparable with the whole plasma itself. Therefore, even if the resistive effects occur in a narrow region, the magnetic reconnection processes could be able to significantly modify the entire magnetic configuration of the system [111].

3.5.3 Tearing mode stability

It can be seen from equation (3.44) that the island width is proportional to $b_r^{\frac{1}{2}}$. This means that the growth rate of the island is associated with the growth of the perturbed radial field [7]. The growth of the island is thus limited by the diffusion of this field. For this reason, an important role in the stability of TMs is played by the conductive structures, such as the vacuum vessel, that encircle the plasma. This means that the conductive wall poses a boundary condition for the tearing mode equation and its presence could reduce the value of Δ' with respect to the no-wall condition.
The standard procedure is the following: a solution for $r > r_s$ is launched and integrated to the right boundary of the resonant layer. Likewise, a second solution is launched at $r < r_s$ and these solutions are adjusted until they satisfy the boundary condition at the wall $r = r_w$ and at $r = 0$ ($\psi(0) = 0$).
It can be found that, depending on the current profile, TMs with large values of m are stable because of the m^2 dependence in the first term in the r.h.s. of equation (3.38), which represents the stabilizing effect of the line bending.
In figure 3.17, the values of $r_s\Delta'$ for the $m = 2$ TM are shown, assuming a parabolic current profile, with and without an ideal conducting wall.
Without the wall, the stability parameter Δ' is positive for all positions of the resonant surface. Instead, a perfectly conductive wall reduces this value for resonant surfaces close to the wall.

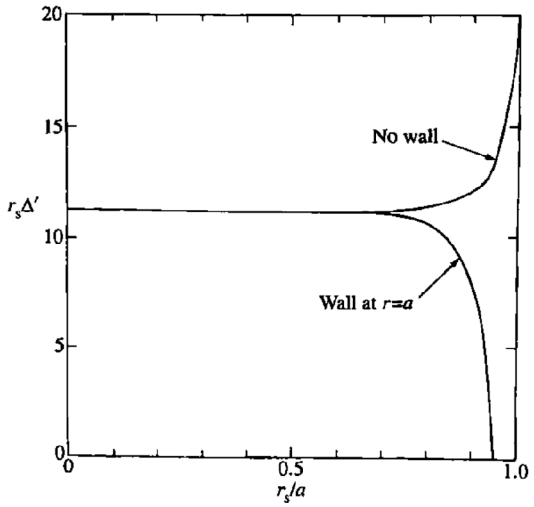

Figure 3.17: Plot of $r_s\Delta'$ for a (2,1) mode for a parabolic current density. The lower plot shows the stabilizing effect of an ideal conductive wall. Taken by [7]

However, a perfectly conductive shell doesn't exist, therefore a real shell could allow the penetration of the radial magnetic perturbation, even if it is close to the plasma. It can be found that field penetration is characterized by a time:

$$\tau_w \simeq \frac{\mu_0 r_w \delta_w}{\eta_w} \tag{3.46}$$

where r_w is the radial position of the shell, δ_w is its thickness and η_w the resistivity [7]. For $t > \tau_w$, the radial field penetrates the shell causing the growth of the TM, with the consequent increase of the radial transport, the reduction of magnetic confinement and, in some cases, to the abrupt termination of the discharge via a disruption. For this reason, the earliest tokamaks had a thick conductive shell, whose penetration time was much longer than the typical pulse duration of the discharge [111].
Fortunately, the natural rotation of TMs can positively affect the influence of the external conducting walls. In fact, the penetration of the radial perturbations into the shell is a strong function of the frequency. At high rotation frequency, the resistive shell has the same behavior as a perfect conductor [7]. Therefore, the rotation of the unstable TM is important to prevent the growth of magnetic islands and the reduction of magnetic confinement.

The analysis of the mechanisms that drive the rotation of TM in the RFX-mod tokamak discharges is one topic of this thesis. Chapter 5 discusses the connection between TM frequencies and flow velocities, estimated by spectroscopic and kinetic measurements. In particular, the dominant contribution of the diamagnetic drift to the TM frequency is shown.

Chapter 4

Analysis of relaxation events in RFP discharges

The Reversed Field Pinch configuration is characterized, as mentioned in chapter 1, by a safety factor less than 1 over all the plasma radius, inverting sign at the reversal surface. Such a q profile leads to the formation of several resistive modes, resonant at multiple radii.
In RFX-mod, the main resonant modes are characterized by poloidal mode numbers $m = 0, 1$ and toroidal numbers $n \gtrsim 3R/2a$. Although such modes can cause field stochasticity through magnetic island overlapping, they are important for the configuration sustainment, by producing the dynamo electric field. Along with the configuration in which such a dynamo is produced by the activity of many tearing modes (the multiple helicity MH), it has been shown that, in high current discharges, the RFP configuration is sustained mainly by a single mode, dominating the spectrum over the other secondary modes (quasi single helicity QSH). This situation is shown in Figure 4.1, in which the spectrum of the $m = 1$ modes as a function of the toroidal number n, during a QSH (black) and MH (red) phases is shown. As can be seen, whereas in MH the resonant modes have comparable amplitudes, in the QSH state, the $m = 1, n = 7$ TM is dominant over all the other components.
RFP discharges exhibit frequent discrete quasi-cyclic relaxation events, most of which are associated to transitions from the QSH to the MH state. During

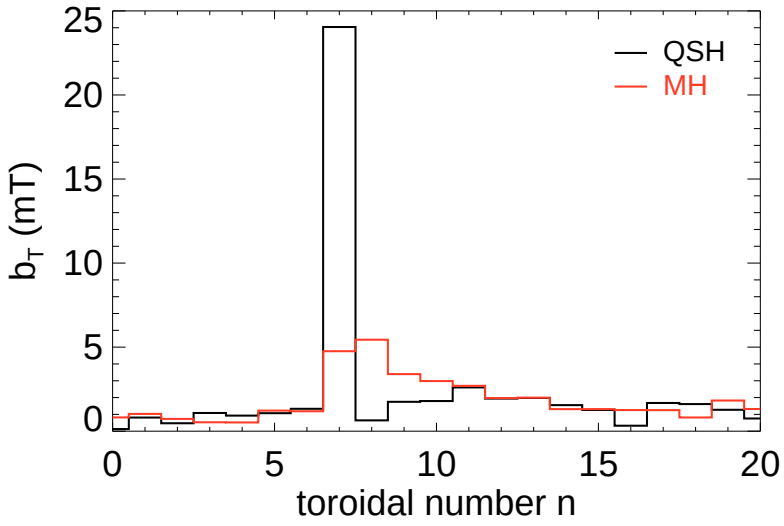

Figure 4.1: Spectrum of $m = 1$ modes as a function of the toroidal number n during a QSH (black) and a MH (red) state, for a typical high current RFP discharge in RFX-mod.

these events, a rearrangement of the magnetic field topology occurs, through magnetic reconnection [91].

Two examples of this characteristic behavior are given in Figure 4.2 , showing the temporal evolution of plasma current I_p and the reversal parameter $F = \frac{B_\phi(A)}{<B_\phi>}$, for two RFX-mod discharges. As can be seen, the F parameter exhibits large fluctuations at several scales, the largest of which are the sign of a global relaxation of the magnetic field.

It must be noted that the frequency of such events is a function of the plasma current, which determines the Lundquist number. The more resistive the plasma, the more frequent the relaxations.

At lower current (Fig. 4.2a), a large number of frequent crashes can be observed; at higher current (Fig. 4.2b), the relaxation events are less frequent but deeper. The former discharge is characterized by a lower value of the F parameter, indicating a deeper reversal of the toroidal magnetic field at the edge. This condition is known as *deep F*. The latter is characterized by a so-called *shallow F*, indicating that the reversal parameter is closer to zero.

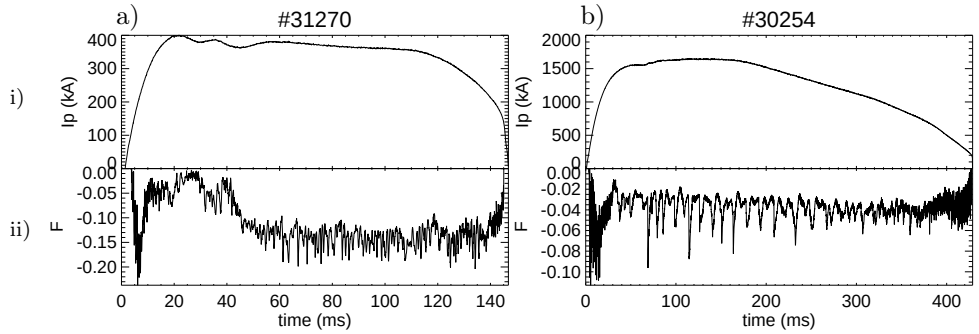

Figure 4.2: Time traces of plasma current I_p (i) and reversal parameter F (ii) for a low (a) and high (b) plasma current discharges.

In this chapter, the analysis of these intermittent events and their effects on the electromagnetic and kinetic fields are presented. In particular, the evolution of the current sheets, developing during the discrete relaxation events, and the characterization of the local acceleration and heating of plasma particles are shown.

4.1 Magnetic analysis

The data analysis presented in this paragraph refers to the toroidal magnetic field measurements collected by the two toroidal arrays of the ISIS pick-up coils. The even and odd poloidal components of the magnetic signals (mainly corresponding to the $m = 1$ and $m = 0$ mode numbers) have been thus easily determined, respectively, as the half-sum and the half-difference of the signals in diametrically opposite positions.

The relaxations events are associated with the rapid formation of localized magnetic perturbations, characterized by a main $m = 0$ periodicity, resonant on the reversal surface, where the condition $q = 0$ is satisfied.

A detail of what happen is shown in Figure 4.3 , which exhibits the amplitude of the $m = 0$ magnetic component as a function of time and toroidal angle, during a single relaxation event. As can be seen, the main perturbation develops in a narrow toroidal position, about 50° wide. It has been demonstrated, by means of insertable current probes at the plasma edge, that this perturbation corresponds to the formation of a poloidal current sheet, with

a maximum radial width of a few centimeter, associated with spontaneous magnetic reconnection [91].

This $m = 0$ activity is always observed to start at the position ϕ_{lock}, corre-

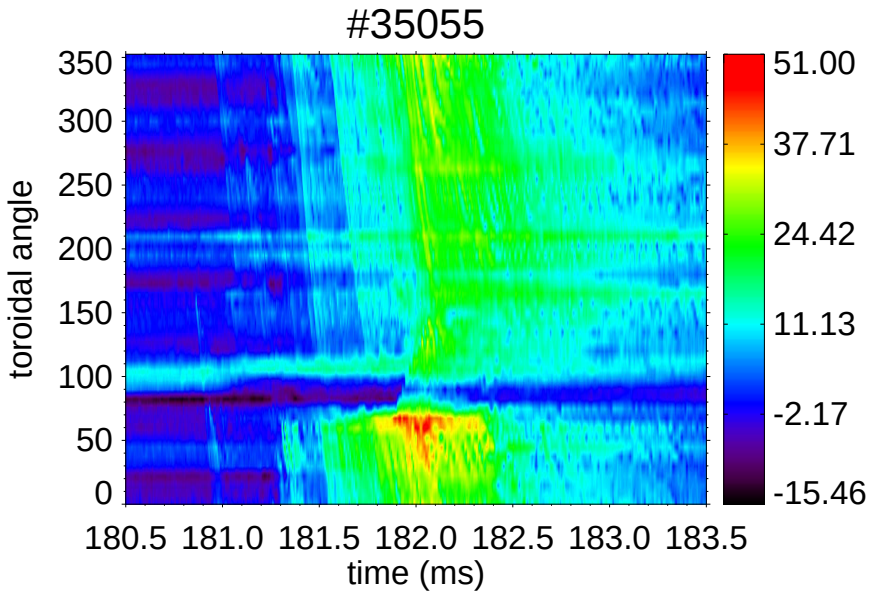

Figure 4.3: Color-coded contour plot of $m = 0$ component of magnetic toroidal signals on toroidal array during a relaxation event. A localized perturbation appears, when magnetic reconnection takes place, at position $\phi \sim 70°$, then propagating towards decreasing toroidal angles.

sponding to the position where several $m = 1$ modes lock in phase, because of a non-linear coupling process, generating a localized deformation of plasma, as schematized in Figure 4.4. After its formation, the current sheet moves with plasma in the direction opposite to the toroidal current, that is towards decreasing toroidal angles.

The development of this $m = 0$ perturbation is associated with the amplitude decrease of the main $m = 1$ tearing mode, which transfers energy to the secondary modes, as can be deduced from Figure 4.5, showing the contourplot of the $m = 1$ (i) and $m = 0$ (ii) component of the magnetic ISIS signals, and the F parameter (iii), during one of such events. Before the crash, a clear $m = 1$ pattern can be identified, characterized by 7 alternating maxima and minima along the whole toroidal angle, while the $m = 0$ is almost negligible. When the crash occurs, the $m = 1$ amplitude decreases, whereas

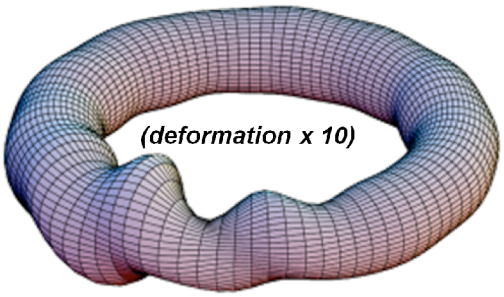

Figure 4.4: Schematic of the plasma column deformation due to the locking of many $m = 1$ modes (the induced deformation is amplified in this schematic for a better view).

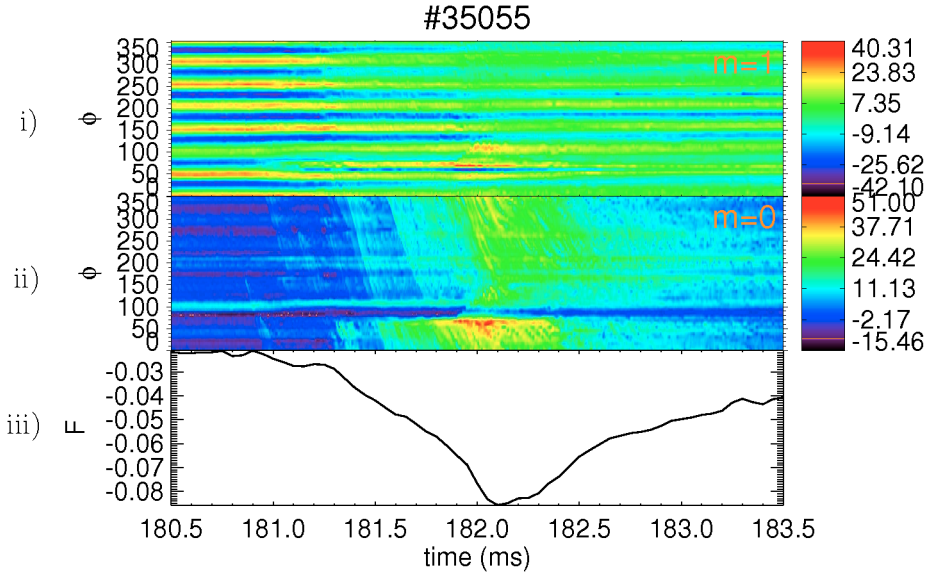

Figure 4.5: From top to bottom: Contour plot of $m = 1$ (i) and $m = 0$ (ii) component of the magnetic toroidal signals, time trace of the F parameter (iii).

a clear $m = 0$ localized structure appears at position $\phi \sim 70°$. This $m = 0$ perturbation then rotates for about one toroidal turn, gradually reducing its amplitude until it disappears.

Figure 4.6 shows the spectra of the $m = 1$ and $m = 0$ harmonics during the same crash time. It can be seen how the $(1, 7)$ mode, dominating at the beginning the spectrum, decreases during the crash as long as the secondary ones increase. An energy transfer to the $m = 0$ modes occurs, whose ampli-

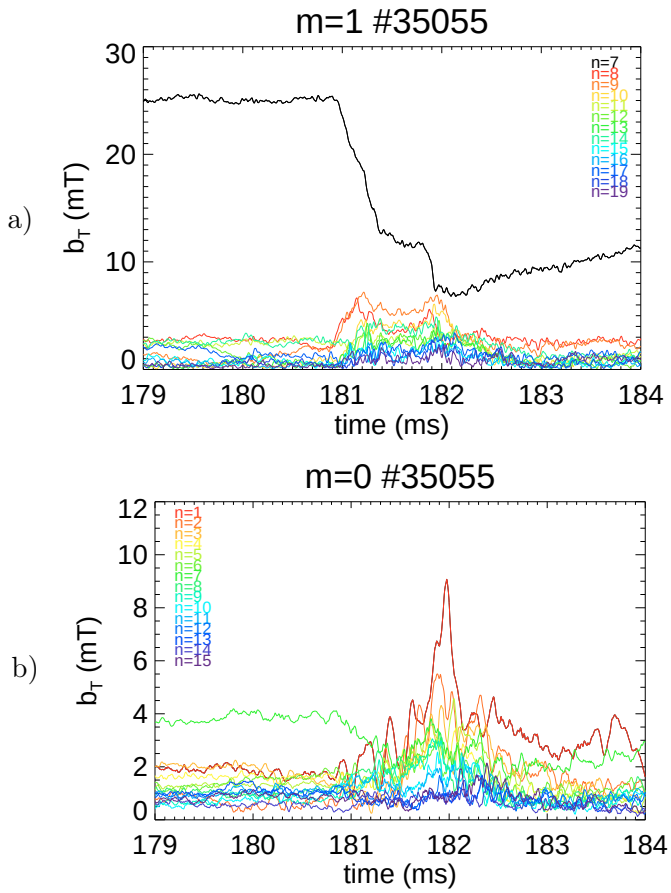

Figure 4.6: Time evolution of the $m = 1$ (a) and $m = 0$ harmonics in a 6ms time window around a relaxation crash. Before the crash, the $(1, 7)$ mode is dominant over all the other secondary ones, during the crash it decreases while the secondary modes increase.

tude increases at the relaxation time.

It must be noted that the (0,7) mode in Fig. 4.6b has a different behavior with respect to the other $m = 0$ modes. It is greater than the others before the crash, while it decreases after the relaxation. This is due to the toroidal coupling with the (1,7) one, so reflecting the time behavior of the latter.

Identification of the reconnection time

The statistical analysis of the experimental data, described in the following paragraphs, has required the identification of the time in which the magnetic

reconnection takes place. Considering that it is not possible to determine the beginning of this process, because of the lack of local measurements, hence such a instant, denoted as t_{rec}, is identified, for simplicity, as the time in which the parameter F reaches the minimum value (Fig. 4.7), during the crashes identified by the wavelet method described in the paragraph 2.2.2.

Nevertheless, it could happen that the process of magnetic reconnection

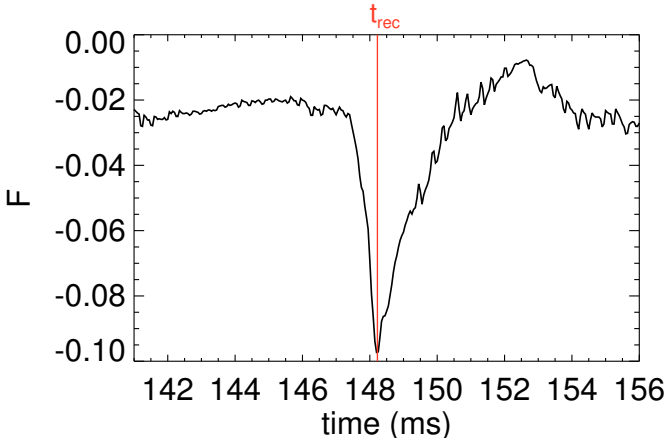

Figure 4.7: Identification of the reconnection time, during a crash of the F parameter.

takes place at a time $t_{mr} = t_{rec} - \Delta t_{mr}$, preceding the identified instant t_{rec}. This behavior can be deduced looking at fig. 4.5, in which the appearance of the $m = 0$ structure occurs a little before the parameter F reaches its minimum value. However, this discrepancy Δt_{mr} ($\sim 10^{-1} ms$) is small compared to the time intervals ($\sim 3ms$) taken into account for the analysis of experimental data. Thus it is believed that the recognized time t_{rec} is a good estimation for the identification of the time in which the magnetic reconnection takes place.

4.1.1 Current sheet fragmentation

In this section, a statistical analysis of the current sheet evolution, by means of magnetic analysis, is presented. The characterization of such perturbations has been performed by studying the intermittent structures that characterize

the magnetic field signals. The wavelet based method for the intermittency detection, illustrated in section 2.2.2, has been used. For each recognized intermittent structure, the amplitude is evaluated as the variation of the signal itself in a time interval equal to the s scale factor, as schematized in Fig. 4.8.
The analysis has been performed taking into account 150 plasma discharges,

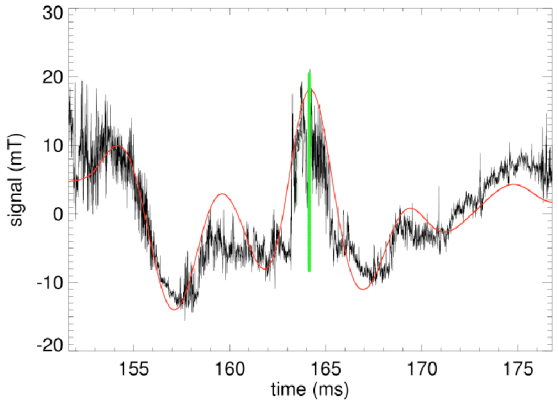

Figure 4.8: Detection of an intermittent event (green segment) in the $m = 0$ component of the magnetic field (black line). The amplitude of a such event is taken equal to the excursion of the signal in a interval equal to the wavelet scale s (green vertical segment). The reversed wavelet transform, determined by few wavelet coefficients is superimposed (red line).

characterized by plasma current in the range $1.4 < Ip_{max}(MA) < 1.7$, in order to include discharges as comparable as possible. The considered identified events belong to the flat-top phase of the plasma current in order to avoid transient phenomena. The database includes into account hydrogen, deuterium and helium plasma discharges.
The statistical analysis of current sheets has been done using the following approach: 1) first, magnetic reconnection events, corresponding to large F parameter crashes, are identified with the wavelet method; 2) for each event, all the intermittent structures of the $m = 0$ magnetic field component are recognized, with the same technique, on a time interval of 3 ms centered on t_{rec}; 3) the toroidal angle (probe location) associated to the current-sheet formation, that is where the field perturbation is maximum, is identified. Such angle Φ_{max} is considered as the origin ($\Phi' = 0$) of a new reference system,

as represented in Fig. 4.9; 4) this process is repeated for each reconnection

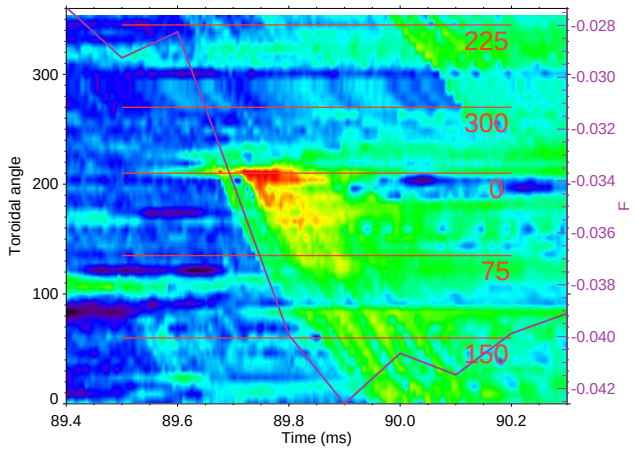

Figure 4.9: Contour plot of the m=0 magnetic field. F parameter is superimposed. Horizontal lines represent the new adopted reference system.

event and for all the discharges; 5) for each new angle (of a such a new reference system), a distribution function is determined just evaluating the total number of events as a function of their amplitude.
It is interesting to observe that, for each scale, the largest number of events is found for an amplitude which increases with the scale itself. This basically means that greater amplitudes correspond to greater scales and vice versa. This can be seen in the contour represented in Fig. 4.10, which shows the number of recognized structures as a function of wavelet scale and amplitude, taking into account a certain reference angle Φ'.

The result of the analysis is then shown in Fig. 4.11: the red curve corresponds to the number of structures revealed at the toroidal position where the major event occurs; the other colors towards blue correspond to increasing angles, according to the legend on the top. It is possible to note that at the greatest amplitudes (>20 mT), which correspond to the largest scales, the number of events decreases when Φ' increases. This tendency is inverted in correspondence of the lowest amplitudes ($< 10mT$) which are related to the shortest scales. This feature suggests that the current sheet structures are subject to a fragmentation process and there is an energy transfer from the largest to the smallest scales.

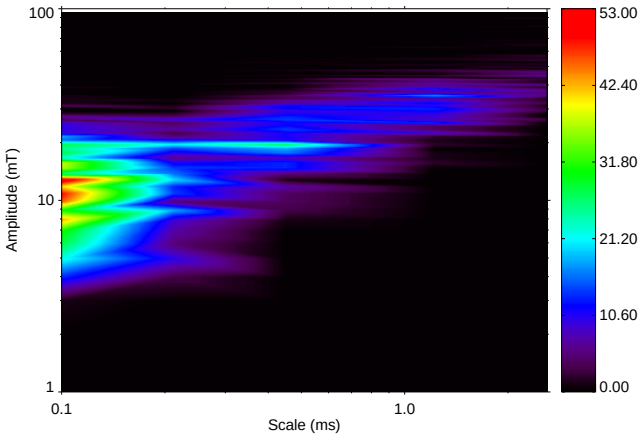

Figure 4.10: Contour plot showing the number of recognized events as a function of scale (abscissa) and amplitude (ordinate) with respect to a fixed angle Φ'.

This result seems to be qualitatively consistent with the numerical simulation of coronal plasma current-sheets made by Onofri et al. [107], already described in paragraph 3.4.3. According to their simulation, the current-sheet fragmentation process is fast and employs about $400\tau_A$ to be complete. An estimation of an analogue temporal interval has been done by considering the Alfvén time relative to the RFX-mod plasma and comparing it with the average time characterizing the current sheet layers experimentally observed ($\tau_f \simeq 4 \cdot 10^{-4} s$) (Figure 4.9). Considering the average value of the Alfvén velocity $v_A \simeq 1 \cdot 10^6 m s^{-1}$ (a typical value for the RFX-mod plasma) and the minor radius $a \simeq 0.5m$ as typical length, the following time is obtained:

$$\tau_A = \frac{a}{v_A} = \frac{0.5m}{1 \cdot 10^6 m\, s^{-1}} \simeq 5 \cdot 10^{-7} s \tag{4.1}$$

Therefore an interval of $400\tau_A$ corresponds to $2 \cdot 10^{-4} s$, a value that matches, as order of magnitude, the experimental one.
It must be noted that, such a current sheet fragmentation could perhaps be compatible with the development of the plasmoid instability along the current sheet. Indeed, the RFP devices, such as RFX-mod, can achieve high Lundquist plasmas (up to $\sim 10^7$), values that are compatible, according to the reconnection phase diagram presented at paragraph 3.4.5, with the

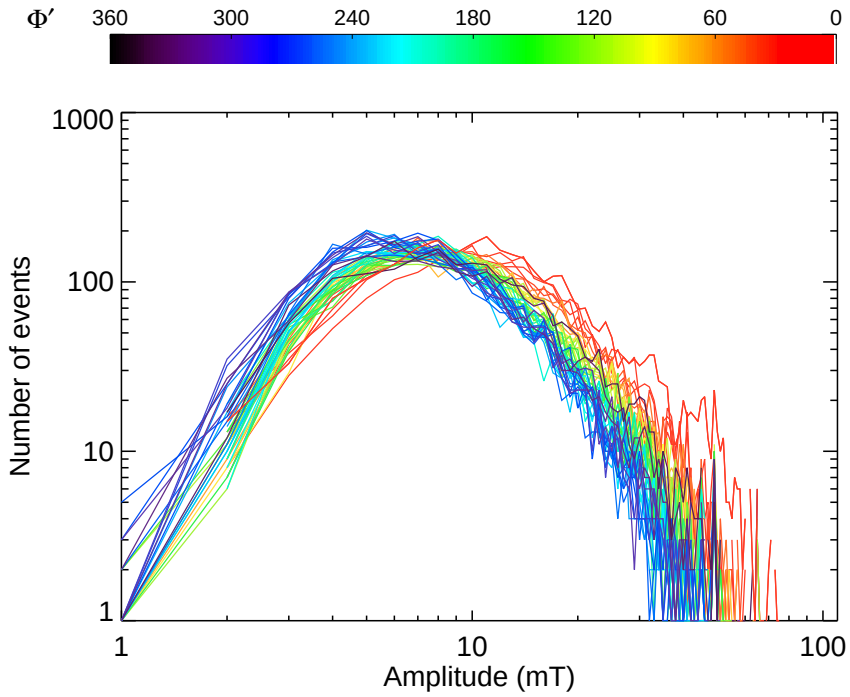

Figure 4.11: Intermittency distribution of m=0 magnetic field component as a function of amplitude. The color bar on the top shows the color-angle correspondence: the red curve refers to the angle $\Phi' = 0$ where the major perturbation occurs. At the greatest amplitudes (>20 mT), the number of events decreases when Φ' increases. On the contrary, at the lowest amplitudes ($< 10mT$) the number of intermittent structures increases with Φ'. This suggests the fragmentation of the current sheet, formed after magnetic reconnection.

development of such an instability. Further analysis is needed in order to verify this hypothesis.

4.2 Particle dynamics

The current fragmentation, just discussed, is also in agreement with what predicted in the literature, which highlights two important aspects: a current sheet could be naturally subject to fragmentation [107] and a fragmented current sheet represents a more efficient particle accelerator with respect to a monolithic one, by offering multiple particle acceleration sites [72].
Indeed, bursty generation of D-D fusion neutrons and gamma rays are ob-

served, which appear to be time correlated with the reconnection dynamics, as can be seen in Fig. 4.12, which shows the time evolution of the edge toroidal field and the count of gamma rays and neutrons. The production of

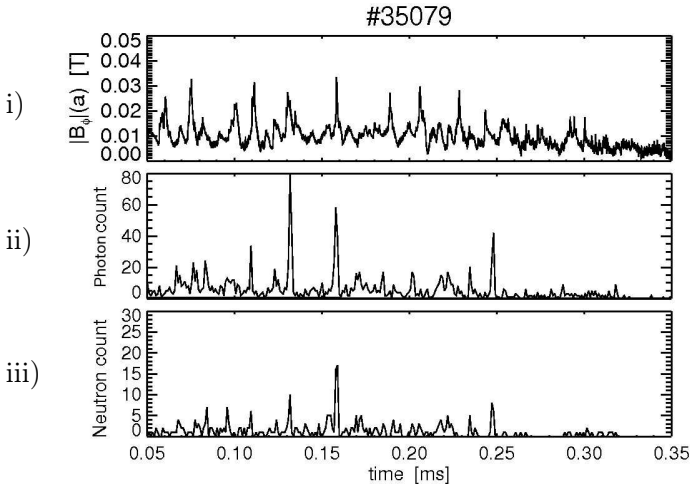

Figure 4.12: Time evolution of toroidal edge magnetic field perturbation (i), gamma photon count (ii) and neutron count (iii).

neutron is strictly related with the heating and accelerations of ions, instead the gamma production could means that, along with ion heating, also an electron heating could take place in the reconnection process, or that neutron capture reactions[1] are occurring from the wall materials encircling the RFX-mod plasma [114].

The correspondence among the signal spikes seems to suggest the coupling among particle acceleration and magnetic reconnection phenomena.

It should however be noted that, although there is a clear correspondence between the most intense peaks of the neutron and gamma fluxes and that of the magnetic signals, there is no a strict one-to-one correspondence. This is because acceleration and heating due to the reconnection process are local phenomena, and therefore, the detected fluxes of neutrons and gamma rays are larger when the main $m = 0$ magnetic fluctuation develops in the vicinity of the neutron detector.

[1]Neutron capture is a type of nuclear reaction in which an atomic nucleus collides with one or more neutrons, merging to form a heavier nucleus. The resulting nucleus typically does form in an excited state and decays by emitting one or more gamma photons.

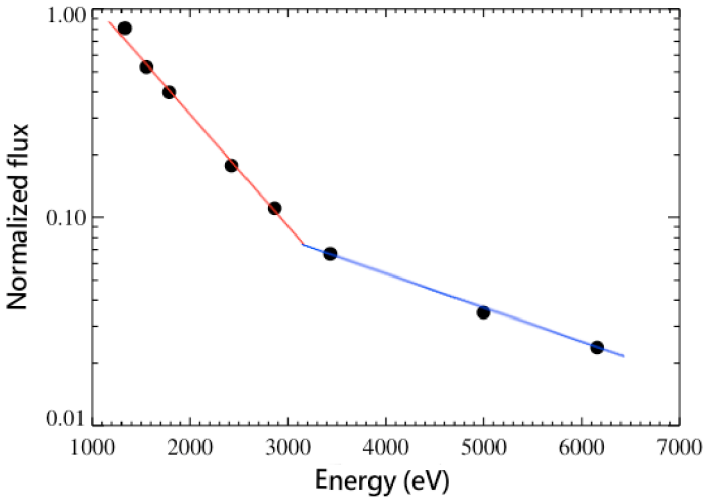

Figure 4.13: Example of distribution of the neutral particle fluxes. Two different distributions, interpolated by straight lines, can be easily recognized.

This local behavior can be deduced also from the analysis of Neutral Particle Analyzer, measuring the distribution function of the neutral atoms produced by charge-exchange reactions in the plasma. The NPA diagnostic is placed at the toroidal position $\phi_{NPA} = 277°$ and it has a narrow solid angle of view, therefore revealing only neutrals coming from the proximity of that position. The RFP particle population has a typical energy distribution characterized by a thermal (Maxwellian) component plus a high-energy non-thermal tail. Each component of the particle distribution can be interpolated with a law $\Gamma(E) = \Gamma_0 e^{-\frac{E}{T}+\gamma}$, as shown in Figure 4.13, in order to deduce the temperature T_i in the thermal region and the temperature T_i^* in the non-thermal tail. Actually the latter is not strictly a temperature, since the high temperature tail does not describe a Maxwellian distribution.

From the flux analysis, it has been found that magnetic reconnection heats the plasma and that this process acts locally. The contour-plot in Figure 4.14 shows the temperature T_i as a function of the time relative to the reconnection $t - t_{rec}$ and of toroidal angle ϕ', in which the magnetic reconnection occurs. It is clear that, near the ϕ_{NPA} position, there is a local increases of the temperature, at the crash time.

This is effectively more evident in Figure 4.15, which shows the ion temper-

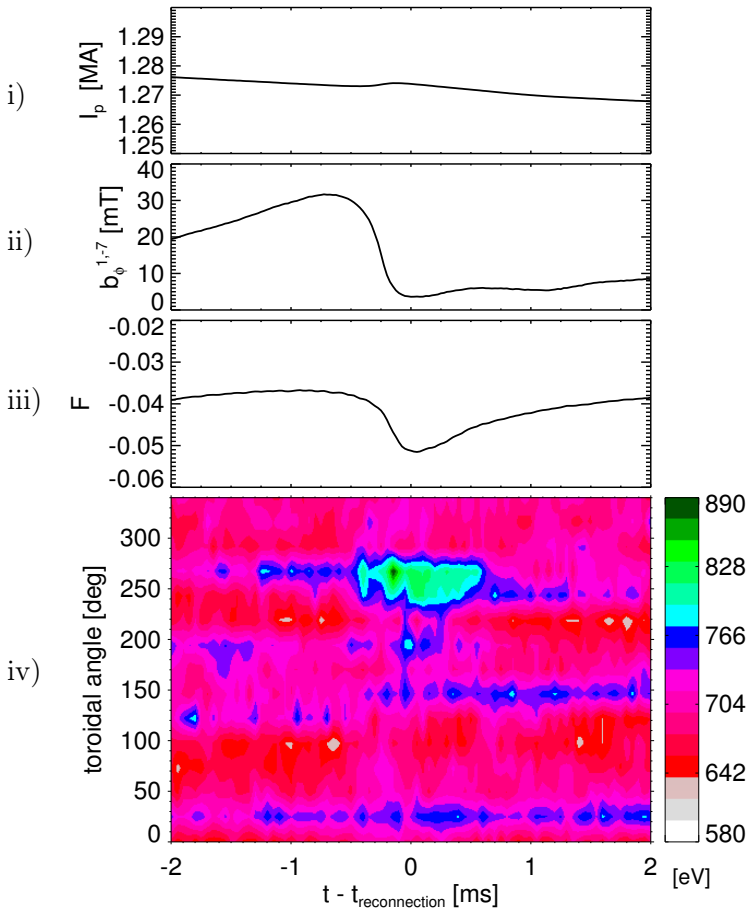

Figure 4.14: From top to bottom: plasma current (i); $m = 1, n = 7$ component of the edge toroidal magnetic field (ii); F reversal parameter (iii); contour-plot of the measured ion temperature as a function of $t - t_{rec}$ and toroidal location of relaxation crash $\phi^{'}$ (iv). All these quantities are averaged over many relaxation crashes.

ature averaged over two different angle intervals. An increase of the thermal ion temperature, of about 200 eV, occurs where the reconnection takes place. From the analysis of neutral fluxes at different energies, it has been found that this local enhancement of the ion temperature appears to be like a transfer of energy between particles. In fact, the fluxes at different energies, normalized

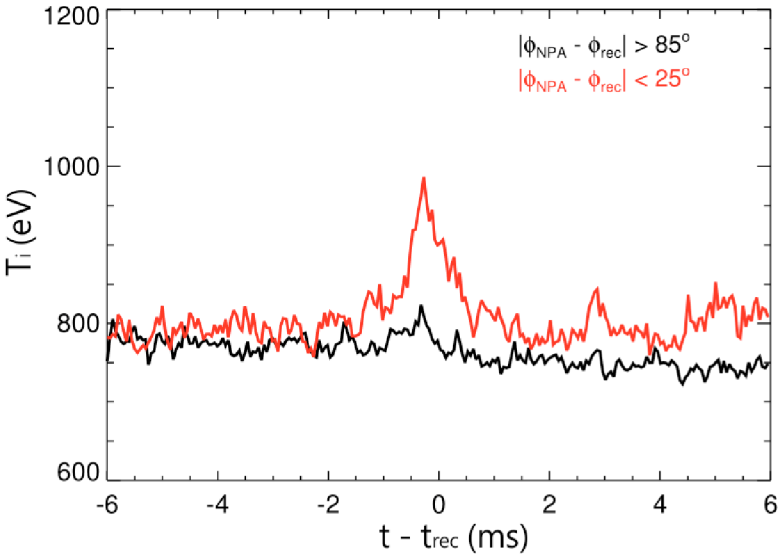

Figure 4.15: Ion temperature averaged on two different toroidal angle intervals. The red curve refers to the formation of the $m = 0$ perturbation in the proximity of the NPA detector. A large localized temperature increase is evident.

to the value at a time before the crash, show different behaviors, as shown in Figure 4.16. This means that reconnection first accelerates high energy particles, which then release, by collisions, the gained energy to the lower energy ones, resulting in a global heating of the thermal ion population.

The timing of the process can be seen in Figure 4.17, which shows the normalized fluxed of three NPA channels versus the lowest energetic one, arrows heads indicating the time verse. In this process, the high energy fluxed increase before the lowest energy ones and this behavior is as higher as the energy gap. Finally, the lowest energy channels appear to be in phase.
It must be noted that, during the relaxation event, the high energy fluxes increase whereas the lowest ones decrease.
The whole process can be thus schematized: at the crash, high energy neutral fluxes increase, but their temperature T^* decreases; the low energy fluxes decrease, but the thermal ion temperature results in a growth; at this stage, the whole distribution flux function is closer to a thermal Maxwellian; after the crash, the plasma cools down again and the flux distribution comes slowly

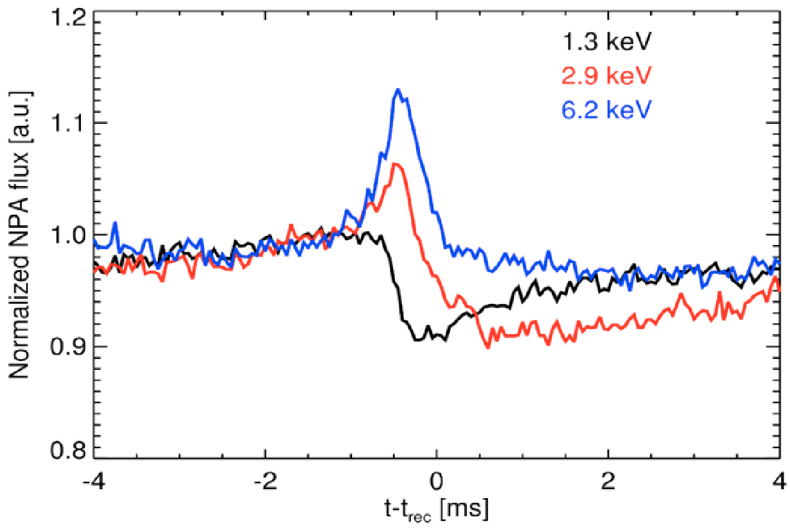

Figure 4.16: Time traces of the normalized NPA fluxes at different energies.

back to pre-crash values.

Here it must be noticed that the events in figures 4.14-4.16 appear to happen a fraction of a millisecond before the reconnection time. This is due to the definition of t_{rec} that could miss a bit of accuracy, as mentioned before. However this does not change the physical conclusions drawn from the analysis of the experimental data.

4.3 Electrostatic analysis

Finally, an analysis of the effects of magnetic reconnection on plasma dynamics has been performed also by means of the insertable U-probe diagnostic. In particular, the intermittent turbulence in the floating potential V_f have been studied.

The time trace of such a signal, measured in the plasma $35mm$ from the vacuum vessel, is shown in Fig. 4.18, along with the plasma current, the reversal parameter and the edge toroidal magnetic field measured by a ISIS pick-up coil. The floating potential, as the magnetic field, is strongly influenced by the reconnection events in the plasma, as can be seen in Figure 4.19, exhibiting a spectrogram of electrostatic pin signals at the plasma edge, averaged

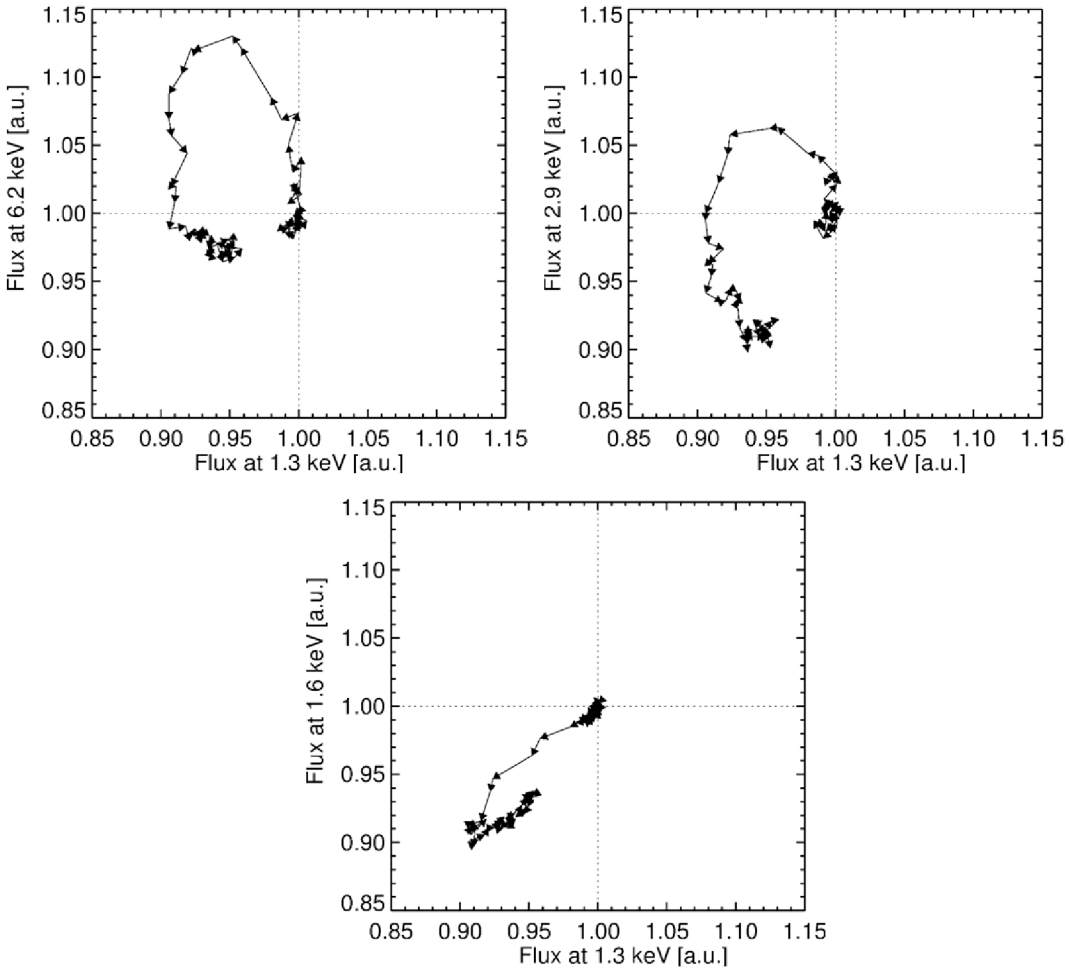

Figure 4.17: Timing comparison of normalized neutral fluxes at different energies. The arrow heads indicate the time direction.

on several relaxation events. It can be seen how the frequency content of the V_f signal increases after the crash.

Therefore, as done for magnetic signals, the intermittency of the floating potential V_f has been studied. The wavelet method of intermittency detection has been used, in a range of wavelet scales varying from 0.5 to 5 μs, that is the typical time range in which the V_f signal exhibits oscillations. A distribution function of intermittency has been obtained by counting the number of intermittent events as a function of their amplitude (that is the variation of the signal in a temporal interval equal to the wavelet scale s), in

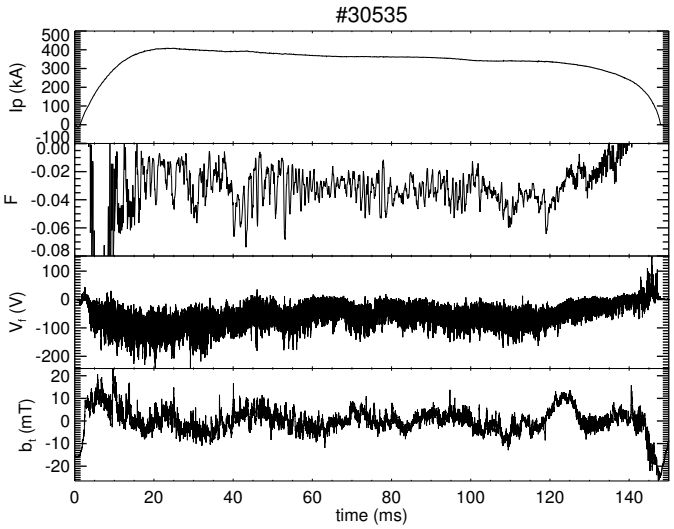

Figure 4.18: Time traces of several quantities in a RFP discharge of RFX-mod. From top to bottom: plasma current; F parameter; fluctuating potential measured by a U-probe pin, inserted 35mm from the vacuum chamber; toroidal magnetic field perturbation measured at the edge by a ISIS pick-up coil.

two equally spaced intervals (4 ms wide), before and during the relaxation crash.

Figure 4.20 shows such distributions obtained for a collection of shallow-F discharges, in which the electrostatic potential has been measured by a pin of the U-probe, inserted inside 35mm from the vacuum vessel. It is clear, from this graph, how reconnection increases the electrostatic turbulent activity of plasma.

A further analysis, aimed to verify the eventual relationship between the intermittent structures of the electrostatic field and the filamentary current structures that have already been observed in RFX-mod at the plasma edge, will be performed as future work.

In conclusion, it has been shown that the current sheets, associated to magnetic reconnection events, can be naturally subject to a fragmentation. The reconnection process strongly influences the magnetic and electrostatic activity of the plasma, generating a wide distribution of intermittent phenomena. During such events, the fast acceleration of high energy particles and the

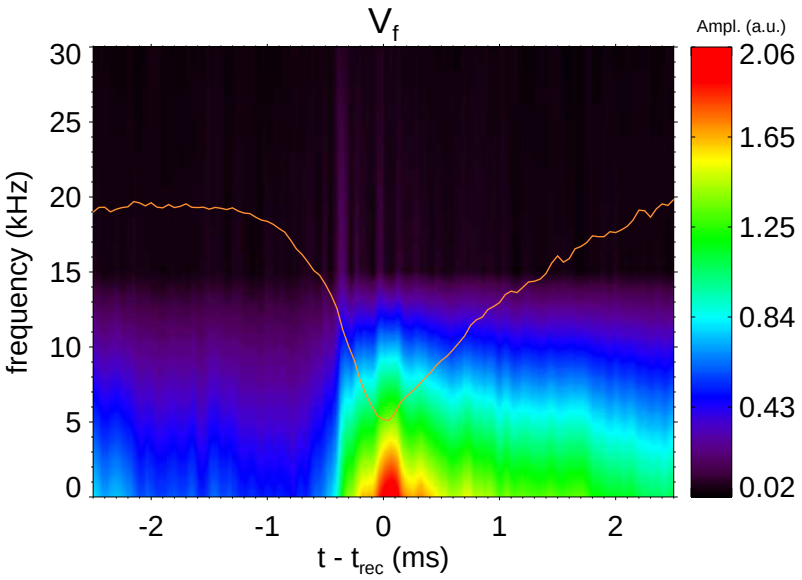

Figure 4.19: Spectrogram of floating potential signals measured by a U-probe pin at the plasma edge, averaged over several relaxation events. The averaged F parameter is superimposed (orange line) in order to highlight the crash. A variation of frequency content after the reconnection events can be easily observed.

localized increase of the ion temperature has been observed.

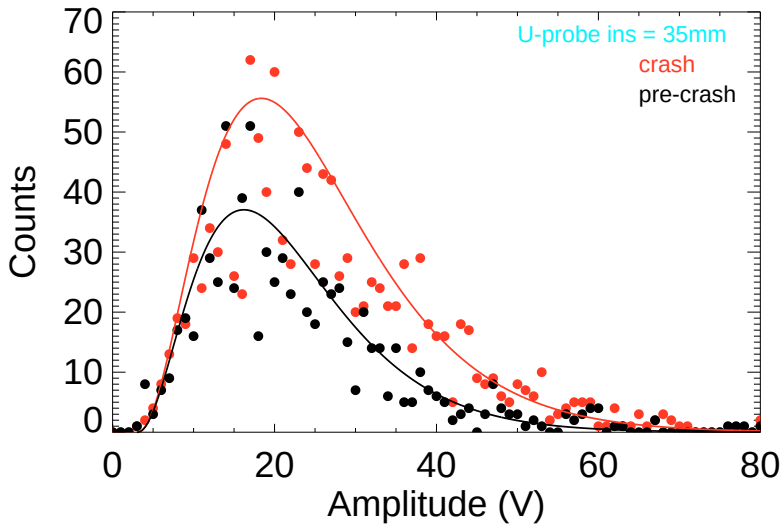

Figure 4.20: Distribution of intermittent events detected in the floating potential signal of a U-probe pin, inserted 35mm from the vacuum vessel. Data are collected, for several relaxation events, in equally spaced temporal interval, before (black points) and during (red points) the magnetic reconnection. Black and red lines are only guides for eyes.

Chapter 5

Tearing mode dynamics in RFX-mod tokamak

In this chapter, the study of tearing modes in the RFX-mod tokamak plasmas, integrating analysis of magnetic, flow and kinetic measurements, is presented. In particular, the diamagnetic drift component of the rotation frequency is investigated.

TMs are a concern for fusion plasmas, being characterized by magnetic islands, whose topology tends to flatten locally the pressure profile and to increase the particle and energy radial transport. Therefore large magnetic islands load to confinement degradation. Moreover, the global plasma column distortion, produced by the mode, increases the plasma-wall interaction. TMs are a major obstacle towards the achievement of high-performance fusion plasmas. Mode amplitude and the related detrimental effects are mitigated by the spontaneous TM rotation with the plasma. In fact,3 mirror currents induced onto the containment wall(s), always having finite conductivity, screen the radial field therein. However, the electromagnetic torque developed by the interaction between TM and these mirror currents can stop the TM rotation in the laboratory frame (wall-locking) as soon as the amplitude exceeds a certain threshold [115, 116]. When this occurs, the stabilizing effect of the wall(s) is lost, and the TM amplitude increases at a rate given by the wall(s) resistive time constant(s). This phenomenon usually leads to

a rapid termination of the discharge (disruption).
Most of the current tokamak devices have a significant rotational momentum, provided by Neutral Beam Injector (NBI) systems, which strongly affects TM dynamics . However, in ITER and future reactors, NBI systems are not expected to provide much momentum. In this respect, the purely ohmic RFX-mod tokamak plasmas [117, 29] can give significant contribution to the study of TM physics in absence of external momentum sources.
In tokamaks, TMs are often seen to rotate with the electron fluid [118]. This has been also observed in RFP discharges of RFX-mod for $I_p < 150kA$, where their spontaneous rotation can be established due to the small amplitudes in such low current conditions [119]. In these cases, TM frequencies differ from the ion fluid rotation frequency, the quantity measured by spectroscopic diagnostics, owing to the diamagnetic drift.
Present chapter mainly discusses the connection between TM frequencies, as detected by the ISIS magnetic probes, and flow velocity, as reconstructed from spectroscopic and kinetic measurements, in the ohmic tokamak discharges of RFX-mod. It is shown that the diamagnetic drift provides the dominant contribution to TM frequency. Moreover, the spin-up/slow-down observed in conjunction with TM amplitude decrease/increase is hardly explained in terms of the above mentioned electromagnetic interaction with the conductive wall. Instead, indications that this dynamic is related to mode-island-induced modifications of the kinetic profiles (mainly temperature), which determine the diamagnetic drift, are provided. To the author knowledge, this is not a standard interpretation of the TM rotational dynamic, hence the analyses here reported can be regarded as new results.
The chapter is organized as follows. In section 5.1, the adopted techniques for the detection and characterization of TMs, both in terms of amplitude and rotation frequency, based on the in-vessel magnetic measurements, are presented. The Fourier analysis of the pick-up probes signals are interpreted in terms of a standard MHD model based on the cylindrical Newcomb's equation [115, 116]. This allows an extrapolation inside the plasma of the TM measured amplitudes to obtain an estimate of the island width. A new statistical analysis of disruptions marked by TMs confirms previous results

obtained with out-vessel probes in a recent paper [29].
Section 5.2 is devoted to the flow analysis, with the identification of the ion and diamagnetic components of the velocity. The comparison with the magnetic analysis shows that TM frequency is mainly determined by the diamagnetic drift. Section 5.3 compares the TM slowing down, occurring typically prior to the disruptions, with the electromagnetic model of the interaction with the vacuum-vessel. Finally, in section 5.4, the observation of periodic oscillations of TM frequency and amplitude, dubbed as *limit cycle*, is presented. The relationship with the sawtooth activity is also shown.

5.1 Magnetic analysis

In RFX-mod the magnetic analysis of slowly varying quantities, such as the equilibrium field or slowly rotating TMs, are performed by means of a system of probes placed outside of the vacuum vessel. Nevertheless, because of the screening effect of the vacuum vessel, these probes are not able to detect the fast rotating TMs (with frequencies greater than few 10^2 Hz, as order of magnitude). Therefore, the magnetic measurement of fast TM rotation is performed by means of the magnetic probes of ISIS. In particular, relatively to the analysis presented in Chapter 2, the time derivative of poloidal and radial magnetic field perturbations are measured at the plasma edge by means of the two poloidal arrays of 8 poloidal and radial coils each. The time derivative of the toroidal field perturbations are measured by means the two arrays of 48 toroidal coils each.
The uniform distribution of these pick-up coils in the poloidal and toroidal directions allows the identification of (m, n) TMs by means of spatial and temporal Fourier transforms.
The adopted procedure is here summarized:

- A spatial Fourier transform, performed on the poloidal array signals, provides the decomposition of the magnetic perturbations in terms of the Fourier modes, with poloidal number $m \leq 3$ (no information can be deducted on the n components on these signals);
- A Fourier spectrogram is performed on each m-component, for which

the dominant frequency component, if any, is determined as a function of time;

- A similar spatial Fourier transform is performed on the signals of the toroidal coils, thus discriminating magnetic perturbations with toroidal mode number $n < 24$ (likewise, no information can be extracted on the poloidal mode numbers m);
- The dominant frequency for each n mode is estimated by analyzing the Fourier spectrogram;
- The m, n modes are identified by matching the dominant frequencies obtained at the previous steps.

Just as example, in Figure 5.1a the frequency power spectra, estimated during the flat-top phase, of the $n = 1$ and $m = 2$ components, for the same time interval, are superimposed. As clearly seen, each spectrum shows a dominant

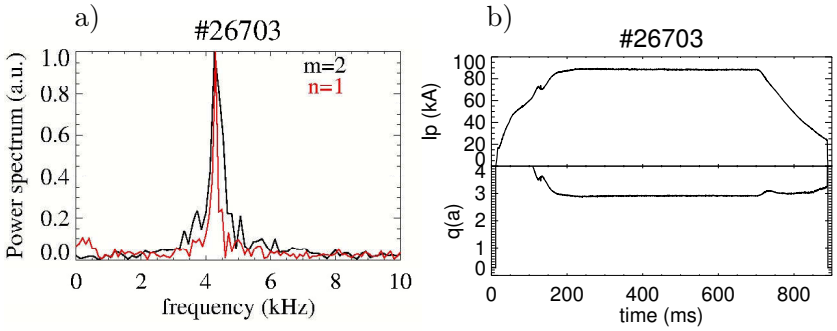

Figure 5.1: a) Frequency spectrum of the $m = 2$ (black curve) and $n = 1$ (red curve) magnetic fluctuation performed at time $t = 320ms$ for the #26703 tokamak discharge. Amplitudes are normalized to unity. Both $m = 2$ and $n = 1$ components exhibit a dominant frequency at about 4.3 kHz. b) Time trace of plasma current (top) and edge safety factor (bottom).

peak, with the same central frequency. This allows for the identification of a (2,1) mode. From the value of the safety factor to the edge ($q(a) \sim 3$), shown in Figure 5.1b, and knowing that the q profile increases with the radius, with a value around unity in the axis, it can be deduced that the identified mode is a tearing mode, internally resonant at the position where $q = 2$.

In Figure 5.2 the spectrogram of the $m = 2$ (i) and $n = 1$ (ii) components are shown, together with the time trace of the plasma current I_p (iii) and the cylindrical edge safety factor q_a (iv), for a typical tokamak discharge. Apart

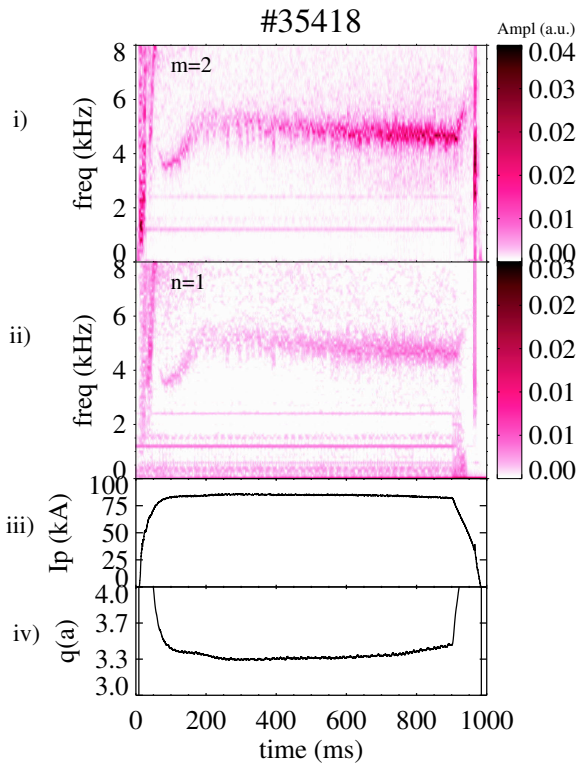

Figure 5.2: From top to bottom: spectrogram of m=2 (i) and n=1 (ii) magnetic fluctuations, time evolution of plasma current Ip (iii) and edge safety factor q(a) (iv) for #35418 tokamak discharge.

from the frequency variations observed during the rising and falling phases of the current, a (2,1) TM is rotating at a quite constant frequency of about 4.5 kHz, during the whole flat-top phase of the plasma current. The almost vertical lines, that can be seen in the spectrogram at $t < 50ms$, are due to resonant modes that are excited while the safety factor rapidly varies during the ramp-up of the plasma current at the initial stage of the discharge. Furthermore, it must be noted that the horizontal bright stripes, centered around 1.2 and its higher harmonic 2.4 kHz, are due to electronic disturbances and they must be opportunely filtered in order to correctly estimate the TM amplitude and phase.

Figure 5.3 shows the same quantities of the previous Figure 5.2 for a different tokamak discharge. As can be seen, a (2,1) TM similarly rotates at a frequency around 4.5 kHz, but, after 550 ms, the frequency slows down to

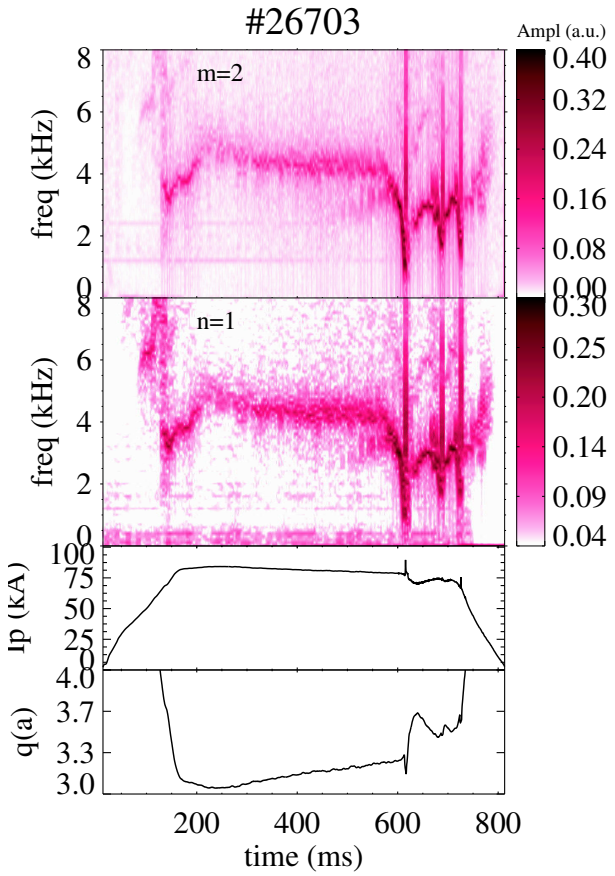

Figure 5.3: Same quantities of figure 5.2 for shot #26703. After $t \sim 550ms$ the (2,1) slows down and the plasma disrupts.

about 500Hz and the plasma disrupts. The disruption is identified by a spike in both safety factor and plasma current at $t \sim 620ms$. At the same time, the spectrogram shows a vertical band indicating a sudden variation of the frequency spectrum.

Fortunately, this events are not really harmful for the RFX-mod device because the plasma current is not very high, if compared to other currently operating machines, and the system control is able to sustain the plasma still a more longer.

By the spatial and temporal Fourier analysis, it is possible to determine amplitude, phase and frequency of each mode.

It must be noted that only the radial and poloidal magnetic field signals

have been considered in the present thesis. The amplitude of the toroidal component has not been taken into account, being the toroidal field signal-to-ratio at the edge too small for a reliable estimation. The signals collected by the toroidal arrays have been used only for the identification of TM mode numbers.
In RFX-mod, alongside the (2,1) TM, both its toroidal sideband (3,1), and the (3,2) TM are detected by the pick-up coils of ISIS.
As already mentioned, the study of the high frequency rotation of TM and the slowing down is important to understand the main mechanisms that drive them and, possibly, learn how to control them. Therefore this analysis requires a good time resolution for the determination of such a frequency. In particular, such a resolution cannot be achieved, especially during the slowing down phases, with the standard Fourier analysis. The frequency behavior of the TM, as a function of time, $f(t)$, has been thus determined as the time derivative of the phase Φ, given by the spatial Fourier transform ($f(t) = \dot{\Phi}(t)/2\pi$). Such estimation is not trivial from the ISIS signals, as $\dot{\Phi}(t)$ can be affected by high frequency disturbances and, as mentioned before, by low frequency noise. For this reason, a pass-band filter around the central frequency has been applied to the signals. It must be noted that, during the slowing down phase, the amplitude of the mode increases, which indeed allows a better determination of $\dot{\Phi}(t)$ and, consequently, of the frequency itself.

5.1.1 Comparison between ISIS measurements and a MHD model

It is mandatory to assess the compatibility between the result coming from the procedure just described and standard MHD models. As basic description [115], cylindrical geometry, Newcomb's equation for the radial profile of the magnetic perturbation, and the thin-shell dispersion relation [120] are taken into account in order to model the diffusion across the passive conductive structures, considered as uniform layers.
In this paragraph the relationship between the fluctuating b_r and b_θ magnetic

field components of a given (m, n) tearing mode, as detected by ISIS on the vessel inner surface, with the prediction of the above model are compared.
In the kHz frequency range, the screening effect of the vessel onto br is very important. The RFX-mod vacuum vessel is a complex three-dimensional structure made by Inconel 625 [121], with inner and outer radii $r_w = 0.475$, $r_v = 0.505$ respectively. It has been modelled by two thin shells, the innermost placed at $r = r_w$ with time constant $\tau_w \sim$ 1ms, the outermost placed at $r = r_v$ with time constant $\tau_v \sim \tau_w/2$. In the above frequency range, the 100ms time constant, outermost ($b = 0.5125$) copper shell can be approximated as ideal. Hence, b_r is set to zero there.
The m, n Fourier harmonic of the magnetic perturbation radial profile (referred to the basis $e^{i(m\theta - n\phi)}$) satisfies the Newcomb's equation. It is convenient using the expansion made with the basis $\hat{\psi}_s(r)$, $\hat{\psi}_w(r)$, $\hat{\psi}_v(r)$ of real, independent solutions:

$$-irb_r^{m,n} \equiv \psi^{m,n}(r,t) \equiv \psi_s(t)\hat{\psi}_s(r) + \psi_w(t)\hat{\psi}_w(r) + \psi_v(t)\hat{\psi}_v(r) \qquad (5.1)$$

The superscript m, n in the r.h.s have been dropped for ease of notation. The solution $\hat{\psi}_s(r)$ is regular at $r = 0$, equal to 1 at the mode resonant surface r_s, 0 at $r \geq r_w$; the solution $\hat{\psi}_w(r)$ is 0 at $r \leq r_s$, 1 at r_w, 0 at $r \geq r_v$; the solution $\hat{\psi}_v(r)$ is 0 at $r \leq r_w$, 1 at r_v, 0 at $r \geq b$. Accordingly, the complex coefficients $\psi_s(t), \psi_w(t), \psi_v(t)$ encapsulate amplitude and phase of the perturbation respectively at the resonant surface, at the innermost vessel surface and at the outermost vessel surface.
The solution basis of (5.1) is computed for the zero-pressure Newcomb's equation, a reasonable approximation, given the low-β, ohmic plasmas of RFX-mod. The radial function $\psi_{m,n}$ is everywhere continuous, but in general its first derivative has a discontinuity at r_s, r_w, r_v, modelling the presence of localized currents therein. Those at r_w, r_v rule the diffusion of the radial field across the vessel.
To this purpose, the thin-shell dispersion relation $\tau_x \partial\psi^{m,n}/\partial t \equiv [r\partial\psi^{m,n}/\partial r]_{r_x-}^{r_x+}$,

being $x = w, v$, is taken into consideration. Exploiting (5.1), one gets

$$i\omega\tau_w\psi_w = E_{sw}\psi_s + E_{ww}\psi_w + E_{vw}\psi_v \tag{5.2}$$

$$i\omega\tau_v\psi v = E_{wv}\psi w + E_{vv}\psi_v \tag{5.3}$$

where $\omega = 2\pi f$, with f the mode frequency, and the real coefficients $E_{yx} = rd\hat{\psi}_y/dr\Big|_{r_X-}^{r_x+}$ encapsulate the derivative discontinuities of $\hat{\psi}_y(y = s, w, v)$ at $r = r_x(x = w, v)$. It must be also taken into account that in vacuum [116]

$$b_\theta^{m,n} = -\frac{m}{m^2 + n^2(r/R)^2}\frac{\partial}{\partial r}\psi^{m,n} \tag{5.4}$$

From (5.1)-(5.4), the (complex) ratio between the m, n harmonics of poloidal and radial field, taken on the inner surface of the vessel where the ISIS sensors are located, is

$$\frac{b_\theta^{m,n}}{ib_r^{m,n}}\bigg|_{r_w-} = -\frac{m}{m^2 + n^2(r_w/R)^2}[A(\omega) + iB(\omega)] \tag{5.5}$$

with

$$A(\omega) = \frac{E_{vw}E_{wv}E_{vv}}{\omega^2\tau_v^2 + E_{vv}^2} - r_w\left.\frac{d\hat{\psi}_w}{dr}\right|_{r_w+}, \quad B(\omega) = \omega\left(\tau_w + \frac{E_{vw}E_{wv}}{\omega^2\tau_v^2 + E_{vv}^2}\tau_v\right) \tag{5.6}$$

All the parameters E_{yx} in (5.6), as well as $d\hat{\psi}_w/dr\Big|_{r_w+}$, refer to the vacuum region, hence they do not depend on plasma equilibrium. Quantities A, B very weakly depend on the mode numbers m, n. Therefore, the phase difference between b_θ and b_r is almost the same function of ω for different modes, and tends to $\pi/2$ for $\omega \to 0$.

Predictions from equations (5.5), (5.6) compare fairly well with experimental measurements of fluctuating b_r and b_θ. In figures 5.4, 5.5 specific examples are provided for shots #35364 and #34642. In the former, $q_{cyl}(a) \sim 3$ and the dominant detected harmonics pertain to the $(2, 1)$ tearing mode and its toroidal sideband $(3, 1)$. Equation (5.5) is evaluated with $\tau_w = 1.2$ ms and

$\tau_v = \tau_w/2$. In the latter, the $m = 2$, $n = 1$ tearing mode is replaced by the $m = 3$, $n = 2$ tearing mode, being $q_{cyl}(a) \sim 1.75$. In this case equation (5.5) is evaluated with $\tau_w = 1.1$ms and $\tau_v = \tau_w/2$. The detection of the $(3, 2)$ mode

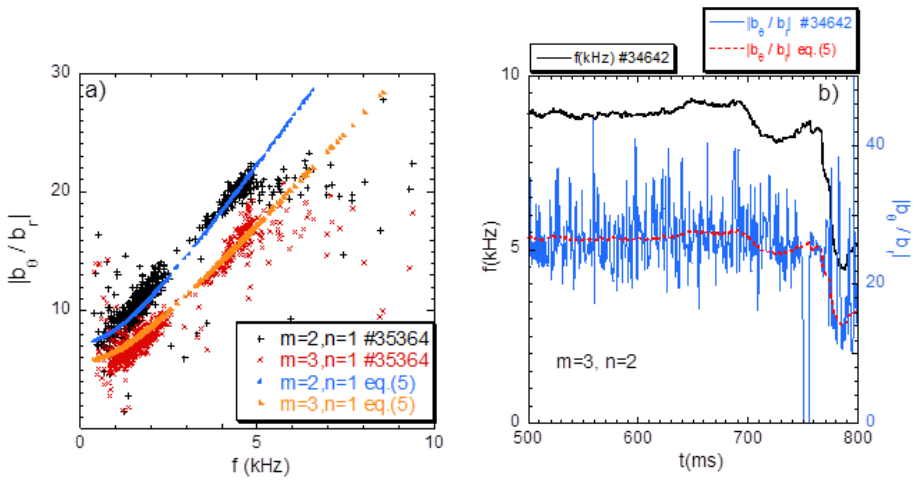

Figure 5.4: Ratio between the poloidal and radial field amplitudes. a): experimental data from shot #35364 for harmonics $m = 2, 3$, $n = 1$ plotted as function of frequency, alongside prediction from equation (5.5); in this particular shot, the mode slows down from $f \sim 4$kHz to $f \sim 2$kHz in the second half of the discharge. b): experimental data from shot #34642 for the harmonic $m = 3$, $n = 2$ plotted as function of time, alongside prediction from equation (5.5); in this particular shot the mode slows down from $f \sim 9$kHz to $f \sim 5$kHz in the final part of the discharge.

is not as reliable as for the $(2, 1)$ mode, owing to its very small amplitude. Therefore, the experimental data for the $(3, 2)$ are rather scattered. Figure 5.4a shows that the amplitudes ratio $|b_\theta/b_r|$ increases with f in both shots, due to the screening of the vessel onto the radial field. Figure 5.5 shows that the phase difference between b_θ and b_r, decreasing with f, is insensitive to the mode number. These results show that the ISIS data can be integrated within the model to extrapolate the magnetic perturbation inside the plasma. In particular, this allows an estimate of the TM island width, as described in the next paragraph.

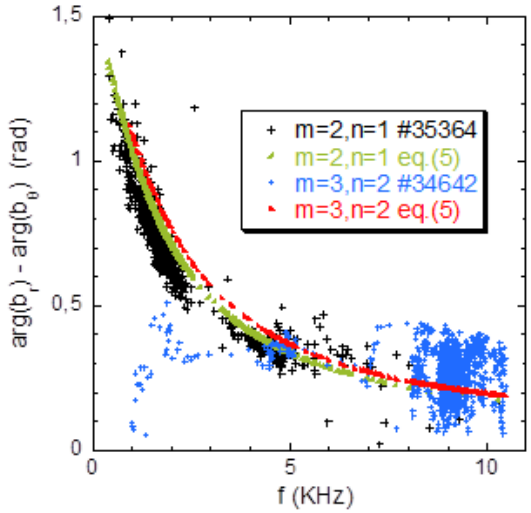

Figure 5.5: Phase difference as function of frequency. Experimental data from shot #35364 for harmonic $m = 2$, $n = 1$ and from shot #34642 for harmonic $m = 3$, $n = 2$ are shown, alongside prediction from equation (5.5).

5.1.2 Estimate of the island width

According to a standard text-book formula the 'nominal' island width is given by the mode amplitude at the resonant surface divided by an equilibrium related coefficient, the expression being given by eq. (3.43) [113]:

$$W = 4(|\psi_s / F_0'(r_s)|)^{\frac{1}{2}} \ , \qquad F_0(r) \equiv mB_{0\theta} - nB_{0\phi} r/R_0 \ , \qquad ' \equiv d/dr \tag{5.7}$$

The subscript '0' denotes equilibrium quantities, and it is implicit that the perturbed quantities refer to the m, n harmonic. We speak of 'nominal' width since (5.7) is valid under the so-called 'constant-ψ approximation', i.e. when $\psi^{m,n}$ weakly varies within the island. For macroscopic islands this assumption is not justified, in particular for the $(2, 1)$ mode. In these cases the reconstruction of the island topology can be done only numerically by combining the radial profiles of both equilibrium and $\psi^{m,n}$. Nonetheless, for high-frequency $(2, 1)$ and $(3, 2)$ tearing modes, the radial function $|\psi^{m,n}|$ can be approximated by a linear decreasing trend vanishing at the first wall (the vessel inner surface r_w), in the region $r \geq r_s$ beyond the resonant surface. In such a case a refinement of formula (5.7), as far as the maximum 'external'

radial excursion of the island is concerned, can be straightforwardly found: in appendix 5.5 it is shown that the point on the island separatrix corresponding to the maximum radius is:

$$r_{island,ext} = r_s + \frac{W}{2} - \frac{W^2}{16(r_w - rs)} \tag{5.8}$$

Quantity W denotes the 'nominal' width defined by (5.7). Formula (5.8) improves the 'constant-ψ expression' $r_{island,ext} = r_s + W/2$. Finding a formula similar to (5.8) for the *inboard* side of the island, which combined with (5.8) gives the *true* island width, does not seem an easy task, due to the non-monotonic, equilibrium-dependent behavior of $|\psi^{m,n}|$ for $r \leq r_s$.

To carry out (5.7), (5.8) an estimate of $|\psi_s|$ is needed. From (5.1) and (5.4)

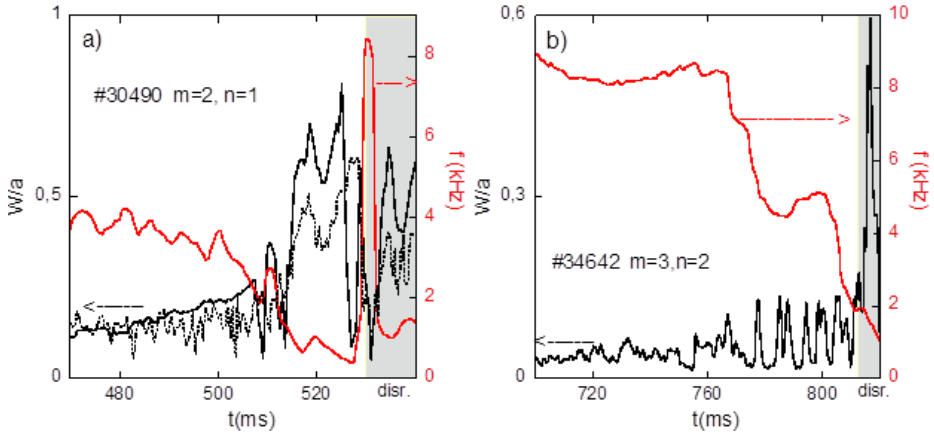

Figure 5.6: Estimates of the normalized island width W/a, reported in black: continuous line, from ISIS measurements, dotted line, from out-vessel probes (limited to plot a). Mode frequency, from ISIS measurements, is shown in red. The disruptive phase is shaded in gray. Plot a) displays the $m = 2$, $n = 1$ mode for shot #30490: in the examined interval, $q_{cyl}(a) \sim 3$, and density is in the range $n_e/n_G \sim 0.75$. Plot b) displays the $m = 3$, $n = 2$ mode for shot #34642: in the examined interval, $q_{cyl}(a) \sim 1.8$, and density is in the range $n_e/n_G \sim 0.2$.

$|\psi_s|$ can be related to the ISIS measurements b_r, b_θ on the inner surface of the vessel in the following way:

$$|\psi_s|^2 = \{K^2 |b_\theta|^2 + H^2 |b_r|^2 - 2KH |b_\theta| |b_r| sin[Arg(b_r) - Arg(b_\theta)]\}_{r_w -} \tag{5.9}$$

$$K = \frac{m^2 + n^2(r_w/R)^2}{m}\frac{r_w}{E_{sw}} \ , \qquad H = \frac{r_w}{E_{sw}}\left(E_{ww} - r_w \frac{d\hat{\psi}_w}{dr}\bigg|_{r_w+}\right) \tag{5.10}$$

Since $|b_r| \ll |b_\theta|$ for an high frequency mode, $|\psi_s| \simeq K|b_\theta(r_w-)|$. The coefficients E_{ww}, E_{sw} are equilibrium dependent. An example of W estimate for the $(2,1)$ mode is shown in Fig. 5.6a (black continuous line), where the growth of a large island ($W/a > 0.5$) eventually triggers a disruption ($t = 530$ms), which is identified by a positive spike in plasma current (not shown).

A similar evaluation, based on the outer standard sensors (black dotted line), discards the screening of the vessel so giving a comparable, but smaller result. The growing mode slows down during the pre-disruptive phase (from

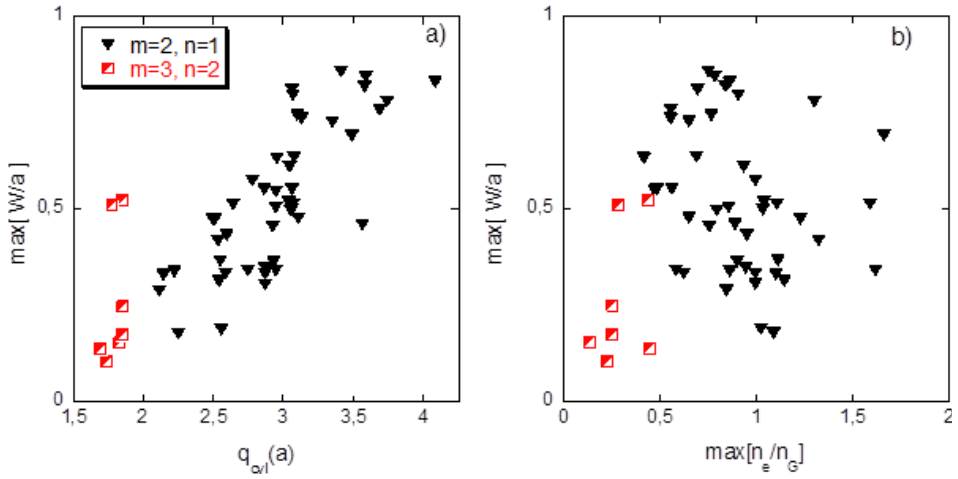

Figure 5.7: Statistical analysis on a database of disrupted discharges, showing a slowing down of the dominant tearing mode. The maximum W/a is plotted against the edge cylindrical safety factor (a) and the maximum value of n_e/n_G (b). All quantities are estimated within $10 \div 20$ms before the disruption.

$f \sim 4$kHz to $f \sim 0.4$kHz; the following transient acceleration marks the disruption) without locking to the wall in the strict sense. This is the signature of the majority of the $(2,1)$ induced disruptions, as highlighted by a previous study based on the out-vessel sensors [29]. In fact, the penetration through the innermost vacuum-vessel, concomitant to the mode growth and slowing

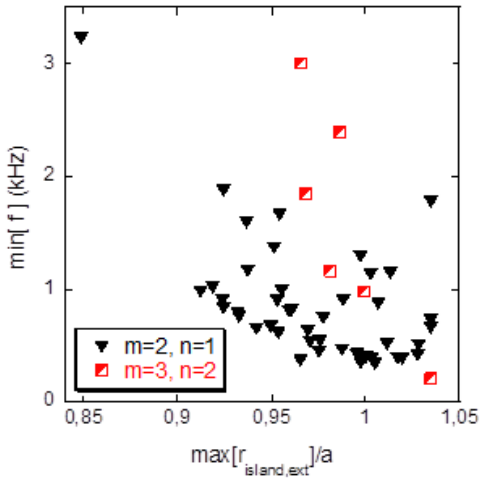

Figure 5.8: Different analysis on the same shots considered in figure 5.7. The minimum frequency is plotted against the maximum value of the outward island radius, as given by formula (5.8). Both quantities are estimated within $10 \div 20$ms before the disruption.

down, is sufficient to provoke a disruption when $q_{cyl}(a) > 2.5$.

A similar W estimate for the $(3, 2)$ mode is shown in figure 5.6b. The maximum island width prior to the disruption is significantly smaller ($W/a < 0.15$) than the typical $(2, 1)$ disruptive values. The disruption occurs after a slowing down of the mode from $f \sim 8$kHz to $f \sim 2$kHz. A growing amplitude, slowing down TM is the signature of the majority of the disruptions observed in the RFX-mod tokamak. Regardless of the fact that TM is or not the original cause of the disruption, it surely takes a part in the final process. Therefore it is interesting to analyze the island width in the pre-disruptive phase of the discharge.

A new statistical analysis over a database of discharges disrupted after a slowing down of the dominant tearing mode ($m = 2$, $n = 1$ or $m = 3$, $n = 2$) refines previously published results from outer magnetic sensors (figures 5-7 of [29]). Note that the statistic for the $m = 3$, $n = 2$, where reliable ISIS data can be extracted, is rather poor. Figure 5.8 shows that the island external radius, given by equation (5.8), gets close or even beyond the plasma surface ($a = 0.459$) in the pre-disruptive phase. Figure 5.7a confirms figure 6b) of reference [29]: the $m = 2$, $n = 1$ (nominal) island width increases with $q_{cyl}(a)$, i.e. with the distance of the resonant surface from the shell. For

the $m = 3$, $n = 2$ island, the range of $q_{cyl}(a)$ is not wide enough to establish a clear trend. Figure 5.7b shows that, at least for the examined cases, the $m = 3$, $n = 2$ induced disruptions occur at smaller W/a and n_e/n_G (i.e. line-average density/Greenwald density) with respect to those caused by the $m = 2$, $n = 1$. Nonetheless, figure 5.8 shows that the island external radius, given by equation (5.8), gets close or even beyond the plasma surface ($a = 0.459$) in the pre-disruptive phase for both $m = 2, n = 1$ and $m = 3, n = 2$ TMs. The minimum rotation frequency attained by TM before the disruption is better correlated with this quantity, which combines both equilibrium and W, than with the maximum island width alone.

5.2 Flow analysis

This section is the core of the chapter, since the connection between the TM frequencies detected by ISIS and the plasma flow is established.

5.2.1 Model of TM rotation

A two-fluid MHD cylindrical model has been already used in [119] to interpret the tearing mode fast rotation frequencies observed in low-current RFP plasmas ($Ip \leq 100$kA) of RFX-mod. Basically, the m, n TM island, which develops at the resonant surface, is assumed to be frozen within the electron fluid. From a theoretical point of view, this hypothesis should be justified only for small-size islands, unable to flatten significantly the pressure profiles at the resonant surface [122, 123].
Following the assumption and referring the harmonics to the basis $e^{i(m\theta - n\phi)}$, the island phase velocity is given by a combination of poloidal and toroidal equilibrium angular velocities ($\Omega_\phi = V_\phi/R_0$, $\Omega_\theta = V_\theta/a$) of the electron fluid at the resonant radius $r = r_s$:

$$\frac{d\varphi^{m,n}}{dt} = n\Omega_{\phi,e}(r_s,t) - m\Omega_{\theta,e}(r_s,t) = \frac{n}{R_0 B_\theta}(\mathbf{B}\times\mathbf{V}_e)_r\Big|_{r_s} \tag{5.11}$$

In order to obtain the last equality, use has been made of $q(r_s) = m/n = rB_\phi/(R_0 B_\theta)|_{r_s}$. Note that, only the velocity perpendicular to $\mathbf{B}$ contributes to (5.11). This equation is managed in order to express $d\varphi^{m,n}/dt$ in terms of the total ion velocity combined with the *diamagnetic components* of electron and ion velocities. In fact, the former can be estimated by spectroscopic diagnostic, the latter by pressure profile reconstruction. Taking the perpendicular velocity, in the absence of any external momentum input, as the sum of $\mathbf{E} \times \mathbf{B}$ and diamagnetic drifts, the total velocity is:

$$\mathbf{V}_p = \mathbf{V}_p^{ExB} + \mathbf{V}_p^{diam} + \mathbf{V}_p^{//} \ , \qquad p = e, i \tag{5.12}$$

The last term of the r.h.s. is the parallel component, irrelevant in (5.11). The $\mathbf{E} \times \mathbf{B}$ drift is independent on the mass and on the charge of the particles, hence the electron velocity is given by:

$$\mathbf{V}_e = \mathbf{V}_i + \mathbf{V}_e^{diam} - \mathbf{V}_i^{diam} + \mathbf{V}_e^{//} - \mathbf{V}_i^{//} \tag{5.13}$$

By combination of (5.11) and (5.13), one ends up with the formula:

$$\frac{d\varphi^{m,n}}{dt} = n\Omega_{\phi,i}(r_s, t) - m\Omega_{\theta,i}(r_s, t) + \frac{m}{en_e r B_\phi} \frac{d(p_e + p_i)}{dr}\bigg|_{r_s} \tag{5.14}$$

Symbol $e > 0$ denotes the electron charge magnitude, n_e the electron density ($= n_i$), p_e, p_i electron and ion pressure respectively. According to this model, the tearing mode rotation frequency can be estimated by knowledge of ion velocity, pressure and density profiles.
The angular phase velocity has hence two main contributions: a 'flow' term,

$$\Omega_{flow}(r_s, t) = n\Omega_{\phi,i}(r_s, t) - m\Omega_{\theta,i}(r_s, t) \tag{5.15}$$

associated to the ion flow velocities; and a 'diamagnetic' term,

$$\Omega_{diam}(r_s, t) = \frac{m}{en_e r B_\phi} \frac{d(p_e + p_i)}{dr}\bigg|_{r_s} \tag{5.16}$$

given by pressure and density profiles.
Evaluation of (5.15), (5.16) requires knowledge of r_s, which in turns is obtained from the $q(r)$ profile. Since there are no tools available for a direct measurement, $q(r)$ is reconstructed by means of an equilibrium code [124][20] able to extrapolate the edge (out-vessel) magnetic measurements by assuming a toroidal force-free plasma with circular cross section. This code, optimized for the RFP, has been recently extended to the tokamak low-beta configuration too.

5.2.2 Evaluation of Ω_{flow}

In the present RFX-mod tokamak plasma, ion velocity is estimated by means of a multi-chord Doppler spectroscopy diagnostic, which measures the impurity emissions integrated on several poloidal and toroidal lines of sight [125]. Three spectrometers allow to simultaneously acquire the spectra of three different ions, in particular CIII (λ = 4647 Å), CV (λ = 2271 Å) and OV (λ = 6500 Å), and hence to deduce their toroidal and poloidal flows. A 1D transport code simulates the radial emission profiles of each ion in order to calculate their mean radial positions and then to reconstruct the toroidal and poloidal flow profiles [126]. It has been found that the experimental flow profiles are well described by the following radial profiles, justified in [127]:

$$\Omega_{\phi,i}(r) = \Omega_{\phi,i}(0)\left(1 - \frac{r^2}{a^2}\right) \tag{5.17}$$

$$\Omega_{\theta,i}(r) = \Omega_{\theta,i}(0)\frac{F(r)}{F(0)}\ , \qquad F(r) = \left(1 - \frac{a}{r}\frac{I_1(\alpha r/a)}{I_1(\alpha)}\right) \tag{5.18}$$

with $\Omega_{\phi,i}(0)$ and $\Omega_{\theta,i}(0)$ of about 7 km/s and 1 km/s, respectively. Here I_1 represents the first-order modified Bessel function, and $\alpha = \sqrt{\tau_V/\tau_D}$, being τ_V the viscous diffusion time and τ_D the poloidal-flow damping characteristic time. The spectroscopic diagnostic allows setting the global coefficients $\Omega_{\phi,i}(0)$ and $\Omega_{theta,i}(0)$, but not α, which is an almost free parameter, being τ_V and τ_D of difficult estimate. Here the values $\tau_V = 60ms$ (of the order of the energy confinement time) [29], and $\tau_D = \tau_V/500$ have been taken. The

latter choice is motivated by the strong damping observed for the poloidal flow, which implies $\tau_D \ll \tau_V$. However, a sensitivity study on α of the TM frequency computed from (5.14) will be provided later on in paragraph 5.2.5.

5.2.3 Evaluation of Ω_{diam}

This term is obtained by reconstructions of density and temperature radial profiles. The density profile is computed by the inversion of the interferometer data [128], by means of a numerical code on the flux coordinate [45]. The electron temperature profile is resolved by means of a Thomson scattering diagnostic [129], measuring T_e at 78 radial positions, with a spatial resolution of about 10 mm. A fit procedure is carried out by exploiting the following model:

$$T_e(r) = T_0 \left(1 - \left(\frac{r}{a}\right)^{\alpha}\right)^{\beta} + T_{edge} \tag{5.19}$$

The fit procedure depends on four parameters α, β, T_0 and T_{edge}, the last

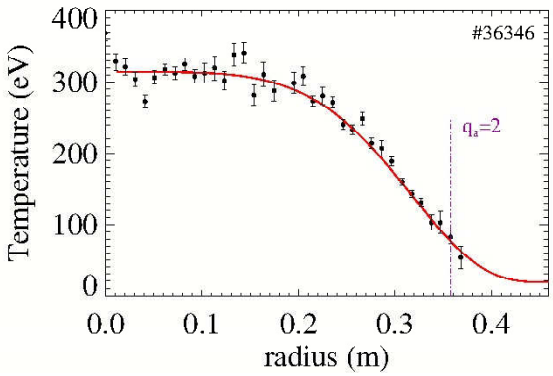

Figure 5.9: Example of electron temperature radial profile, measured by the Thomson scattering diagnostic. The best fit (eq. (5.19)) is represented by a red line. A vertical light-blue line indicates the position of the $m = 2$,$n = 1$ resonant radius

of which, the edge temperature, is determined by triple Langmuir probes at the vacuum vessel radius. In fact, these probes provides a good measurement of temperature with high temporal resolution, hence allow a reliable reconstruction of the outermost part of the temperature profile, where the measurements provided by the Thomson scattering diagnostic are not available. This is mandatory to estimate Ω_{diam} when r_s gets close to a.

Figure 5.9 presents an example of the temperature profile, measured by the RFX-mod Thomson scatter diagnostic, and the profile that has been extrapolated by fit.
The $m = 2$,$n = 1$ resonant radius (from magnetic equilibrium reconstruction, as described below) is highlighted by a vertical light blue line.
The ion temperature T_i, being not available for the whole tokamak discharges database, has been set to 2/3 of the electron one ($T_i \sim 2/3T_e$). This value has been estimated as an average over a large number of measurements, in the typical density range of tokamak discharges, by means of the Neutral Particle Analyzer [130].
The ion density have been instead taken equal to the electronic one, $n_i = n_e$, since only hydrogen and deuterium plasmas have been analyzed.
For both density and temperature, the profiles are reconstructed every 10ms, according to the sampling time of the relative measurements.
Although a large number of plasma shots have been studied, only in few cases reliable measurements of both temperature and density are available. In fact, RFX-mod diagnostics are optimized to operate in RFP configuration, with plasma current up to 2MA and typical density of few $10^{19}m^{-3}$. Instead, the tokamak discharges are characterized by a current smaller than 200 kA and by a density typically one order of magnitude smaller than the RFP case. Therefore, in many cases, density and temperature data do not exist or are unreliable. Moreover, for shots where measurements are both available, data may be limited to a narrow time interval.

5.2.4 Model validation

Collecting all these data, a comparison between the tearing mode frequencies predicted by (5.14) (hereafter dubbed 'modelled frequencies') and those extracted from the ISIS measurement, as described in section 5.1 (hereafter dubbed 'experimental frequencies'), has been made for both $m = 2$, $n = 1$ and $m = 3$, $n = 2$ modes.
Figure 5.10 provides an example for shot #35372. The analysis is done in

the time interval [135, 245] ms, where both electron density and temperature are available. As far as the $m = 3$, $n = 2$ mode is concerned, it is further restricted to the sub-interval [180, 245] ms, where the mode amplitude can be detected with sufficient accuracy.
Data are plotted in the negative frequency axis because the magnetic island move towards the electron diamagnetic direction, which basically means in the counter-current direction.
A good agreement is found between the experimental and modelled frequencies, for both the $m = 2$, $n = 1$ and $m = 3$, $n = 2$ modes. The colored bands represent the error estimate.
Within model (5.14), the diamagnetic term (5.16) dominates over the ion-flow contribution (5.15). Moreover, Figure 5.10a suggests that variations of the mode frequency (in this case an acceleration at about 150ms) can be ascribed to modifications of the diamagnetic term, since the time traces of diamagnetic and experimental frequencies always follow closely each other. Further evidences of this are provide in the following.
The spectrogram of the ISIS magnetic signals, showing the experimentally detected frequency, is plotted in Figure 5.11. One can appreciate that this frequency variations is not associated to any significant modification of the magnetic equilibrium, since q(a) stays almost constant.

The same analysis has been performed on a $q(a) < 2$ discharge (Figures 5.12, 5.13), condition that can be safely achieved in RFX-mod thanks to the suppression of the non-resonant $m = 2$, $n = 1$ resistive wall mode, by means of a sophisticated magnetic feedback system [131]. Therefore, the dominant mode is the $m = 3$, $n = 2$ tearing in this discharge: it appears after 100 ms with a frequency about 8 kHz (Figure 5.13), remaining almost constant up to about 375 ms. Afterwards, it rapidly slows down to few hundreds Hz, and a disruption occurs.
The comparison between the experimental and modelled frequencies is shown in Figure 5.12: a good agreement is found even in this case. As in Figure 5.10a, the variation of the mode frequency, the final slowing down in this case, is straightforwardly explained by the quenching of the diamagnetic term. Such a reduction of the diamagnetic frequency is due to a modification

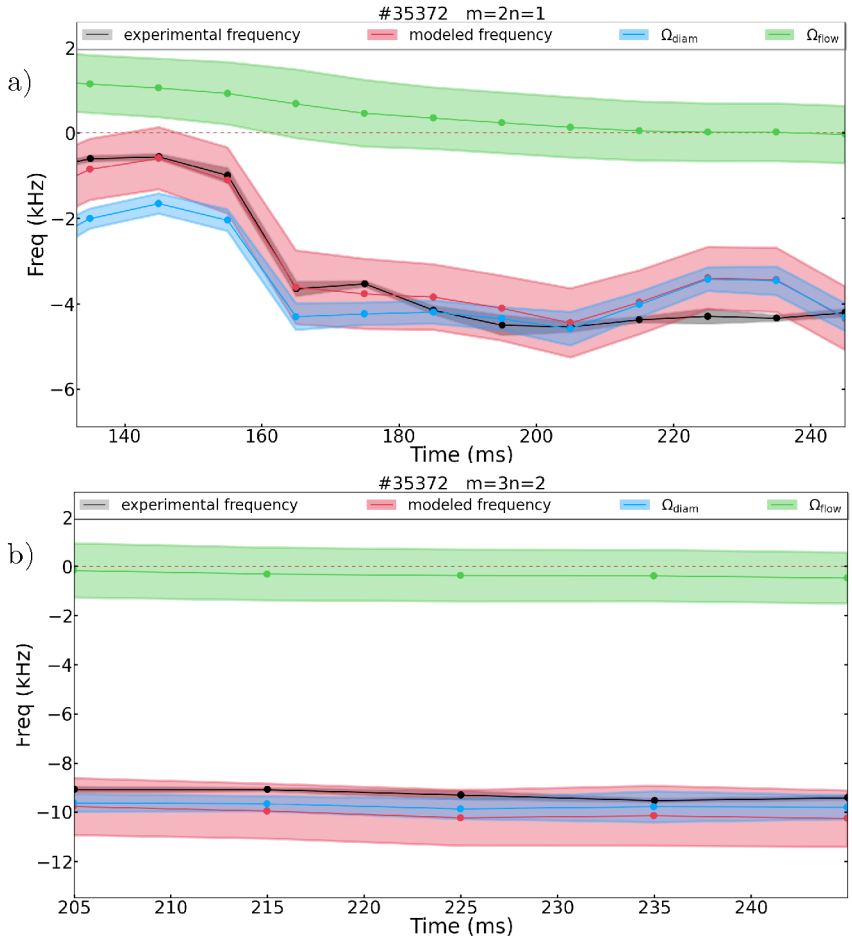

Figure 5.10: Comparison of experimental (black) TM frequency and that obtained from the model (5.14) (red). The top panel (a) refers to the $m = 2$, $n = 1$ TM, the bottom one (b) to the $m = 3$, $n = 2$ TM. The diamagnetic (blue, eq. (5.16)) and flow (green, eq. (5.15)) contributions are shown as well. The estimated error is represented by the colored bands.

mainly of the temperature profile, as the following analysis will elucidate. To this purpose, the contributions of density and temperature within the diamagnetic frequency are investigated in a more detail for the $m = 2$, $n = 1$ and $m = 3$, $n = 2$ examples, described in figures 5.10a-5.12. Let's consider the splitting

$$\Omega_{diam}(r_s, t) = CT_e \left[\frac{d(\log n_e)}{dr} + \frac{d(\log T_e)}{dr} \right] \Bigg|_{r_s} = \Omega_{diam,T_e} + \Omega_{diam,n_e} \quad (5.20)$$

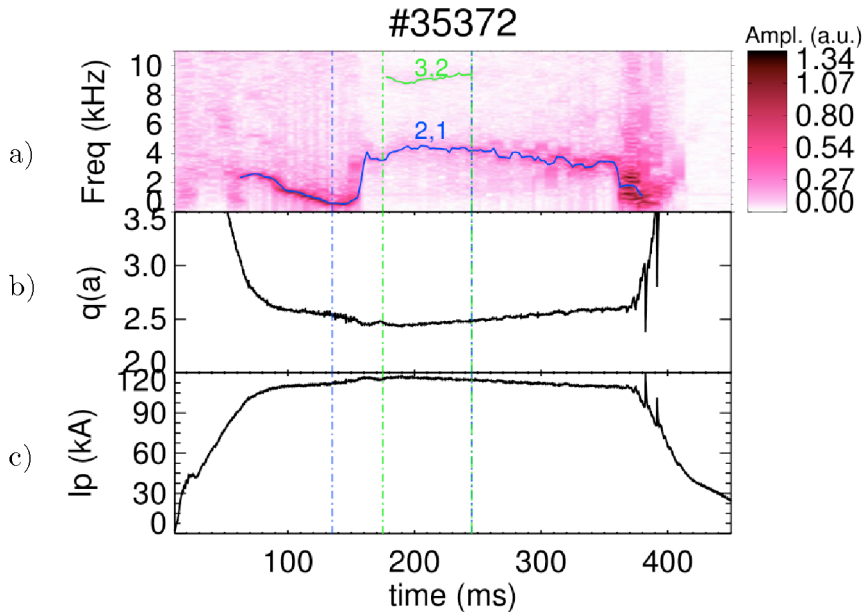

Figure 5.11: Spectrogram of ISIS magnetic fluctuation data for discharge #35372 (a). The measured $m = 2$, $n = 1$ and $m = 3$, $n = 2$ mode frequencies are highlighted. Time traces of edge cylindrical safety factor q(a) (b) and plasma current I_p (bottom panel). The vertical lines identify the time range chosen for the analysis.

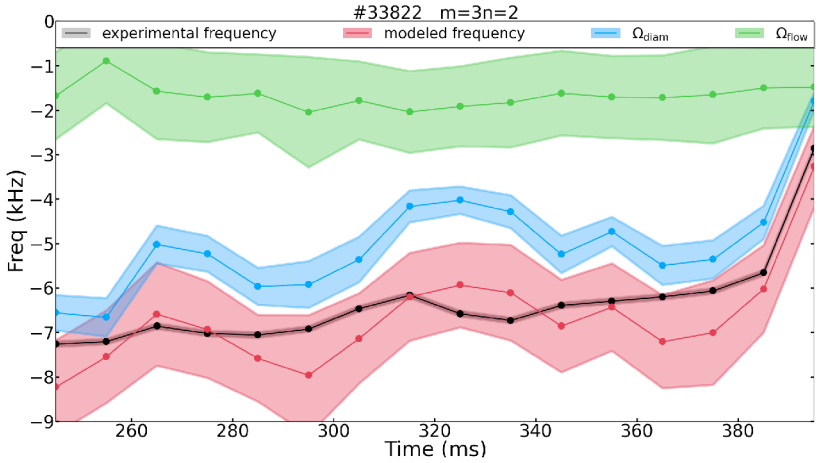

Figure 5.12: Analysis of m=3, n=2 TM frequency, with the same quantities displayed in figure 5.10.

where $\Omega_{diam,T_e} = CT_e \frac{d(\log T_e)}{dr}$ and $\Omega_{diam,n_e} = CT_e \frac{d(\log n_e)}{dr}$.
The factor $C = \frac{5}{3} \frac{m}{er_s B_\phi}$ doesn't change significantly within the examined time intervals, being related to magnetic equilibrium only ($q(a)$ is almost constant

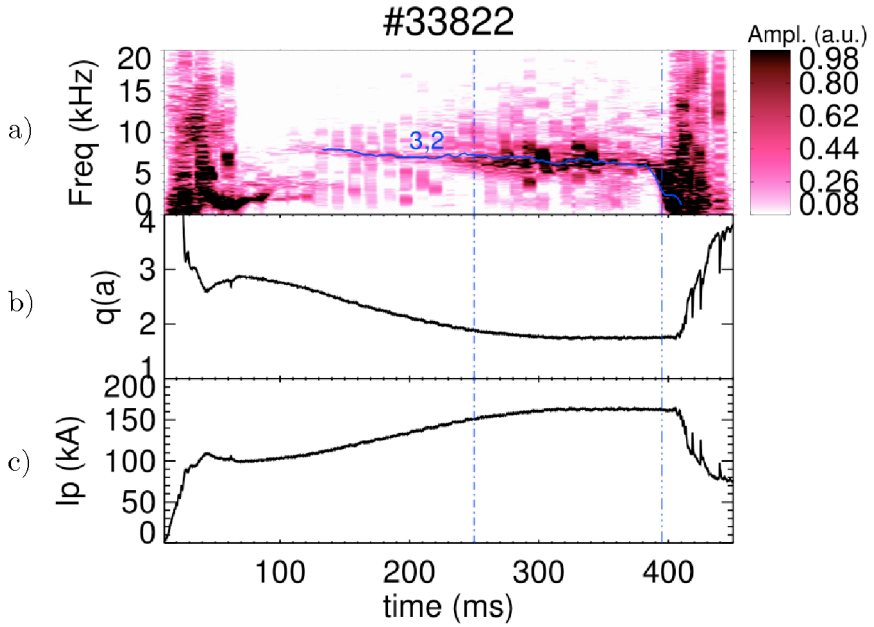

Figure 5.13: Same quantities of figure 5.11 for shot #33822 characterized by a m=3, n=2 TM.

therein; see figures 5.11, 5.13). Hence, it can be regarded as a shot-dependent coefficient. Note that Ω_{diam,T_e} depends on T_e only, whereas Ω_{diam,n_e} combines both T_e and n_e. As shown by panels (iv) of figure 5.14, Ω_{diam,T_e} is more important than Ω_{diam,n_e}. The reasons is that the normalized temperature gradient $\frac{d(\log T_e)}{dr}\Big|_{r_s}$ is larger than the normalized density gradient $\frac{d(\log n_e)}{dr}\Big|_{r_s}$, both in absolute terms and as far as the variations are concerned (see panels (ii) and (iii)). Panels (v) shows a correlation between $\frac{d(\log T_e)}{dr}\Big|_{r_s}$, $\frac{d(\log n_e)}{dr}\Big|_{r_s}$ and the 'nominal' island width: increase/decrease of W implies local flattening/peaking of T_e and n_e profiles about the resonant surface. In these two examples the variations of $T_e(r_s)$ are concordant with those of the normalized gradients and enhance the overall effect onto Ω_{diam} (see panels (i)).
The same occurs in the further $m = 2, n = 1$ example provided in figure 5.15. The full temperature profile is also provided at two time instants: note that the modifications induced on $T_e(r)$ have a global character.
The above analysis suggests a correlation between the TM fast rotation and the kinetic profiles. The results can be summarized as follows. i) in the

RFX-mod tokamak TM frequency is mostly given by the diamagnetic drift at the resonant surface, effect that should be less important in larger devices, due to the inverse dependence on the major radius and on the toroidal magnetic field; ii) this drift mainly depends on the local normalized temperature gradient; iii) this gradient is affected by the TM island through global modifications of the temperature profile. In particular, the following sequence is proposed: the *increase/decrease* of the island width induces a *flattening/peaking* of T_e, which *slows-down/spins-up* the diamagnetic drift along with the TM frequency.

It should be notice that this is not the customary interpretation of the

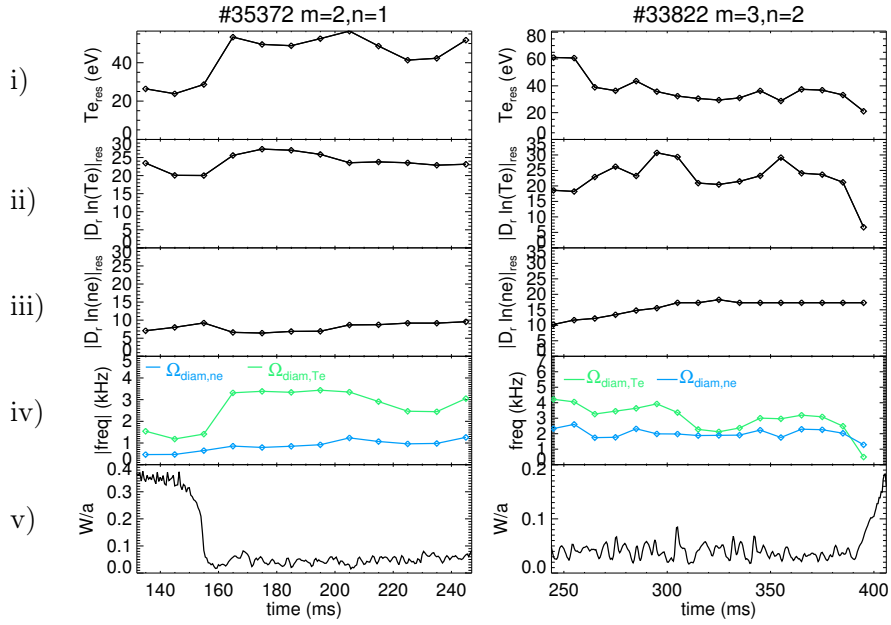

Figure 5.14: Temporal evolution of several quantities related to the diamagnetic frequency for $m = 2, n = 1$ TM in shot #35372 (left panels) and $m = 3, n = 2$ TM in shot #33822 (right panels). From top to bottom: electron temperature at the resonant radius (i), absolute value of radial derivative of $\log T_e$ ($D_r = \partial/\partial r$) (ii), absolute value of radial derivative of $\log n_e$ (iii). All these quantities are estimated at the resonant radius. The density (blue) and temperature (green) contributions to the diamagnetic frequency are shown in panel (iv). Panel (v) displays the estimated island width normalized to the minor radius.

TM frequency variations, since they are generally ascribed to the interaction with the mirror currents induced onto the vacuum-vessel, which develops an

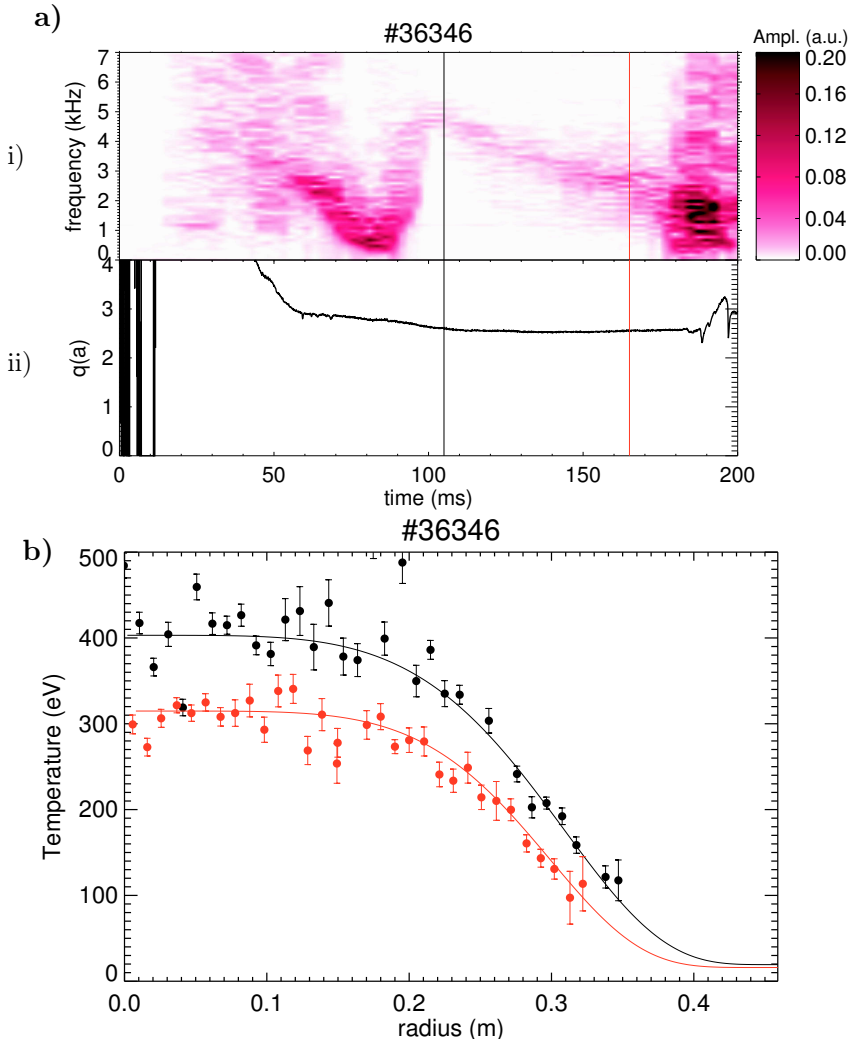

Figure 5.15: Analysis of m=2, n=1 mode in shot #36346, characterized by a long slowing down phase. Therefore, this shot is well suited to correlate the modifications of the frequency with those of the temperature profile. a) Spectrogram (i) and time trace of $q(a)$ (ii). b) T_e profile, acquired and fitted, at two different time instants (highlighted in (a) by vertical lines) corresponding to significantly different TM frequencies.

electromagnetic torque on the *ion fluid* at the resonant surface. Above a mode amplitude threshold, this causes TM rotation frequency stop in the laboratory frame (wall-locking) [116]. However, if such an effect were relevant in considered cases, the correlation between the diamagnetic frequency and the mode frequency would not be so strict. Rather, a significant modification of the ion fluid velocity, not observed, would occur. In the section

5.3, further evidences supporting the inadequacy of the above purely electromagnetic model for the present discharges are presented.

5.2.5 Sensitivity analysis on α

As anticipated at the end of paragraph 5.2.2, the poloidal angular ion velocity $\Omega_{\theta,i}(r)$, which gives a contribution to the flow component of equation (5.14), is modelled by equation 5.18: here, $\alpha = \sqrt{\frac{\tau_V}{\tau_D}}$ is an almost free parameter, being the viscous time diffusion τ_V and the poloidal flow damping characteristic time τ_D of difficult estimate.
In the flow analysis just discussed, τ_V has been taken of the order of the energy confinement time ($\tau_V \sim 60ms$). Moreover, the choise $\tau_D = \tau_V/500$

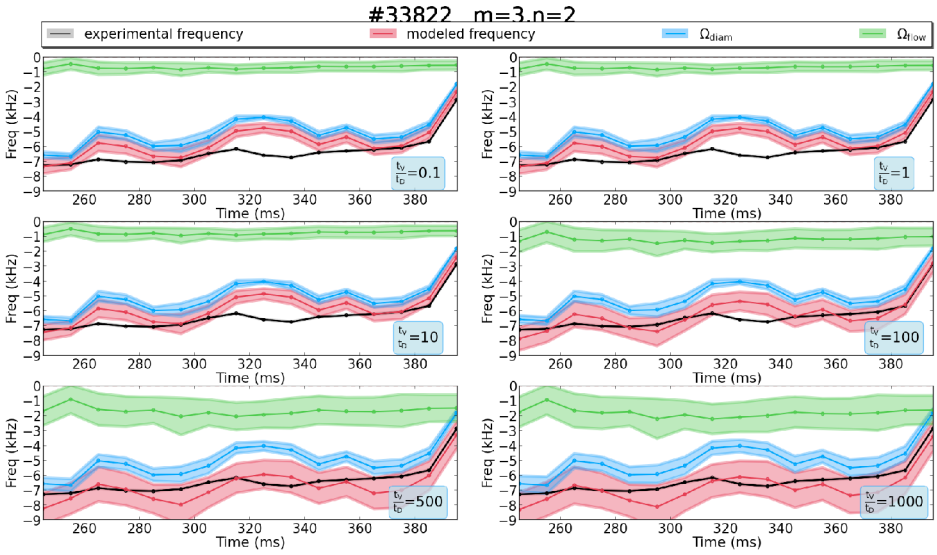

Figure 5.16: Comparison of the experimental and modeled frequencies (the latter reported with the full, diamagnetic and flow components) for 6 different values of the ratio τ_V/τ_D (see equations (5.14, 5.18)). Obviously, the ion flow component varies with α, whereas the diamagnetic one not.

has been done, in order to model a strong poloidal flow damping [29].
A sensitivity analysis has been performed in order to verify the dependence of the TM frequency model estimate on the parameter $\alpha = \sqrt{\tau_V/\tau_D}$, which enters in the modelling (5.18) of the ion poloidal angular velocity.

For the #33822 discharge, Fig. 5.16 compares the experimental frequency and the modelled one, computed with six different values of α, covering four orders of magnitudes. The dependence of the final result on this parameter is rather week, since of the ion flow component of the TM modelled frequency is dominated by the diamagnetic one. Nonetheless, the comparison with the experimental frequency suggests $\alpha = 100 - 500$ as optimum interval.

5.3 Slowing down analysis

The RFX-mod analysis just presented links the dynamic of TM fast rotation to that of the kinetic profiles, temperature in particular. In this case, the electromagnetic interaction with the mirror currents induced onto the passive conductive structures should be a secondary effect. In this section, a more quantitative assessment of this statement is provided, showing that the electromagnetic torque model does not fit the pre-disruptive TM slowing down phase. Let's consider the $m = 2$, $n = 1$, which benefits from data better than those of the $m = 3$, $n = 2$. The frequencies (from ISIS measurement), taken from the database displayed in figures (5.8, 5.7) are plotted as a function of time in Figure 5.17a: most of the initial values, before the slowing down, stand between $4 \div 5$ kHz. Therefore, we take these frequencies unaltered, without applying any normalization.
In Figure 5.17b the normalized island width is plotted against these frequencies. Note a continuous slowing down as the mode amplitude increase, roughly fitted by a logarithmic function (blue continuous line). The further fit (red dotted line) wants to assess the compatibility of the present data with the electromagnetic braking model. Now this fit is described. Modelling the vacuum vessel as a single thin shell with global time-constant τ_{vess}, denoting E_{vess} the normalized derivative discontinuity of $\psi_{m,n}$ across the vessel, defined as in section 2.2, and taking the outermost copper shell to be ideal, this theory predicts the following relationship between the mode frequency

and the island width [116]:

$$C\left(\frac{W}{a}\right)^4 \frac{2\pi f \tau_{vess}}{(2\pi f \tau_{vess})^2 + E_{vess}^2} = f_0 - f \tag{5.21}$$

The constant C incorporates the viscosity and the poloidal flow damping time, whereas f_0 is the mode frequency for $W/a \ll 1$. Therefore, by inverting (5.21), in order to express W/a as function of the frequency, the following interpolating function of the data displayed in Figure 5.17b is tried:

$$y = m_1 \times \left\{ |m_4 - x| \times \left[(2\pi x \tau_{vess})^2 + m_2^2 \right] / (2\pi x \tau_{vess}) \right\}^{1/4} + |m_3| \tag{5.22}$$

In this expression x is in kHz and τ_{vess} in ms. The coefficients of the fit are

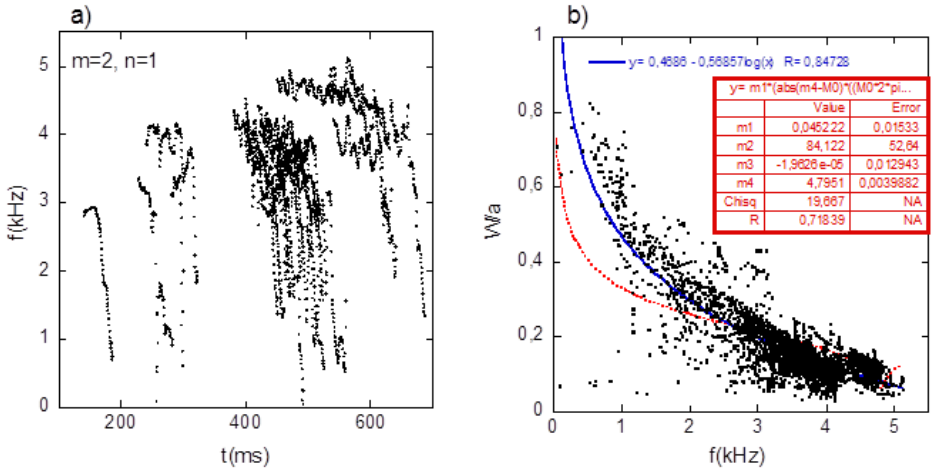

Figure 5.17: Slowing down analysis for the $m = 2$, $n = 1$ TM. a) Frequencies (from ISIS measurements) vs time. b) Island width vs frequencies: blue line is a logarithmic fit, whereas red dashed line is the fit (5.22).

denoted m_i, with $i = 1, ..., 4$. In particular, m_4 gives an estimate of f_0 and m_2 of E_{vess}. In order to make the fit viable, two changes has been made with respect to (5.21): the difference $f_0 - f$ is taken in absolute value, and an offset $|m3|$, expected to be small, is added. There is little sensitivity of the result on τ_{vess}: here it is fixed at 1.5ms. The fit made with (5.22) is rather bad, as can be seen in Figure 5.17b. Moreover, while m_4 turns out to be in the expected range, m_2 is quite larger than the estimate $|E_{vess}| \sim 18$ from

Newcomb's equation.
The conclusion, as anticipated before, is that the purely electromagnetic model cannot describe the slowing down of the $m = 2$, $n = 1$ tearing mode in the RFX-mod discharges. This statement is applied to the fast rotation only and it does not imply that TMs do not interact with the passive or active conductive structures in RFX-mod. In fact, for $q(a) < 2.5$ the $m = 2$, $n = 1$ induced disruptions follows a wall-locking, in the absence of magnetic feedback (see figure 5 of [29]). The latter, instead, prevents the true wall-locking, keeping TM into slow rotation (some tens Hz), thereby avoiding the disruption [29, 132].

5.4 Limit-cycle analysis

In this section, the experimental observation of quasi-periodic oscillations of the TM frequency and amplitude, particularly evident when the average density raises up to few $10^{19}m^{-3}$, are presented.
An example of a such a behavior is shown in Figure 5.18, where the spectrogram of the $m = 2$ magnetic fluctuation component is shown, together with the time evolution of plasma current, edge safety factor, electron density and the ratio of the latter to the Greenwald density for the RFX-mod #29757 tokamak discharge.
As can be seen, after $t \simeq 210$ ms, the $m = 2$, $n = 1$ TM is characterized by a propagation frequency of about 4.5 kHz, while the density raises. At time $t \simeq 300$ ms the spectrogram shows that the spectrum changes, exhibiting oscillations both in frequency and amplitude. This oscillatory behavior quickly ceases when the electron density collapses rapidly down to few $10^{18}m^{-3}$. This rapid variation of density is accomplished by a TM frequency variation, likely to be a consequence of a global equilibrium change. The amplitude and frequency analysis was performed in the time window [210,440] ms. Their time traces are presented in Figure 5.19, alongside the normalized density (line-averaged density/Greenwald value) and the poloidal component of the TM magnetic field. In the time interval [210-280] ms, both amplitude and frequency are quite constant. Starting from about 280 ms, frequency, amplitude

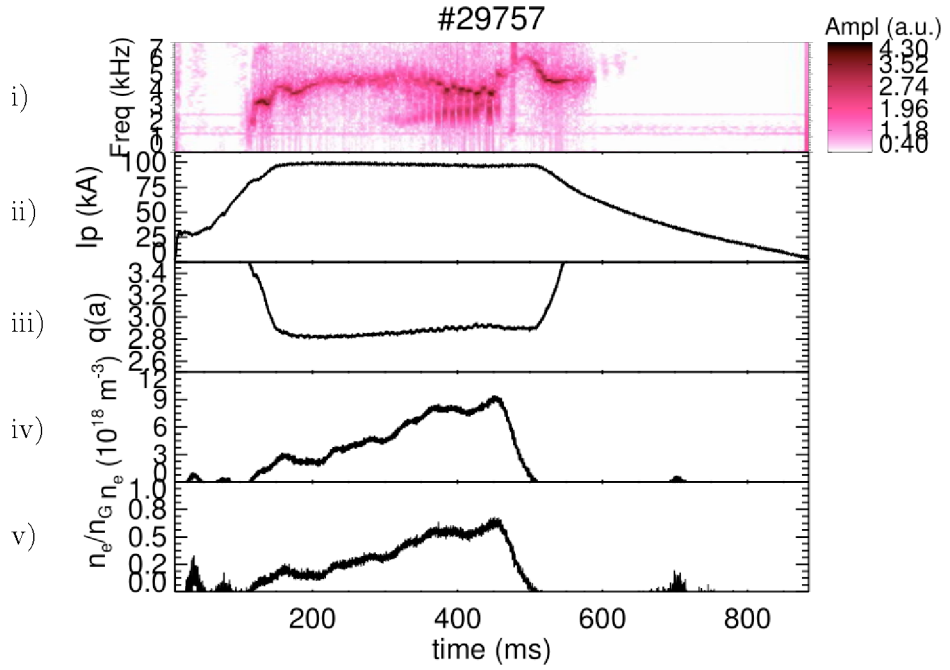

Figure 5.18: Time evolution of several parameters for #29757 discharge. From top to bottom: spectrogram of $m = 2$ poloidal magnetic field component (i), plasma current (ii), edge safety factor (iii), electron density (iv), electron density ratio to the Greenwald density (v).

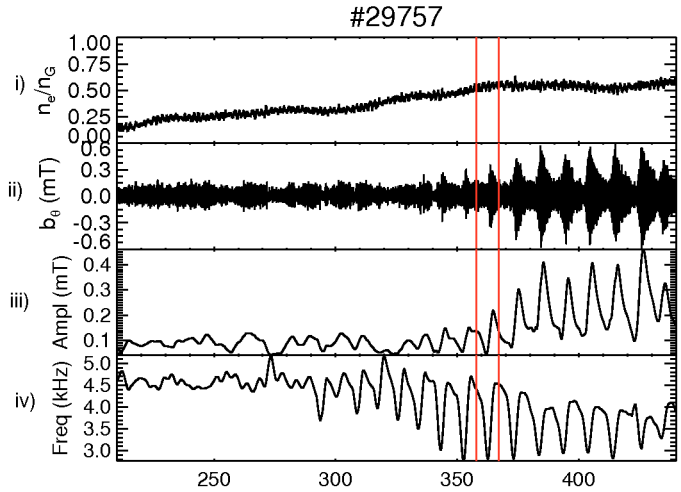

Figure 5.19: Time traces of some parameters of $m = 2$, $n = 1$ TM for #29757 discharge. From top to bottom: normalized density (i), poloidal magnetic field (ii), amplitude (iii) and frequency (iv). Red vertical lines identify the time interval chosen for a single cycle analysis.

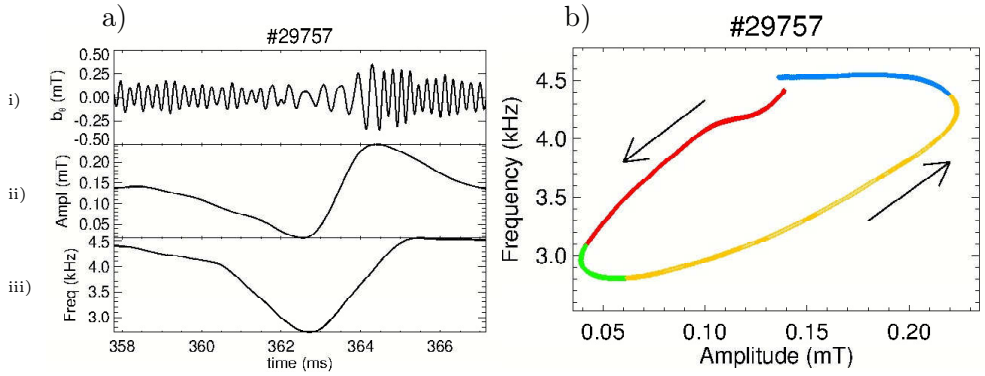

Figure 5.20: a) Time traces of TM parameters in the time interval 358:368 ms. From top to bottom: poloidal magnetic field (i), amplitude (ii) and frequency (iii). b) Mode evolution on the amplitude-frequency plane. Two arrows indicate the direction rotation. Colors refer to different time intervals.

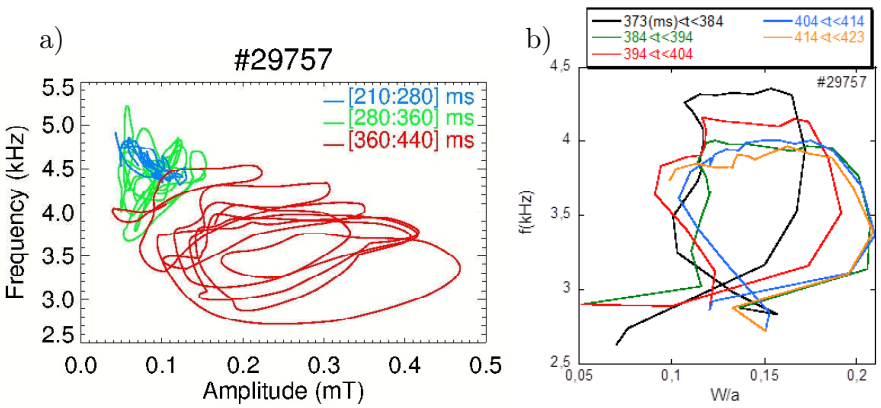

Figure 5.21: a) Mode evolution in the amplitude-frequency plane. Three main phases are highlighted. In the first one (blue line) there is no appreciable swinging, in the second oscillations are small and irregular, in the last phase, oscillations are wide and quite regular. b) mode oscillations in the island width-frequency plane. Only 5 cycles in the time interval [373-423] ms are reported.

and magnetic field signals exhibit quasi-periodic oscillations that increase until a sort of saturation of the amplitude peaks occurs, at about $t \simeq 400$ ms. In this time interval [210-400] ms, the electron density raises linearly up to an almost constant flat-top value.

To get more in detail, the same quantities are presented in Figure 5.20a for a single oscillation cycle, identified by two vertical lines shown in the previous picture, while Figure 5.20b shows the time evolution of the MHD mode on the amplitude-frequency plane for the same cycle. A cyclic path of the mode

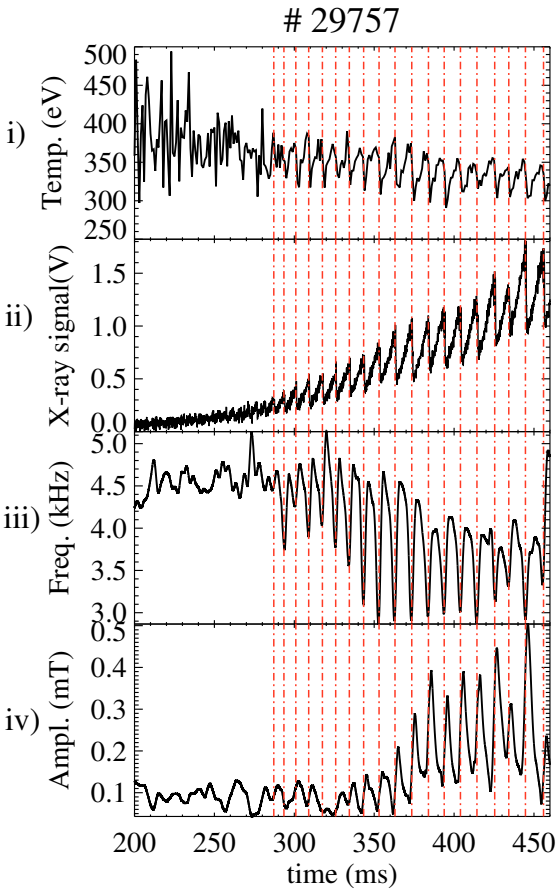

Figure 5.22: Data from #29757 discharge. From top to bottom: electron temperature (i), central chord soft X-ray flux (ii), $m = 2$, $n = 1$ estimated frequency (iii) and amplitude (iv). Vertical lines indicate the recognized X-ray signal crash instants. A clear correlation between temperature and X-ray crashes with the amplitude and frequency swinging can be seen.

evolution is observed and the colors identify different stages of the cycle (red: frequency decreases, amplitude decreases; green: frequency almost constant, amplitude rises, yellow: both frequency and amplitude grow; blue: frequency almost constant, amplitude decreases). This phenomenon has been already observed in FTU [133], and it has been dubbed as *limit cycle*.

It is interesting to note that, in the case here presented, the rotation direction in the frequency-amplitude plane is opposite with respect to that

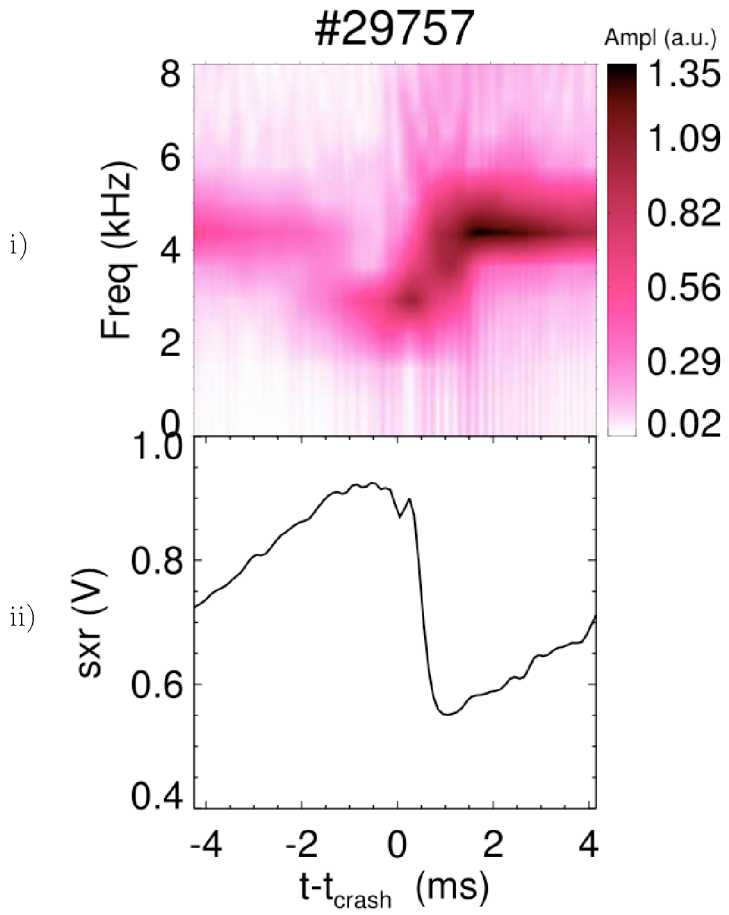

Figure 5.23: Spectrogram of the $m = 2$ component (i) and time trace of the sxr signal (ii). These quantites have been calculated by averaging different time intervals centered on sawtooth crash events

observed in FTU plasmas.

A similar graph (Figure 5.21a) shows the evolution in the whole time interval [210,440] ms. It is possible to notice that in a first stage, highlighted by a blue line, there are not appreciable oscillations; then, in a second stage, amplitude and frequency oscillate quite irregularly in the amplitude/frequency plane; finally, the width of amplitude and frequency oscillations increases, with almost regular cycles. In this last stage, the average frequency is reduced of about 1 kHz.

Figure 5.21b shows the cycles in the plane island-width/frequency. In this figure, only 5 cycles between 373 ms and 422 ms are reported, corresponding

to a "stationary phase", this is probably why, in this plane, the cycles seem even more regular and reproducible.

Role of sawtooth activity

It is possible to observe that the limit cycle period is coincident with the interval between two subsequent crashes of soft X-ray flux (central chord) and electron temperature signals, as shown in figure 5.22. The recurrent crashes that characterized these signals are a clear evidence of $m = 1$, $n = 1$ sawtooth activity.
The relationship between sawtooth activity and the oscillations of TM amplitude and frequency becomes further evident in figure 5.23, where the spectrogram of the m=2 magnetic fluctuation component and the time evolution of the soft x-ray signal are shown. These quantities have been obtained averaging different time intervals centered on a crash event, in the time window [320,430] ms.
This observation could mean that the limit cycle is likely to be due to a coupling between the $m = 2$, $n = 1$ TM and the internal resonant $m = 1$, $n = 1$ mode.
These graphs show that the limit cycle oscillation takes place in a short interval, of about 3/4 ms, around the sawtooth crash time. Being the characteristic oscillation period of amplitude and frequency shorter than that of the temperature sampling, we are not able to compare the frequency variation with the diamagnetic term on that time scale.
Further analysis will be carried out to better investigate the role of the saw tooth and the dependence on plasma density

5.5 Conclusions

In conclusion, it has been shown, by comparison of the experimentally observed frequencies and those predicted by a two-fluid MHD model, that the diamagnetic drift represents the dominant contribution to the TM rotation velocity, if compared with the ion flow drift. This indication could be useful

for the future fusion machines, like ITER, in which a low ion flow velocity is expected. It has seen also that the TM slowing down, a phenomenon that, in most cases, lead to the plasma disruption, can be associated to the growth of TM islands, which modify the diamagnetic profiles. Instead, a purely electromagnetic model, describing the interaction between the island and the external conductive structures, results insufficient to explain this TM breaking.
The observation of quasi-periodic oscillation of the TM in the amplitude-frequency plane, dubbed as "limit cycle", has been described. This characteristic dynamics is related, in the analyzed tokamak discharges, to the sawtooth activity at the plasma core. A possible coupling of the $m = 2, n = 1$ TM to the most internal $m = 1, n = 1$ mode has been proposed.

Appendix

Equation (5.8) arises from the following approximation, which can be applied fairly well either to a high-frequency $m = 2$, $n = 1$ or $m = 3$, $n = 2$ mode, screened by the vacuum vessel, in the region $r \geq r_s$:

$$|\psi^{m,n}| = |\psi_s| \left(1 - \frac{x}{x_w}\right) \ , \qquad x = (r - r_s)/r_s \geq 0 \ , \qquad x_w = (r_w - r_s)/r_s \tag{A1}$$

Let's consider the cylindrical, helical formalism described in [134]: every quantity depends on r and the helical angle $u = m\theta - n\phi$. Denoting by χ the helical flux, which is a real quantity, standard relations are:

$$r b_r = \frac{\partial \chi}{\partial u} \tag{A2}$$

$$r\, \mathbf{B} \cdot \nabla u = m B_\theta - n \frac{r}{R} B_\phi = -\frac{\partial \chi}{\partial r} \tag{A3}$$

We also assume the expansion $\chi(r, u) = \chi_0(r) + \chi_1(r) cos(u)$. In this case equations (5.1) and (A2) are conciliated by taking $\chi_1 = |\psi^{m,n}|$ and including in $\psi^{m,n}$ a factor 2, which encapsulates the complex conjugate harmonic's

(i.e. $-m$,$-n$) contribution. Hence, $\chi_1(r_s) = |\psi_s|$. As far as the zeroth-order component is concerned, (A3) becomes

$$-\frac{\partial \chi_0}{\partial r} = mB_{\theta 0} - n\frac{r}{R}B_{\phi 0} = F_0(r) \tag{A4}$$

For the $m = 2$, $n = 1$ mode of a tokamak equilibrium, F_0 can be well approximated by a linear decreasing function, hence χ_0 by a parabolic function, in the region beyond the resonant surface:

$$F_0(r) \cong F'_{0s}\, r_s\, x \quad \rightarrow \quad \chi_0 \cong -\frac{1}{2}F'_{0s}\, r_s^2\, x^2 \ , \quad x \geq 0 \ , \quad F'_{0s} \equiv F'_0(r_s) < 0 \tag{A5}$$

A magnetic surface identified by $\chi(r,u) = \chi_0(r) + \chi_1(r)cos(u) = \overline{\chi}$ is described by a parametric equation for $x(u)$, obtained from (A1), (A5):

$$x^2 - \left(\frac{\xi}{x_w}cosu\right)x + \xi cosu + C = 0 \ , \quad \xi = \frac{2\chi_1(r_s)}{r_s^2|F'_{0s}|} = \frac{W^2}{8r_s^2} \ , \quad C = -\frac{2\overline{\chi}}{r_s^2|F'_{0s}|} \tag{A6}$$

Use has been made of definition (5.7). Note that ξ is a small positive parameter. The approximations leading to (A6), valid for $x \geq 0$, still holds for $x < 0$, but not too far from the resonant surface. The discriminant of (A6) is $\Delta(u,C)/4 = -\xi cosu\left[1 - \frac{\xi}{4x_w^2}cosu\right] - C = \Delta(u,0)/4 - C$. Given the smallness of ξ, we can take the term in parenthesis to be positive. Hence, $\Delta(u,0)$ is monotonically increasing from $u = 0$ to $u = \pi$, and then monotonically decreasing up to $u = 2\pi$. Therefore, for $C < \Delta(0,0)/4 = -\xi\left[1 - \frac{\xi}{4x_w^2}\right]$ two real solutions of x are given at any u: this is the region outside the magnetic island. Instead, for $\Delta(0,0)/4 < C < \Delta(\pi,0)/4 = \xi\left[1 + \frac{\xi}{4x_w^2}\right]$ two real solutions of x are given only within the intervals $u_C < u < 2\pi - u_C$, being $\Delta(u_C,C) = 0$: this is the region of the magnetic island. The island separatrix is identified by $C = \Delta(0,0)/4 = -\xi\left[1 - \frac{\xi}{4x_w^2}\right]$: here, the maximum x, attained at $u = \pi$, is

$$max[x]_{separatrix} = \frac{1}{2}\left(\frac{W}{r_s} - \frac{\xi}{x_w}\right) \tag{A7}$$

Using the x and ξ definitions within A7, formula (5.8) is finally obtained.

Chapter 6

Conclusions

Magnetic reconnection is the process that cause the variation of the magnetic field topology. In this process, the conversion of magnetic into kinetic energy occurs. It takes place everywhere in the Universe, being observed both in astrophysical and laboratory plasmas.
Throughout this thesis, it has been shown that magnetic reconnection, although acting in a localized region of plasma, characterized by enhanced resistivity, is able to strongly influence the magnetic and particle fields of the whole plasma system.
A characterization of the magnetic reconnection phenomena taking place in the RFX-mod plasma discharges, by means of in-vessel magnetic and electrostatic measurements, has been presented.
It has been shown how magnetic reconnection phenomena in RFP plasmas are associated to the formation of toroidally localized current sheets, which are naturally subject to fragmentation. This process is found to be compatible with those deduced from modelling and experimental observations of astrophysical plasmas. Such fragmentation seems to be associated with the efficient acceleration of charged particles in plasma, which is indeed found to be coupled to enhancement of the temperature and fusion reactivity. The latter is deduced by time-resolved measurement of the neutron fluxes.
These evidences thus show how reconnection can contribute to plasma heating in the RFP configuration. Furthermore, the evidence of current sheet

fragmentation and high Lundquist plasmas produced in RFX-mod, induce to believe that such a machine could be a useful device for the study of collisionless magnetic reconnection, and a natural laboratory to test the evolution of the plasmoid instabilities.

A particular attention has been dedicated to the study of tearing modes (TMs) in the circular tokamak discharges of RFX-mod. TMs, being associated to the formation of magnetic islands through magnetic reconnection, reduce magnetic confinement. Their study is an essential issue in order to achieve high performances in future fusion reactors.

The study of TMs in the RFX-mod plasma has integrated analysis of magnetic, flow and kinetic measurements. In particular, the diamagnetic drift component of the rotation frequency has been investigated.

In this work, it has been shown, by comparison of the experimentally observed frequencies and those predicted by a two-fluid MHD model, that the diamagnetic drift represents the dominant contribution to the TM rotation velocity, if compared with the ion flow drift.

It has also shown that a purely electromagnetic model, describing the interaction of the TM with the currents induced at the conductive structures encircling the plasma, is not sufficient to explain the rotation slowing down, a phenomenon, observed in conjunction with the TM amplitude increases, leading sometimes to the wall-locking and the rapid termination of the discharge (disruption). Instead, indications that the this dynamic is related to mode-island-induced modifications of the kinetic profiles (mainly temperature), which determine the diamagnetic drift, are provided.

Lastly, the characteristic oscillations of frequency and amplitude of TM in tokamak plasmas, known as 'limit cycle', have been presented. The role of the sawtooth activity in such a phenomenon has been also characterized. The coupling of the $m = 2, n = 1$ to the $m = 1, n = 1$ internal mode has been proposed as a possible mechanism of such a limit-cycle effect.

Bibliography

[1] J. M. Griffin. *Global climate change: the science, economics and politics*, volume 4. Edward Elgar Publishing, 2003.

[2] International Energy Agengy. Energy technology perspectives, scenarios & strategies to 2050. `https://www.iea.org/publications/freepublications`.

[3] L. Antilla. Climate of scepticism: Us newspaper coverage of the science of climate change. *Global environmental change*, 15(4):338–352, 2005.

[4] W. Poortinga, A. Spence, L. Whitmarsh, S. Capstick, and N. F. Pidgeon. Uncertain climate: An investigation into public scepticism about anthropogenic climate change. *Global environmental change*, 21(3):1015–1024, 2011.

[5] C. Rosenzweig, D. Karoly, M. Vicarelli, P. Neofotis, Q. Wu, G. Casassa, A. Menzel, T. L. Root, N. Estrella, B. Seguin, et al. Attributing physical and biological impacts to anthropogenic climate change. *Nature*, 453(7193):353, 2008.

[6] C. Marius Braams and P. E. Stott. *Nuclear fusion: half a century of magnetic confinement fusion research*. CRC Press, 2002.

[7] J. Wesson and D.J. Campbell. *Tokamaks*. International Series of Monographs on Physics. OUP Oxford, 2011.

[8] M. Kikuchi. *Frontiers in fusion research: physics and fusion*. Springer Science & Business Media, 2011.

[9] J. P. Freidberg. *Plasma physics and fusion energy*. Cambridge university press, 2008.

[10] S. Pfalzner. *An introduction to inertial confinement fusion*. CRC Press, 2006.

[11] T. J. Dolan. *Fusion research*. 1982.

[12] W. M. Stacey. *Fusion plasma physics*. John Wiley & Sons, 2008.

[13] V. Igochine. *Magneto-Hydrodynamics and Operational Limits*, pages 9–51. Springer Berlin Heidelberg, Berlin, Heidelberg, 2015.

[14] H. Zohm. *Introduction to Tokamak Operational Scenarios*, pages 1–7. Springer Berlin Heidelberg, Berlin, Heidelberg, 2015.

[15] C. Chiuderi and M. Velli. *Fisica del Plasma: Fondamenti e applicazioni astrofisiche*. Springer Science & Business Media, 2012.

[16] G. Spizzo, G. Pucella, O. Tudisco, M. Zuin, M. Agostini, E. Alessi, F. Auriemma, W. Bin, P. Buratti, L. Carraro, R. Cavazzana, G. Ciaccio, G. De Masi, B. Esposito, C. Galperti, S. Garavaglia, G. Granucci, M. Marinucci, L. Marrelli, E. Martines, C. Mazzotta, D. Minelli, A. Moro, M.E. Puiatti, P. Scarin, C. Sozzi, M. Spolaore, O. Schmitz, N. Vianello, and R.B. White. Density limit studies in the tokamak and the reversed-field pinch. *Nuclear Fusion*, 55(4):043007, 2015.

[17] D.A. Gates, L. Delgado-Aparicio, and R.B. White. Physics of radiation-driven islands near the tokamak density limit. *Nuclear Fusion*, 53(6):063008, 2013.

[18] P. Zanca, F. Sattin, D.F. Escande, G. Pucella, and O. Tudisco. A unified model of density limit in fusion plasmas. *Nuclear Fusion*, 57(5):056010, 2017.

[19] P. Zanca, L. Marrelli, R. Paccagnella, A. Soppelsa, M. Baruzzo, T. Bolzonella, G. Marchiori, P. Martin, and P. Piovesan. Feedback control

model of the m= 2, n= 1 resistive wall mode in a circular plasma. *Plasma Physics and Controlled Fusion*, 54(9):094004, 2012.

[20] P. Piovesan, M. J. Hanson, P. Martin, G. Navratil, F. Turco, J. Bialek, M. N. Ferraro, J. R. La Haye, M. Lanctot, M. Okabayashi, C. Paz-Soldan, J. E. Strait, D. A. Turnbull, P. Zanca, M. Baruzzo, T. Bolzonella, W. A. Hyatt, L. G. Jackson, L. Marrelli, and D. Shiraki. Tokamak operation with safety factor q(95) < 2 via control of MHD stability. 113:045003, 07 2014.

[21] R. Paccagnella. Tokamak operation at low q and scaling toward a fusion machine. *ArXiv e-prints*, June 2012.

[22] K. Miyamoto. *Reversed Field Pinch*, pages 389–402. Springer Berlin Heidelberg, Berlin, Heidelberg, 2016.

[23] S. Ortolani and D. D. Schnack. *Magnetohydrodynamics of plasma relaxation*. World Scientific, 1993.

[24] J. K. Anderson, T. M. Biewer, C. B. Forest, R. O'Connell, S. C. Prager, and J. S. Sarff. Dynamo-free plasma in the reversed field pinch. *Physics of Plasmas*, 11(5):L9–L12, 2004.

[25] H. Ji, A. F. Almagri, S. C. Prager, and J. S. Sarff. Time-resolved observation of discrete and continuous magnetohydrodynamic dynamo in the reversed-field pinch edge. *Physical review letters*, 73(5):668, 1994.

[26] S. Cappello and D. F. Escande. Bifurcation in viscoresistive mhd: The hartmann number and the reversed field pinch. *Phys. Rev. Lett.*, 85:3838–3841, Oct 2000.

[27] R. Lorenzini, E. Martines, P. Piovesan, D. Terranova, P. Zanca, M. Zuin, A. Alfier, D. Bonfiglio, F. Bonomo, A. Canton, et al. Self-organized helical equilibria as a new paradigm for ohmically heated fusion plasmas. *Nature Physics*, 5(8):570, 2009.

[28] P. Sonato, G. Chitarin, P. Zaccaria, F. Gnesotto, S. Ortolani, A. Buffa, M. Bagatin, W.R. Baker, S. Dal Bello, P. Fiorentin, L. Grando, G. Marchiori, D. Marcuzzi, A. Masiello, S. Peruzzo, N. Pomaro, and G. Serianni. Machine modification for active mhd control in rfx. *Fusion Engineering and Design*, 66(Supplement C):161 – 168, 2003. 22nd Symposium on Fusion Technology.

[29] P. Zanca, R. Paccagnella, C. Finotti, A. Fassina, G. Manduchi, R. Cavazzana, P. Franz, C. Piron, and L. Piron. An active feedback recovery technique from disruption events induced by m=2, n=1 tearing modes in ohmically heated tokamak plasmas. *Nuclear Fusion*, 55(4):043020, 2015.

[30] S. Barison, A. Canton, S. Dal Bello, S. Fiameni, P. Innocente, A. Alfier, S. Munaretto, and F. Rossetto. Analysis of the interaction between plasmas and the graphite first wall in RFX-mod. *Journal of Nuclear Materials*, 415(1):S274–S277, 2011.

[31] M et al. Zuin. Overview of the rfx-mod fusion science activity. *Nuclear Fusion*, 57(10):102012, 2017.

[32] G. Serianni, T. Bolzonella, R. Cavazzana, G. Marchiori, N. Pomaro, L. Lotto, M. Monari, and C. Taliercio. Development, tests, and data acquisition of the integrated system of internal sensors for RFX. *Review of Scientific Instruments*, 75(10):4338–4340, 2004.

[33] Noah Hershkowitz. 3 - How Langmuir probes work. In O. Auciello and D. L. Flamm, editors, *Plasma Diagnostics*, pages 113 – 183. Academic Press, 1989.

[34] S. Spagnolo. High frequency magnetic activities in a Reversed-field Pinch plasma, Ph.D. thesis, January University of Padova, 2012.

[35] G. Serianni, W. Baker, and S. Dal Bello. High-spatial resolution edge electrostatic probe system for RFX. *Review of Scientific Instruments*, 74(3):1558–1562, 2003.

[36] T. Bolzonella, N. Pomaro, G. Serianni, and D. Marcuzzi. New wide bandwidth in-vessel magnetic measurement system for RFX. *Review of Scientific Instruments*, 74(3):1554–1557, 2003.

[37] EJ-301 Liquid scintillator. Datasheet. `http://lartpc-docdb.fnal.gov/cgi-bin/RetrieveFile?docid=708&filename=EJ301%20data%20sheet.pdf&version=1`.

[38] H8500 Photocathode. Instrument datasheet. `https://www.hamamatsu.com/resources/pdf/etd/H8500_H10966_TPMH1327E.pdf`.

[39] G. F. Knoll. *Radiation detection and measurement*. John Wiley & Sons, 2010.

[40] D. Rapp and W. E. Francis. Charge exchange between gaseous ions and atoms. *The Journal of Chemical Physics*, 37(11):2631–2645, 1962.

[41] I. H. Hutchinson. *Principles of Plasma Diagnostics*. Cambridge University Press, 2 edition, 2002.

[42] A. Alfier and R. Pasqualotto. New thomson scattering diagnostic on RFX-mod. *Review of Scientific Instruments*, 78(1):013505, 2007.

[43] A. Fassina, M. Gobbin, S. Spagnolo, P. Franz, and D. Terranova. Characterization of small thermal structures in RFX-mod electron temperature profiles. *Plasma Physics and Controlled Fusion*, 58(5):055017, 2016.

[44] P. Innocente, S. Martini, A. Canton, and L. Tasinato. Upgrade of the RFX CO2 interferometer using in-vessel optics for extended edge resolution. *Review of Scientific Instruments*, 68(1):694–697, 1997.

[45] F. Auriemma, R. Lorenzini, M. Agostini, L. Carraro, G. De Masi, A. Fassina, M. Gobbin, E. Martines, P. Innocente, P. Scarin, et al. Characterization of particle confinement properties in RFX-mod at a high plasma current. *Nuclear Fusion*, 55(4):043010, 2015.

[46] P. Franz, L. Marrelli, A. Murari, G. Spizzo, and P. Martin. Soft x ray tomographic imaging in the RFX reversed field pinch. *Nuclear fusion*, 41:695–709, 2001.

[47] Walter Rudin. *Real and complex analysis*. Tata McGraw-Hill Education, 1987.

[48] J. W. Cooley and J. W. Tukey. An algorithm for the machine calculation of complex Fourier series. *Mathematics of computation*, 19(90):297–301, 1965.

[49] M. Fedotenkova, P. B. Graben, J. Sleigh, and A. Hutt. Time-frequency representations as phase space reconstruction in recurrence symbolic analysis. In *ITISE*, 2016.

[50] M. Farge. Wavelet transforms and their applications to turbulence. *Annual review of fluid mechanics*, 24(1):395–458, 1992.

[51] J. C. Van den Berg. *Wavelets in physics*. Cambridge University Press, 2004.

[52] N. Vianello. *Fenomeni di auto organizzazione e generazione di strutture coerenti indotte da turbolenza elettrostatica in plasmi magnetizzati*, Ph.D. thesis 2002.

[53] Martin Storath, Laurent Demaret, and Peter Massopust. Signal analysis based on complex wavelet signs. *Applied and Computational Harmonic Analysis*, 2015.

[54] E. Priest and T. Forbes. Magnetic reconnection: Mhd theory and applications. *Cambridge Univ Press, Cambridge*, 2000.

[55] D. Biskamp. *Magnetic reconnection in plasmas*. Number 3. Cambridge University Press, 2005.

[56] E. G. Zweibel and M. Yamada. Perspectives on magnetic reconnection. In *Proc. R. Soc. A*, volume 472, page 20160479. The Royal Society, 2016.

[57] M. Yamada, R. Kulsrud, and H. Ji. Magnetic reconnection. *Reviews of Modern Physics*, 82(1):603, 2010.

[58] H. Karttunen, P. Kröger, H. Oja, M. Poutanen, and K. J. Donner. *Fundamental Astronomy*. Springer Science & Business Media, 2007.

[59] E. G. Zweibel and M. Yamada. Magnetic reconnection in astrophysical and laboratory plasmas. *Annual review of astronomy and astrophysics*, 47:291–332, 2009.

[60] R. G. Giovanelli. A Theory of Chromospheric Flares. *Nature*, 158:81–82, July 1946.

[61] F. Hoyle. Magnetic storms and aurorae. *Some Recent Researches in Solar Physics*, pages 92–102, 1949.

[62] J.W. Dungey. Conditions for the occurrence of electrical discharges in astrophysical systems. *The London, Edinburgh, and Dublin Philosophical Magazine and Journal of Science*, 44(354):725–738, 1953.

[63] M. Yamada, J. Yoo, and C. E. Myers. Understanding the dynamics and energetics of magnetic reconnection in a laboratory plasma: Review of recent progress on selected fronts. *Physics of Plasmas*, 23(5):055402, 2016.

[64] R. J. Goldston and P. H. Rutherford. *Introduction to plasma physics*. CRC Press, 1995.

[65] Nasa archive. `https://www.nasa.gov`.

[66] G. S. Vaiana, L. Van Speybroeck, M. V. Zombeck, A. S. Krieger, J. K. Silk, and A. Timothy. The S-054 x-ray telescope experiment on Skylab. *Space Science Instrumentation*, 3:19–76, 1977.

[67] W. D. Pesnell. *Solar dynamics observatory (SDO)*. Springer, 2015.

[68] R. P. Lin, B. R. Dennis, G. J. Hurford, D. M. Smith, A. Zehnder, P. R. Harvey, D. W. Curtis, D. Pankow, P. Turin, M. Bester, et al.

The reuven ramaty high-energy solar spectroscopic imager (RHESSI). *Solar Physics*, 210(1):3–32, 2002.

[69] A. I. Poland. Solar and heliospheric observatory (SOHO). In *Mass Supply and Flows in the Solar Corona: The 2nd SOHO Workshop*, volume 70, pages 7–12. Springer Science & Business Media, 2012.

[70] S. Krucker, M. Battaglia, P. J. Cargill, L. Fletcher, H. S. Hudson, A. L. MacKinnon, S. Masuda, L. Sui, M. Tomczak, A. L. Veronig, et al. Hard x-ray emission from the solar corona. *The Astronomy and Astrophysics Review*, 16(3-4):155–208, 2008.

[71] R. Turkmani, P.J. Cargill, K. Galsgaard, L. Vlahos, and H. Isliker. Particle acceleration in stochastic current sheets in stressed coronal active regions. *Astronomy & Astrophysics*, 449(2):749–757, 2006.

[72] P. J. Cargill, L. Vlahos, R. Turkmani, K. Galsgaard, and H. Isliker. Particle acceleration in a three-dimensional model of reconnecting coronal magnetic fields. *Space science reviews*, 124(1):249–259, 2006.

[73] M. Bárta, J. Büchner, M. Karlickỳ, and J.n Skála. Spontaneous current-layer fragmentation and cascading reconnection in solar flares. i. model and analysis. *The Astrophysical Journal*, 737(1):24, 2011.

[74] I. De Moortel, P. Browning, S. J. Bradshaw, B. Pintér, and E. Kontar. The way forward for coronal heating. *Astronomy & Geophysics*, 49(3):3–21, 2008.

[75] P. Cargill, C. Parnell, P. Browning, I. De Moortel, and A. Hood. Magnetic reconnection in the solar atmosphere: from proposal to paradigm. *Astronomy & Geophysics*, 51(3):3–31, 2010.

[76] V. K. Joshi and L. Prasad. Nanoflares heating of solar corona by reconnection model. *Romanian Astronomical Journal*, 22(1):13–21, 2012.

[77] H. S. Hudson. Solar physics: Solar flares add up. *Nature Physics*, 6:637–638, 2010.

[78] S. Wedemeyer-Böhm, E. Scullion, O. Steiner, L. R. van der Voort, J. de La Cruz Rodriguez, V. Fedun, and R. Erdélyi. Magnetic tornadoes as energy channels into the solar corona. *Nature*, 486(7404):505, 2012.

[79] P. Cargill and I. De Moortel. Solar physics: Waves galore. *Nature*, 475(7357):463–464, 2011.

[80] J. W. Cirtain, L. Golub, A. R. Winebarger, B. De Pontieu, K. Kobayashi, R. L. Moore, R. W. Walsh, K. E. Korreck, M. Weber, P. McCauley, et al. Energy release in the solar corona from spatially resolved magnetic braids. *Nature*, 493(7433):501, 2013.

[81] Nasa archive. `https://www.nymetroweather.com`.

[82] Space Studies Board, National Research Council, et al. *Plasma physics of the local cosmos*. National Academies Press, 2004.

[83] J. Egedal, W. Daughton, and A. Le. Large-scale electron acceleration by parallel electric fields during magnetic reconnection. *Nature Physics*, 8(4):321, 2012.

[84] F. S. Mozer, S. D. Bale, and T. D. Phan. Evidence of diffusion regions at a subsolar magnetopause crossing. *Physical review letters*, 89(1):015002, 2002.

[85] A. Retinò, D. Sundkvist, A. Vaivads, F. Mozer, M. André, and C. J. Owen. In situ evidence of magnetic reconnection in turbulent plasma. *Nature Physics*, 3(4):236, 2007.

[86] D. A. Uzdensky and R. M. Kulsrud. Physical origin of the quadrupole out-of-plane magnetic field in hall-magnetohydrodynamic reconnection. *Physics of Plasmas*, 13(6):062305, 2006.

[87] B. B. Kadomtsev. Disruptive instability in tokamaks. *Soviet Journal of Plasma Physics*, 1:710–715, 1975.

[88] N. F. Loureiro and D. A. Uzdensky. Magnetic reconnection: from the Sweet-Parker model to stochastic plasmoid chains. *Plasma Physics and Controlled Fusion*, 58(1):014021, 2015.

[89] M. T. Beidler and P. A. Cassak. Model for incomplete reconnection in sawtooth crashes. *Physical review letters*, 107(25):255002, 2011.

[90] Q. Yu, S. Günter, and K. Lackner. Numerical modelling of sawtooth crash using two-fluid equations. *Nuclear Fusion*, 55(11):113008, 2015.

[91] M. Zuin, N. Vianello, M. Spolaore, V. Antoni, T. Bolzonella, R. Cavazzana, E. Martines, G. Serianni, and D. Terranova. Current sheets during spontaneous reconnection in a current-carrying fusion plasma. *Plasma Phys. Control. Fusion*, 51(035012):15pp, 2009.

[92] Ma. Yamada, H. Ji, S. Hsu, T. Carter, R. Kulsrud, N. Bretz, F. Jobes, Y. Ono, and F. Perkins. Study of driven magnetic reconnection in a laboratory plasma. *Physics of Plasmas*, 4(5):1936–1944, 1997.

[93] J. Egedal, A. Fasoli, M. Porkolab, and D. Tarkowski. Plasma generation and confinement in a toroidal magnetic cusp. *Review of Scientific Instruments*, 71(9):3351–3361, 2000.

[94] P. A. Sweet. The neutral point theory of solar flares. In *Symposium-International Astronomical Union*, volume 6, pages 123–134. Cambridge University Press, 1958.

[95] E. N. Parker. Sweet's mechanism for merging magnetic fields in conducting fluids. *Journal of Geophysical Research*, 62(4):509–520, 1957.

[96] H. Ji and W. Daughton. Phase diagram for magnetic reconnection in heliophysical, astrophysical, and laboratory plasmas. *Physics of Plasmas*, 18(11):111207, 2011.

[97] P. A. Cassak and J. F. Drake. On phase diagrams of magnetic reconnection. *Physics of Plasmas*, 20(6):061207, 2013.

[98] H. E. Petschek. Magnetic field annihilation. *NASA Special Publication*, 50:425, 1964.

[99] N. F. Loureiro, A. A. Schekochihin, and S. C. Cowley. Instability of current sheets and formation of plasmoid chains. *Physics of Plasmas*, 14(10):100703, 2007.

[100] A. Bhattacharjee, Y.-M. Huang, H. Yang, and B. Rogers. Fast reconnection in high-Lundquist-number plasmas due to the plasmoid instability. *Physics of Plasmas*, 16(11):112102, 2009.

[101] D. H. Nickeler, M. Karlickỳ, T. Wiegelmann, and M. Kraus. Fragmentation of electric currents in the solar corona by plasma flows. *Astronomy & Astrophysics*, 556:A61, 2013.

[102] M. Karlickỳ and M. Bárta. Successive merging of plasmoids and fragmentation in a flare current sheet and their x-ray and radio signatures. *The Astrophysical Journal*, 733(2):107, 2011.

[103] L. J. Guo, A. Bhattacharjee, and Y. M. Huang. Distribution of plasmoids in post-coronal mass ejection current sheets. *The Astrophysical Journal Letters*, 771(1):L14, 2013.

[104] M. Karlickỳ, M. Bárta, and D. Nickeler. Fragmentation during merging of plasmoids in the magnetic field reconnection. *Astronomy & Astrophysics*, 541:A86, 2012.

[105] Q. Yu, S. Günter, and K. Lackner. Formation of plasmoids during sawtooth crashes. *Nuclear Fusion*, 54(7):072005, 2014.

[106] P. J. Cargill, L. Vlahos, G. Baumann, J. F. Drake, and Å. Nordlund. Current fragmentation and particle acceleration in solar flares. *Space science reviews*, 173(1-4):223–245, 2012.

[107] M. Onofri, H. Isliker, and L. Vlahos. Stochastic acceleration in turbulent electric fields generated by 3d reconnection. *Physical Review Letters*, 96(15):151102, 2006.

[108] RA Treumann and W Baumjohann. A note on the structure and kinematics of harris current sheets. *arXiv preprint arXiv:1307.7008*, 2013.

[109] P. Piovesan, M. Zuin, A. Alfier, D. Bonfiglio, F. Bonomo, A. Canton, S. Cappello, L. Carraro, R. Cavazzana, D. F. Escande, et al. Magnetic order and confinement improvement in high-current regimes of rfx-mod with mhd feedback control. *Nuclear Fusion*, 49(8):085036, 2009.

[110] H. Zohm. *Magnetohydrodynamic stability of tokamaks*. John Wiley & Sons, 2014.

[111] R. Fitzpatrick. *Plasma physics: an introduction*. Crc Press, 2014.

[112] M. Maraschek. *Neoclassical Tearing Mode (NTM)*, pages 259–304. Springer Berlin Heidelberg, Berlin, Heidelberg, 2015.

[113] R. Fitzpatrick. Formation and locking of the "slinky mode" in reversed-field pinches. *Physics of Plasmas*, 6(4):1168–1193, 1999.

[114] M. Zuin, L. Stevanato, E. Martines, F. Auriemma, B. Momo, R. Cavazzana, G. De Masi, W. Gonzalez, R. Lorenzini, P. Scarin, et al. Characterization of particle dynamics and magnetic reconnection in the RFX-mod plasmas. In *42nd EPS Conference on Plasma Physics*. European Physical Society, 2015.

[115] R. Fitzpatrick. Interaction of tearing modes with external structures in cylindrical geometry (plasma). *Nuclear Fusion*, 33(7):1049, 1993.

[116] R. Fitzpatrick, S. C. Guo, D. J. Den Hartog, and C. C. Hegna. Effect of a resistive vacuum vessel on dynamo mode rotation in reversed field pinches. *Physics of Plasmas*, 6(10):3878–3889, 1999.

[117] P. Martin, J. Adamek, P. Agostinetti, M. Agostini, A. Alfier, C. Angioni, V. Antoni, L. Apolloni, F. Auriemma, O. Barana, et al. Overview of the RFX fusion science program. *Nuclear Fusion*, 51(9):094023, 2011.

[118] M. F. M. De Bock, I. G. J. Classen, C. Busch, R. J. E. Jaspers, H. R. Koslowski, B. Unterberg, TEXTOR Team, et al. The interaction between plasma rotation, stochastic fields and tearing mode excitation by external perturbation fields. *Nuclear Fusion*, 48(1):015007, 2008.

[119] P. Innocente, P. Zanca, M. Zuin, T. Bolzonella, and B. Zaniol. Tearing modes transition from slow to fast rotation branch in the presence of magnetic feedback. *Nuclear Fusion*, 54(12):122001, 2014.

[120] C. G. Gimblett. On free boundary instabilities induced by a resistive wall. *Nuclear fusion*, 26(5):617, 1986.

[121] F. Gnesotto, P. Sonato, W. R. Baker, A. Doria, F. Elio, M. Fauri, P. Fiorentin, G. Marchiori, and G. Zollino. The plasma system of RFX. *Fusion engineering and design*, 25(4):335–372, 1995.

[122] F. L. Waelbroeck. Natural velocity of magnetic islands. *Physical review letters*, 95(3):035002, 2005.

[123] Q. Yu, S. Günter, Y. Kikuchi, and K. H. Finken. Numerical modelling of error field penetration. *Nuclear Fusion*, 48(2):024007, 2008.

[124] P. Zanca and D. Terranova. Reconstruction of the magnetic perturbation in a toroidal reversed field pinch. *Plasma physics and controlled fusion*, 46(7):1115, 2004.

[125] L. Carraro, M. E. Puiatti, F. Sattin, P. Scarin, and M. Valisa. Toroidal and poloidal plasma rotation in the reversed field pinch RFX. *Plasma physics and controlled fusion*, 40(6):1021, 1998.

[126] L Carraro, ME Puiatti, F Sattin, P Scarin, M Valisa, and M Mattioli. Carbon and oxygen behaviour in the reversed field pinch rfx. *Nuclear fusion*, 36(12):1623, 1996.

[127] P. Zanca. Avoidance of tearing modes wall-locking in a reversed field pinch with active feedback coils. *Plasma Physics and Controlled Fusion*, 51(1):015006, 2009.

[128] P. Innocente, S. Martini, A. Canton, and L. Tasinato. Upgrade of the RFX CO2 interferometer using in-vessel optics for extended edge resolution. *Review of scientific instruments*, 68(1):694–697, 1997.

[129] A. Fassina, M. Gobbin, S. Spagnolo, P. Franz, and D. Terranova. Characterization of small thermal structures in RFX-mod electron temperature profiles. *Plasma Physics and Controlled Fusion*, 58(5):055017, 2016.

[130] M. Zuin, W. Schneider, A. Barzon, R. Cavazzana, P. Franz, E. Martines, M.E. Puiatti, P. Scarin, and E. Zampiva. Ion temperature measurements by means of a neutral particle analyzer in RFX-mod plasmas. volume 35 2, pages 1844–1847, 2011.

[131] P. Zanca, L. Marrelli, R. Paccagnella, A. Soppelsa, M. Baruzzo, T. Bolzonella, G. Marchiori, P. Martin, and P. Piovesan. Feedback control model of the m= 2, n= 1 resistive wall mode in a circular plasma. *Plasma Physics and Controlled Fusion*, 54(9):094004, 2012.

[132] M. Okabayashi, P. Zanca, E. J. Strait, A. M. Garofalo, J. M. Hanson, Y. In, R. J. La Haye, L. Marrelli, P. Martin, R. Paccagnella, et al. Avoidance of tearing mode locking with electro-magnetic torque introduced by feedback-based mode rotation control in DIII-D and RFX-mod. *Nuclear Fusion*, 57(1):016035, 2016.

[133] G. Pucella, E. Giovannozzi, P. Buratti, and C. Cianfarani. MHD limit cycles on FTU. *Nucl. Fusion*, 57(116037):116037, 2017.

[134] D. Bonfiglio, D. F. Escande, P. Zanca, and S. Cappello. Necessary criterion for magnetic field reversal in the reversed-field pinch. *Nuclear Fusion*, 51(6):063016, 2011.